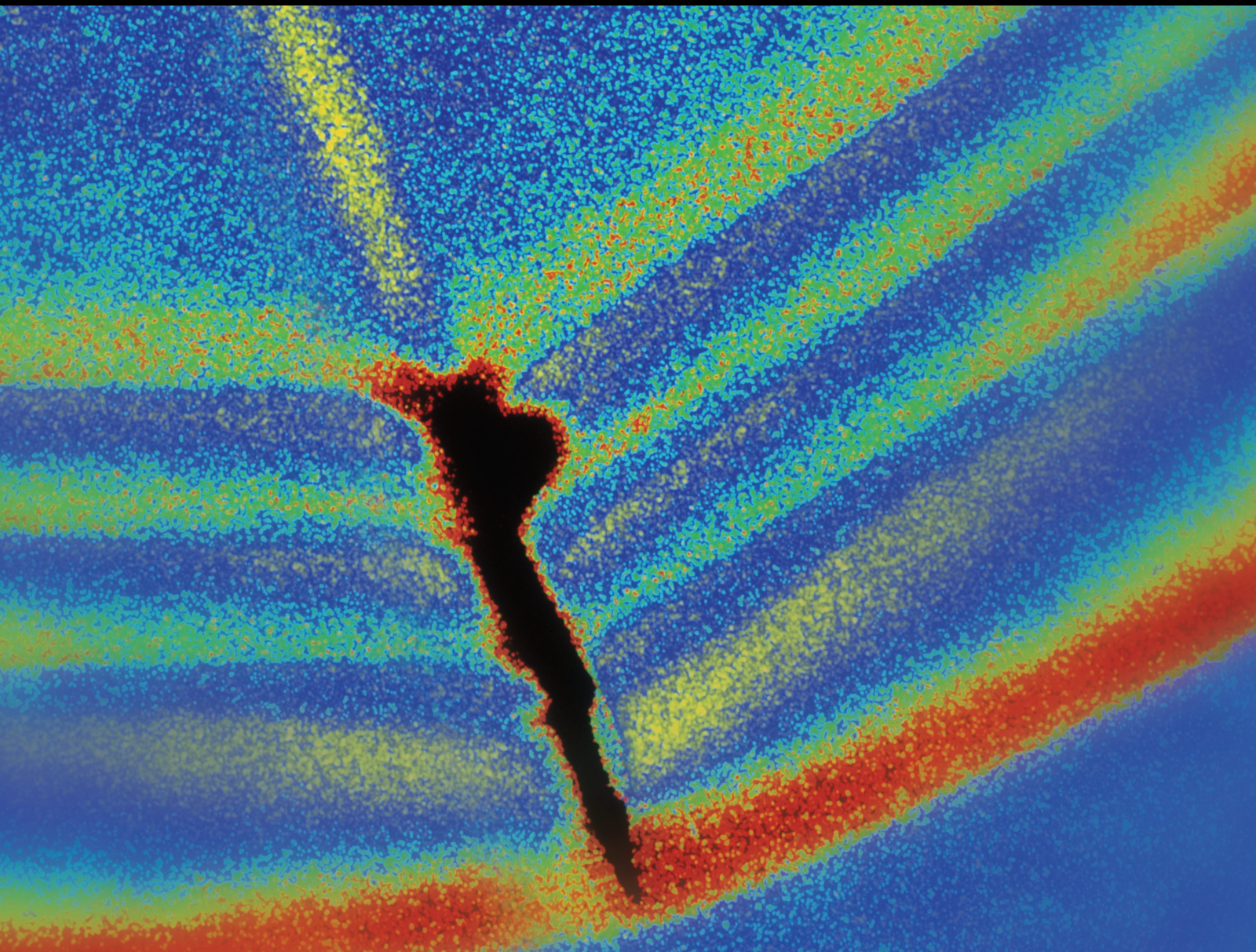


Vibration Control of Buildings Under Wind and Earthquake Loads Using Energy Dissipation Devices

Lead Guest Editor: Edén Bojórquez

Guest Editors: Sonia E. Ruiz, Alfredo Reyes-Salazar, and Antonio Formisano





Vibration Control of Buildings Under Wind and Earthquake Loads Using Energy Dissipation Devices

Vibration Control of Buildings Under Wind and Earthquake Loads Using Energy Dissipation Devices

Lead Guest Editor: Edén Bojórquez

Guest Editors: Sonia E. Ruiz, Alfredo Reyes-Salazar,
and Antonio Formisano

Chief Editor

Huu-Tai Thai , Australia

Associate Editors

Ivo Calì , Italy
Nawawi Chouw , New Zealand
Longjun Dong , China
Farzad Ebrahimi , Iran
Mickaël Lallart , France
Vadim V. Silberschmidt , United Kingdom
Mario Terzo , Italy
Angelo Marcelo Tusset , Brazil

Academic Editors

Omid A. Yamini , Iran
Maher Abdelghani, Tunisia
Haim Abramovich , Israel
Desmond Adair , Kazakhstan
Manuel Aenlle Lopez , Spain
Brij N. Agrawal, USA
Ehsan Ahmadi, United Kingdom
Felix Albu , Romania
Marco Alfano, Italy
Sara Amoroso, Italy
Huaming An, China
P. Antonaci , Italy
José V. Araújo dos Santos , Portugal
Lutz Auersch , Germany
Matteo Aureli , USA
Azwan I. Azmi , Malaysia
Antonio Batista , Brazil
Mattia Battarra, Italy
Marco Belloli, Italy
Francisco Beltran-Carbajal , Mexico
Denis Benasciutti, Italy
Marta Berardengo , Italy
Sébastien Besset, France
Giosuè Boscato , Italy
Fabio Botta , Italy
Giuseppe Brandonisio , Italy
Francesco Bucchi , Italy
Rafał Burdzik , Poland
Salvatore Caddemi , Italy
Wahyu Caesarendra , Brunei Darussalam
Baoping Cai, China
Sandro Carbonari , Italy
Cristina Castejón , Spain

Nicola Caterino , Italy
Gabriele Cazzulani , Italy
Athanasios Chasalevris , Greece
Guoda Chen , China
Xavier Chimentin , France
Simone Cinquemani , Italy
Marco Civera , Italy
Marco Cocconcelli , Italy
Alvaro Cunha , Portugal
Giorgio Dalpiaz , Italy
Thanh-Phong Dao , Vietnam
Arka Jyoti Das , India
Raj Das, Australia
Silvio L.T. De Souza , Brazil
Xiaowei Deng , Hong Kong
Dario Di Maio , The Netherlands
Raffaella Di Sante , Italy
Luigi Di Sarno, Italy
Enrique Lopez Droguett , Chile
Mădălina Dumitriu, Romania
Sami El-Borgi , Qatar
Mohammad Elahinia , USA
Said Elias , Iceland
Selçuk Erkaya , Turkey
Gaoliang Fang , Canada
Fiorenzo A. Fazzolari , United Kingdom
Luis A. Felipe-Sese , Spain
Matteo Filippi , Italy
Piotr Fołęga , Poland
Paola Forte , Italy
Francesco Franco , Italy
Juan C. G. Prada , Spain
Roman Gabl , United Kingdom
Pedro Galvín , Spain
Jinqiang Gan , China
Cong Gao , China
Arturo García García-Perez, Mexico
Rozaimi Ghazali , Malaysia
Marco Gherlone , Italy
Anindya Ghoshal , USA
Gilbert R. Gillich , Romania
Antonio Giuffrida , Italy
Annalisa Greco , Italy
Jiajie Guo, China

Amal Hajjaj , United Kingdom
Mohammad A. Hariri-Ardebili , USA
Seyed M. Hashemi , Canada
Xue-qiu He, China
Agustin Herrera-May , Mexico
M.I. Herreros , Spain
Duc-Duy Ho , Vietnam
Hamid Hosano , Japan
Jin Huang , China
Ahmed Ibrahim , USA
Bernard W. Ikua, Kenya
Xingxing Jiang , China
Jiang Jin , China
Xiaohang Jin, China
MOUSTAFA KASSEM , Malaysia
Shao-Bo Kang , China
Yuri S. Karinski , Israel
Andrzej Katunin , Poland
Manoj Khandelwal, Australia
Denise-Penelope Kontoni , Greece
Mohammadreza Koopialipoor, Iran
Georges Kouroussis , Belgium
Genadijus Kulvietis, Lithuania
Pradeep Kundu , USA
Luca Landi , Italy
Moon G. Lee , Republic of Korea
Trupti Ranjan Lenka , India
Arcanjo Lenzi, Brazil
Marco Lepidi , Italy
Jinhua Li , China
Shuang Li , China
Zhixiong Li , China
Xihui Liang , Canada
Tzu-Kang Lin , Taiwan
Jinxin Liu , China
Ruonan Liu, China
Xiuquan Liu, China
Siliang Lu, China
Yixiang Lu , China
R. Luo , China
Tianshou Ma , China
Nuno M. Maia , Portugal
Abdollah Malekjafarian , Ireland
Stefano Manzoni , Italy





Stefano Marchesiello , Italy
Francesco S. Marulo, Italy
Traian Mazilu , Romania
Vittorio Memmolo , Italy
Jean-Mathieu Mencik , France
Laurent Mevel , France
Letícia Fleck Fadel Miguel , Brazil
FuRen Ming , China
Fabio Minghini , Italy
Marco Miniaci , USA
Mahdi Mohammadpour , United Kingdom
Rui Moreira , Portugal
Emiliano Mucchi , Italy
Peter Múčka , Slovakia
Fehmi Najar, Tunisia
M. Z. Naser, USA
Amr A. Nassr, Egypt
Sundararajan Natarajan , India
Toshiaki Natsuki, Japan
Miguel Neves , Portugal
Sy Dzung Nguyen , Republic of Korea
Trung Nguyen-Thoi , Vietnam
Gianni Niccolini, Italy
Rodrigo Nicoletti , Brazil
Bin Niu , China
Leilei Niu, China
Yan Niu , China
Lucio Olivares, Italy
Erkan Oterkus, United Kingdom
Roberto Palma , Spain
Junhong Park , Republic of Korea
Francesco Pellicano , Italy
Paolo Pennacchi , Italy
Giuseppe Petrone , Italy
Evgeny Petrov, United Kingdom
Franck Poisson , France
Luca Pugi , Italy
Yi Qin , China
Virginio Quaglini , Italy
Mohammad Rafiee , Canada
Carlo Rainieri , Italy
Vasudevan Rajamohan , India
Ricardo A. Ramirez-Mendoza , Mexico
José J. Rangel-Magdaleno , Mexico

Didier Rémond , France
Dario Richiedei , Italy
Fabio Rizzo, Italy
Carlo Rosso , Italy
Riccardo Rubini , Italy
Salvatore Russo , Italy
Giuseppe Ruta , Italy
Edoardo Sabbioni , Italy
Pouyan Roodgar Saffari , Iran
Filippo Santucci de Magistris , Italy
Fabrizio Scozzese , Italy
Abdullah Seçgin, Turkey
Roger Serra , France
S. Mahdi Seyed-Kolbadi, Iran
Yujie Shen, China
Bao-Jun Shi , China
Chengzhi Shi , USA
Gerardo Silva-Navarro , Mexico
Marcos Silveira , Brazil
Kumar V. Singh , USA
Jean-Jacques Sinou , France
Isabelle Sochet , France
Alba Sofi , Italy
Jussi Sopanen , Finland
Stefano Sorace , Italy
Andrea Spaggiari , Italy
Lei Su , China
Shuaishuai Sun , Australia
Fidelis Tawiah Suorineni , Kazakhstan
Cecilia Surace , Italy
Tomasz Szolc, Poland
Iacopo Tamellini , Italy
Zhuhua Tan, China
Gang Tang , China
Chao Tao, China
Tianyou Tao, China
Marco Tarabini , Italy
Hamid Toopchi-Nezhad , Iran
Carlo Trigona, Italy
Federica Tubino , Italy
Nerio Tullini , Italy
Nicolò Vaiana , Italy
Marcello Vanali , Italy
Christian Vanhille , Spain

Dr. Govind Vashishtha, Poland
F. Viadero, Spain
M. Ahmer Wadee , United Kingdom
C. M. Wang , Australia
Gaoxin Wang , China
Huiqi Wang , China
Pengfei Wang , China
Weiqiang Wang, Australia
Xian-Bo Wang, China
YuRen Wang , China
Wai-on Wong , Hong Kong
Yuanping XU , China
Biao Xiang, China
Qilong Xue , China
Xin Xue , China
Diansen Yang , China
Jie Yang , Australia
Chang-Ping Yi , Sweden
Nicolo Zampieri , Italy
Chao-Ping Zang , China
Enrico Zappino , Italy
Guo-Qing Zhang , China
Shaojian Zhang , China
Yongfang Zhang , China
Yaobing Zhao , China
Zhipeng Zhao, Japan
Changjie Zheng , China
Chuanbo Zhou , China
Hongwei Zhou, China
Hongyuan Zhou , China
Jiaxi Zhou , China
Yunlai Zhou, China
Radoslaw Zimroz , Poland

Contents


Enhanced Seismic Structural Reliability on Reinforced Concrete Buildings by Using Buckling Restrained Braces

Victor Baca, Juan Bojórquez , Edén Bojórquez , Herian Leyva, Alfredo Reyes-Salazar, Sonia E. Ruiz , Antonio Formisano, Leonardo Palemón, Robespierre Chávez, and Manuel Barraza 
Research Article (12 pages), Article ID 8816552, Volume 2021 (2021)

A Structural Configuration with Separate Substructures towards Reducing the Seismic Damage of Spatial Structures with Rectangular Plan

Dabin Yang , Litai Sun, Hao Wang , Lei Liu, Mingjin Li, and Xiangyi Sun
Research Article (13 pages), Article ID 8880747, Volume 2020 (2020)

Optimal Location of Multiple Tuned Mass Dampers in Regular and Irregular Tall Steel Buildings Plan





Mohsen Khazaei , Reza Vahdani, and Ali Kheyroddin
Research Article (20 pages), Article ID 9072637, Volume 2020 (2020)

Enhancing the Seismic Performance of Precast RC Frames with Cladding Panels through Setting U-Shaped Dampers and Rocking Walls

Qing Jiang , Hanqin Wang, Yulong Feng , Xun Chong, Junqi Huang, and Yibo Liu
Research Article (16 pages), Article ID 4182094, Volume 2020 (2020)

Research Article

Enhanced Seismic Structural Reliability on Reinforced Concrete Buildings by Using Buckling Restrained Braces

Victor Baca,¹ Juan Bojórquez ,¹ Edén Bojórquez ,¹ Herian Leyva,¹ Alfredo Reyes-Salazar,¹ Sonia E. Ruiz ,² Antonio Formisano,³ Leonardo Palemón,⁴ Robespierre Chávez,¹ and Manuel Barraza ⁵

¹Facultad de Ingeniería, Universidad Autónoma de Sinaloa, Culiacán 80040, Mexico

²Instituto de Ingeniería, Universidad Nacional Autónoma de México, México 04510, Mexico

³Department of Structures for Engineering and Architecture, University of Naples, Naples 80125, Italy

⁴Departamento de Ingeniería Civil, Universidad Autónoma del Carmen, Cd. del Carmen 24180, Mexico

⁵Facultad de Ingeniería, Arquitectura y Diseño, Universidad Autónoma de Baja California, Ensenada 22860, Mexico

Correspondence should be addressed to Juan Bojórquez; jbm_squall_cloud@hotmail.com

Received 5 August 2020; Revised 24 December 2020; Accepted 28 January 2021; Published 9 February 2021

Academic Editor: Francisco Beltran-Carbajal

Copyright © 2021 Victor Baca et al. This is an open access article distributed under the Creative Commons Attribution License, which permits unrestricted use, distribution, and reproduction in any medium, provided the original work is properly cited.

The control of vibrations and damage in traditional reinforced concrete (RC) buildings under earthquakes is a difficult task. It requires the use of innovative devices to enhance the seismic behavior of concrete buildings. In this paper, we design RC buildings with buckling restrained braces (BRBs) to achieve this objective. For this aim, three traditional RC framed structures with 3, 6, and 9 story levels are designed by using the well-known technique nondominated sorting genetic algorithm (NSGA-II) in order to reduce the cost and maximize the seismic performance. Then, equivalent RC buildings are designed but including buckling restrained braces. Both structural systems are subjected to several narrow-band ground motions recorded at soft soil sites of Mexico City scaled at different levels of intensities in terms of the spectral acceleration at first mode of vibration of the structure $S_a(T_1)$. Then, incremental dynamic analysis, seismic fragility, and structural reliability in terms of the maximum interstory drift are computed for all the buildings. For the three selected structures and the equivalent models with BRBs, it is concluded that the annual rate of exceedance is considerably reduced when BRBs are incorporated. For this reason, the structural reliability of the RC buildings with BRBs has a better behavior in comparison with the traditional reinforced concrete buildings. The use of BRBs is a good option to improve strength and seismic behavior and hence the structural reliability of RC buildings subjected to strong earthquake ground motions.

1. Introduction

In the past few years, an extensive amount of buildings has suffered damage due to medium and large earthquakes. Structural systems have evolved in order to reduce seismic damage. Nowadays, one of the most used structural systems is that based on reinforced concrete frames. Reinforced concrete buildings have been frequently used; nevertheless, the main disadvantage of them is the difficulty to be repaired after the occurrence of an earthquake. Furthermore, RC structures located on seismic zones usually are subjected to large peak interstory drift displacements produced by the lateral loads.

Since the seismic design regulations recommend the control of maximum interstory drift as the main engineering demand parameter in order to achieve a good structural performance as Krawinkler and Gupta suggest [1], it is necessary to reduce the peak drift demands in RC buildings. The displacement on traditional concrete buildings can be reduced by means of concentrically braces. The objective of the braces in structural frames is to increase the stiffness and to reduce the lateral displacements due to earthquakes [2, 3]. In spite of the advantages of typical braced frames, several studies have highlighted that frequent damage has been observed on this type of structural system in past earthquakes such as the 1985 Mexico

earthquake, 1989 Loma Prieta earthquake, 1994 Northridge earthquake, and 1995 Hyogo-ken Nanbu earthquake, among others [4–9], as it was indicated by Sabelli et al. [10]. In particular, the unsymmetrical properties in tension and compression and the large strength deterioration in compression reduce considerably the performance of the braces. In order to have the same mechanical properties in tension and compression of the braces, a new type of brace named buckling restrained brace which consists of a ductility steel core that is forced to have similar yield in tension and compression by restrained the buckling has been suggested [11–17]. Several experimental tests have demonstrated that the cyclic behavior of the BRBs is stable and almost bilinear; in particular, Palazzo et al. [18] concluded that it is feasible to design buckling restrained braces that are efficient, robust, virtually maintenance-free, durable, reasonably cheap, easy to produce, and made of basic and easily replaceable materials. For this reason, although the seismic response of reinforced concrete frames with buckling restrained braces has been studied, usually 2D systems are considered for the dynamic analyses; moreover, the advantages of BRBs on RC buildings in terms of structural fragility and reliability are not commonly assessed. Motivated by the need to observe the advantages of BRBs in the seismic performance in terms of structural fragility and reliability of 3D reinforced concrete framed buildings, in the present study, the seismic performance of 3D RC buildings and equivalent 3D RC structures with BRBs is assessed. For the purpose of this work, three structural RC buildings with 3, 6, and 9 stories are designed according to the Mexico City Seismic Design Provisions (MCS DP) [19]. In addition, three equivalent concrete buildings with BRBs are designed. It is important to say that for the seismic design of all the buildings, the NSGA-II approach [20, 21] is used in order to reduce the cost and increase the structural capacity in accordance with the MCS DP. The 3D framed buildings in both type of structural systems are subjected to 30 ground motion records obtained from soft soil sites of Mexico City scaled at different spectral accelerations at first mode of vibration of the structure. Thus, a total of 3,600 seismic analyses have been performed. The numerical results of the analyses suggest that the seismic performance of reinforced concrete buildings with buckling restrained braces is superior to that of the structural behavior of traditional buildings indicating the advantages of this structural system. For this reason, BRBs can increase considerably the structural reliability when they are incorporated in reinforced concrete frames. Moreover, the damage in the buildings with BRBs is concentrated in the braces which can be replaced after the occurrence of an earthquake. It is important to say that although soil structure interaction was not taken into account, notice that similar conclusions are expected because this effect increases the period of vibration of a building [22, 23].

2. Buckling Restrained Braces

The innovative buckling restrained braces are devices used as seismic energy absorption elements with the aim of reducing the damage in a structure under strong earthquake events. They consist of a steel section enclosed in a tubular or cylindrical case filled with concrete or mortar. Figure 1 shows

the topology and components of this brace [11, 24], which makes it possible to take advantage of the full capacity of steel core and to obtain a symmetrical and highly stable cyclic behavior in comparison with conventional braces. In addition, BRBs can be easily replaced in case of damage.

Different experimental studies on this type of devices have been carried out. Terán-Gilmore and Virto-Cambray [25] performed cyclic test at multiple BRBs using circular tube or angle steel cores concluding that both developed stable hysteretic behavior and similar resistance to both compression and tension. Khampanit et al. [2] proposed an energy-based design methodology by comparing experimental studies between a reinforced concrete bare frame and a reinforced concrete braced frame. Guerrero et al. [26] carried out a comparative study between two 5-story steel frames with and without BRB at 1/10 scale factor under narrow-band seismic records obtained in Mexico City. The results demonstrated a considerable decrease in terms of displacements, maximum interstory drift, and floor accelerations for braced frames, as well as an increase of stiffness and damping of the system. Similarly, studies have been carried out on new methods to adequately model this type of braces. Rahnavard et al. [27] compared hysteresis curves of experimental studies with a simple numerical model in order to avoid large computational time for the analyses. In addition, they have used this type of brace for retrofit or strengthening of concrete buildings [28]. In this study, a considerable difference is observed in lateral resistance, cyclic behavior, and energy dissipation capacity. The lateral stiffness that a BRB brings to a floor can be obtained regardless of the core area as shown in the following equation [29]:

$$\frac{K_L}{(A/L)} = \frac{E \cos^2 \theta}{\gamma + \eta(1 - \gamma)} = \frac{E \cos^2 \theta}{L_{RF}}, \quad (1)$$

where L is the total length of the brace, E is the elastic modulus, θ is the angle of inclination, L_c is the length of element without connections, γ is the relation between L_c and L , η is the relation between average axial strains of outside and inside the core, and L_{RF} is a factor that considers the region of higher axial stiffness at the ends of the brace. Terán-Gilmore and Ruiz-García [30] determined that under the consideration of L_c , it is equal to half value of L , and that the average area outside the core is three times the area of core; L_{RF} is equal to 0.667. Therefore, the actual stiffness that BRB brings to the system depends on the difference between the core and connection areas. Through this type of mechanism, the reinforced concrete braced and unbraced buildings were designed using the NSGA-II approach as explained below. Finally, the seismic reliability when both structural systems are subjected to narrow-band motions recorded in Mexico City is compared.

3. Methodology

3.1. Seismic Design of the RC Models Using NSGA-II. Currently, there are a large number of studies on the application of optimization techniques for structural design,

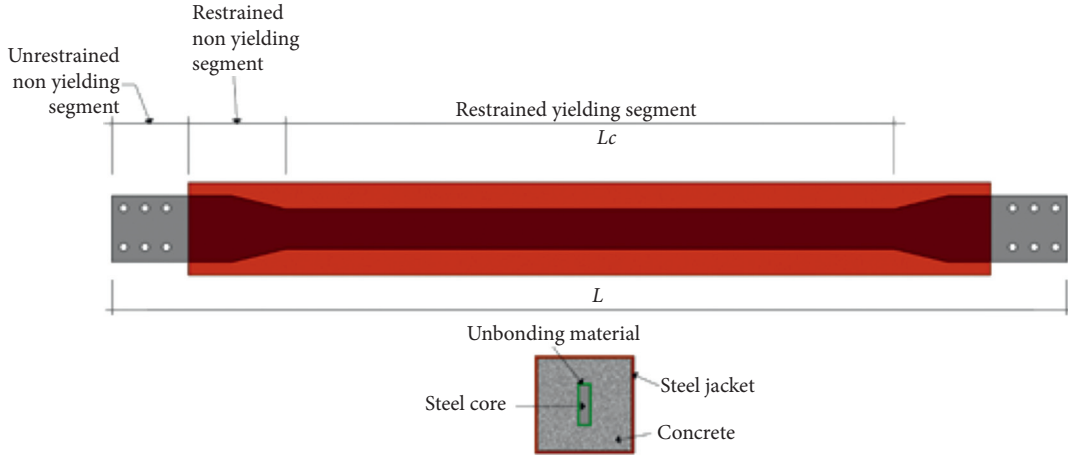


FIGURE 1: Buckling restrained brace parts and cross section components.

especially using genetic algorithms [31]. The aim of this approach is to generate a random population of solutions, classifying them according to their goodness as a solution to the problem using a fitness function. The closest solutions that satisfy the problem are used to obtain new solutions through a crossover procedure, maintaining the best characteristics of each solution. This procedure is repeated up to the desired cycles or generation number, and finally it is able to find optimal results. A typical genetic algorithm is based on the following parameters:

- (1) Fitness function: it consists of creating one or more functions that adequately evaluate the ability of each solution to solve the problem. In addition, penalties are included in order to eliminate those solutions that do not comply simple requirements, in this case some penalties can be adequate beam-columns connections, excessive or inadequate height of section, and excessive displacement, among others. It is important to classify individuals using these values.
- (2) Crossover: it is based on getting new solutions from the best ones. To this aim, each one is represented by a binary codification and the combination of two different codes at any point generates new ones. This exchange is similar to that obtained in sexual reproduction.
- (3) Mutation: it consists of generating diversity by the change of a single bit from binary code using a desired probability that determines which solutions mutate.

For seismic design purposes, it is necessary to use a multiobjective optimization technique such as NSGA-II [21]. This method has been useful for the seismic design of 2D and 3D framed steel buildings compared with another optimization technique [32], for multiobjective design of green buildings [33]. Furthermore, it has recently been used for the optimal design of structures equipped with semi-active fluid viscous dampers [34].

In this study, three RC buildings with 3, 6, and 9 stories named RC3, RC6, and RC9 and equivalent structural models

with BRBs (named RC3-BRB, RC6-BRB, and RC9-BRB) were designed evaluating two fitness functions: the cost and the maximum interstory drift. While the main characteristics of the structural models are shown in Table 1, Figure 2 illustrates a 3D view of the braced building with 6 story levels. Notice that all the buildings were designed under seismic loads corresponding to soft soil sites of Mexico City. It was proposed to use a different section of beam and column for each 3 floors and one BRB section for all the framed buildings.

The full procedure used for the seismic design of the three framed RC buildings is illustrated in Figure 3 (see Leyva et al. [35] for more details about this approach). The same procedure was used for the seismic design of the RC buildings with BRBs.

As it was indicated before, Figure 3 shows a flowchart of the design procedure. In first place, a number of generation and population are proposed; notice that the first generation is randomly created. Then, we proceed to carry out the main parameters of the genetic algorithm, especially, the fitness functions (2) and (3), crossover, and mutation, in order to obtain the individuals of the new generation. This procedure is repeated and better results are expected as the number of generations increases. It is important to mention that the fitness functions were calibrated based on numerous tests of the algorithm.

$$F_1 = I_{MID} C_{slab}^5 C_d^3 C_{con} C_s^{1/10}, \quad (2)$$

$$F_2 = C^{1/3} C_{slab}^5 C_d^3 C_{con} C_s^{1/10}, \quad (3)$$

where F_1 and F_2 are the fitness functions of maximum interstory drift (MID) and cost, respectively. F_1 has the objective to find the lightest sections comparing MID with a target drift (TD), as shown in the following equation:

$$I_{MID} = \frac{TD}{MID}. \quad (4)$$

With F_2 , it is intended to obtain the most economical sections taking into account the materials and labor cost of the building:

TABLE 1: Main geometric characteristics of the designed structural models.

Model	Number of floors	Bay dir. X	Bay dir. Y	Interstory height (m)	Bay length (m)	Total height (m)
RC3, RC3-BRB	3	3	3	3.5	7	10.5
RC6, RC6-BRB	6	3	3	3.5	7	21
RC9, RC9-BRB	9	3	3	3	5	27

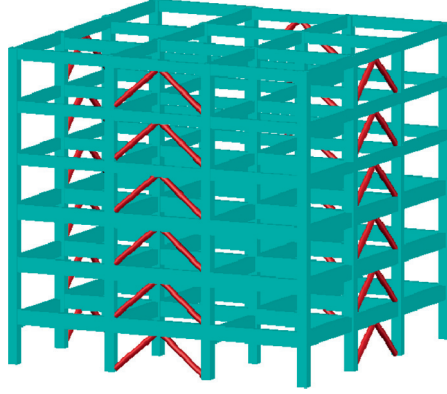


FIGURE 2: 3D view of the reinforced concrete building with BRBs (model RC-BRB6).

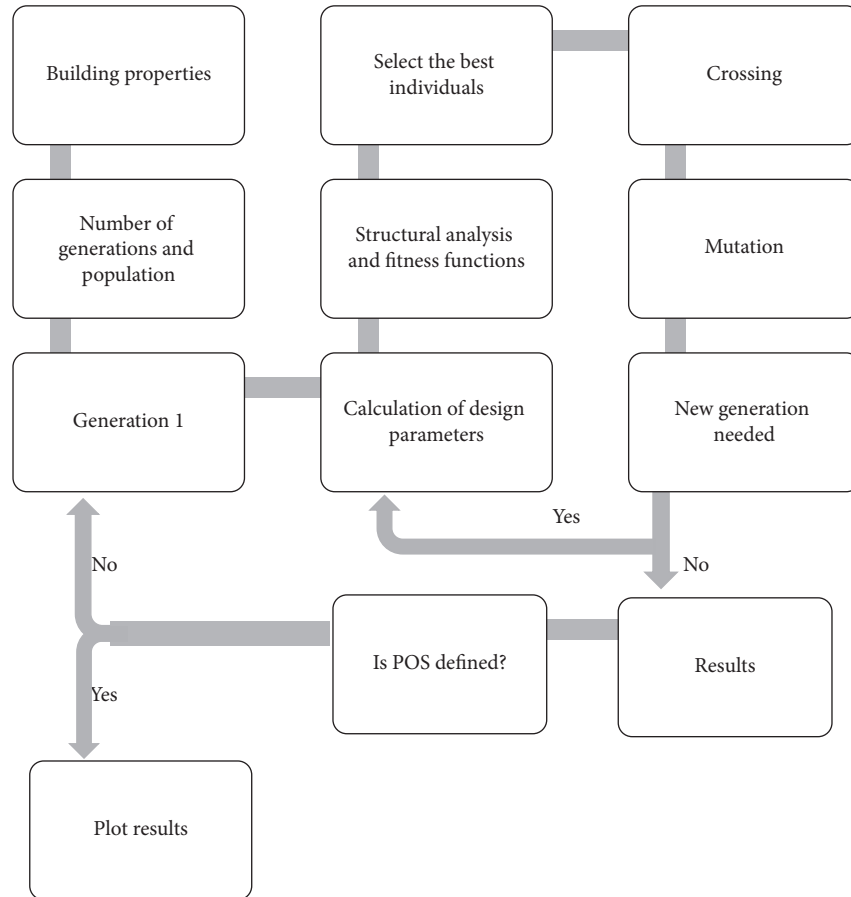


FIGURE 3: Flowchart used for the seismic design of the three-dimensional RC buildings [35].

$$C = C_r + C_c + C_l, \quad (5)$$

where C_r , C_c , C_b , and C are reinforcement, concrete, labor, and total costs, respectively.

The other parameters are used as design constraints if the individual does not satisfy the requirements of displacement (C_d), strength (C_s), constructive feasibility of connections (C_{con}), and slab thickness (C_{slab}).

This procedure was computed several times for each model studied to define the well-known Pareto frontier [21]. Table 2 shows the final sections and the main properties of the structural models obtained.

3.2. Earthquake Ground Motions. For the dynamic analyses of the structural models, thirty narrow-band earthquake ground motions recorded at soft soil sites of Mexico City are used. The soft soil ground motion records were selected because they demand high energy on structures in comparison to firm soil accelerograms [36, 37]. The ground motions were recorded in sites where the soil period is about two seconds and severe level of damage in structures was observed during the 1985 Mexico City Earthquake. In Table 3, some important characteristics of the records are illustrated. Notice that PGA and PGV denote the peak ground acceleration and velocity, and t_D indicates the Trifunac and Brady duration [38].

3.3. Structural Reliability Assessment. The incremental dynamic analysis [39] is used to assess the seismic performance of the RC buildings under narrow-band motions scaled at different intensity levels in terms of spectral acceleration at first mode of vibration of the structure. Next, the well-known seismic performance-based assessment procedure suggested by the Pacific Earthquake Engineering Center [40] in the United States was employed in this study, which indicates that the mean annual rate of exceeding (MARE) a certain engineering demand parameter (EDP), such as peak interstory drift, in this way exceeding a certain level edp can be computed as follows:

$$\lambda(EDP > edp) \cong \int_{IM} P[EDP > edp | IM = im] \cdot |d\lambda_{IM}(im)|, \quad (6)$$

where IM denotes the ground motion intensity measure (in this study, the spectral acceleration at the first-mode period of vibration was used as IM) and $P[EDP > edp | IM = im]$ represents the fragility curve which is the conditional probability that a EDP exceeds a certain level of edp given that the IM is evaluated at the ground motion intensity measure level im . Furthermore, $d\lambda_{IM}(im)$ refers to the differential of the seismic hazard curve of the site of interest. In this context, the conditional probability that EDP exceeds a certain level of edp can be obtained using incremental

dynamic analyses and estimating probabilistic of the EDP of interest. The second term in equation (6) is represented by the seismic hazard curve, which can be computed from conventional probabilistic seismic hazard analysis, evaluated at the ground motion intensity level im . It is important to note that the ground motion intensity measure plays an important role for assessment of the seismic performance, which is the joint between seismology and earthquake engineering. As stated, $S_a(T_1)$ was selected as IM and maximum interstory drift (MID) as EDP in such a way that equation (6) can be expressed as follows:

$$\lambda(MID > mid) \cong \int_{S_a(T_1)} P[MID > mid | S_a(T_1) = s_a] \cdot |d\lambda_{S_a(T_1)}(s_a)|, \quad (7)$$

where $d\lambda_{S_a(T_1)}(s_a) = \lambda_{S_a(T_1)}(s_a) - \lambda_{S_a(T_1)}(s_a + ds_a)$ is the hazard curve differential expressed in terms of $S_a(T_1)$. The seismic reliability of the selected RC and RC-BRB structures was evaluated using equation (7) in terms of the maximum interstory drift demands. In the evaluation of the first term in the integrand for the case of maximum interstory drift demands, a lognormal cumulative probability distribution was used [41]. For this reason, the term $P[MID > mid | S_a(T_1) = s_a]$ is analytically evaluated as follows:

$$P(MID > mid | S_a(T_1) = s_a) = 1 - \Phi\left(\frac{\ln mid - \hat{\mu}_{\ln MID|S_a(T_1)=s_a}}{\hat{\sigma}_{\ln MID|S_a(T_1)=s_a}}\right), \quad (8)$$

where $\hat{\mu}_{\ln MID|S_a(T_1)=s_a}$ and $\hat{\sigma}_{\ln MID|S_a(T_1)=s_a}$ are the geometric mean and standard deviation of the natural logarithm of the MID , respectively, and $\Phi(\cdot)$ is the standard normal cumulative distribution function. It is important to say that Bojórquez et al. [42] suggested the use of $S_a(T_1)$ as intensity measure for records having similar values of N_p [43].

4. Comparison of the Seismic Performance of the RC and RC-BRB Structures: Numerical Results

4.1. Incremental Dynamic Analysis. With the aim to assess and compare the structural fragility and reliability of both selected building models types, the first step is the development of incremental dynamic analysis (IDA) curves. For this aim, the peak interstory drift is computing at different values of the intensity measure $S_a(T_1)$ for all the narrow-band records under consideration. Note that the Ruaumoko software has been used for the 3600 dynamic analyses. Figure 4 compares the incremental dynamic analysis curves for the structural models RC and RC-BRB. It is observed that

TABLE 2: Main properties of the six RC building models (dimensions in cm).

Model property	RC3	RC3-BRB	RC6	RC6-BRB	RC9	RC9-BRB
Column1	55 × 55	40 × 40	65 × 65	55 × 55	55 × 55	60 × 60
Column2			65 × 65	50 × 50	55 × 55	45 × 45
Column3					45 × 45	35 × 35
Beam1	35 × 65	30 × 65	45 × 100	35 × 75	40 × 75	30 × 55
Beam2			35 × 75	35 × 65	40 × 70	30 × 60
Beam3					30 × 60	25 × 50
BRB (area)		40		52		36
Period (s)	0.69	0.42	0.87	0.72	0.92	0.87

TABLE 3: Selected ground motion records.

Record	Date	Magnitude	Station	PGA (cm/s ²)	PGV (cm/s)	t_D (s)
1	19/09/1985	8.1	SCT	178.0	59.5	34.8
2	21/09/1985	7.6	Tlahuac deportivo	48.7	14.6	39.9
3	25/04/1989	6.9	Alameda	45.0	15.6	37.8
4	25/04/1989	6.9	Garibaldi	68.0	21.5	65.5
5	25/04/1989	6.9	SCT	44.9	12.8	65.8
6	25/04/1989	6.9	Sector popular	45.1	15.3	79.4
7	25/04/1989	6.9	Tlatelolco TL08	52.9	17.3	56.6
8	25/04/1989	6.9	Tlatelolco TL55	49.5	17.3	50.0
9	14/09/1995	7.3	Alameda	39.3	12.2	53.7
10	14/09/1995	7.3	Garibaldi	39.1	10.6	86.8
11	14/09/1995	7.3	Liconsa	30.1	9.62	60.0
12	14/09/1995	7.3	Plutarco Elías Calles	33.5	9.37	77.8
13	14/09/1995	7.3	Sector popular	34.3	12.5	101.2
14	14/09/1995	7.3	Tlatelolco TL08	27.5	7.8	85.9
15	14/09/1995	7.3	Tlatelolco TL55	27.2	7.4	68.3
16	09/10/1995	7.5	Cibeles	14.4	4.6	85.5
17	09/10/1995	7.5	CU Juárez	15.8	5.1	97.6
18	09/10/1995	7.5	Centro urbano Presidente Juárez	15.7	4.8	82.6
19	09/10/1995	7.5	Córdoba	24.9	8.6	105.1
20	09/10/1995	7.5	Liverpool	17.6	6.3	104.5
21	09/10/1995	7.5	Plutarco Elías Calles	19.2	7.9	137.5
22	09/10/1995	7.5	Sector popular	13.7	5.3	98.4
23	09/10/1995	7.5	Valle Gómez	17.9	7.18	62.3
24	11/01/1997	6.9	CU Juárez	16.2	5.9	61.1
25	11/01/1997	6.9	Centro urbano Presidente Juárez	16.3	5.5	85.7
26	11/01/1997	6.9	García Campillo	18.7	6.9	57.0
27	11/01/1997	6.9	Plutarco Elías Calles	22.2	8.6	76.7
28	11/01/1997	6.9	Est. # 10 Roma A	21.0	7.76	74.1
29	11/01/1997	6.9	Est. # 11 Roma B	20.4	7.1	81.6
30	11/01/1997	6.9	Tlatelolco TL08	16.0	7.2	57.5

the maximum interstory drift in general tends to increase for all the building models as $S_a(T_1)$ also increases. In particular, the maximum interstory drift for a specific value of $S_a(T_1)$ is smaller in the case of the BRB buildings. For example, for the structural frame with 6 story levels and a value of $S_a(T_1)$ equal to 900 cm/s², the peak drift for the traditional RC6 model could be larger than 0.2, while in the case of RC6-BRB, it is smaller than 0.1. In other words, the uncertainty in the structural response prediction also tends to increase for larger values of $S_a(T_1)$, and this is especially true for the unbraced RC buildings. Figure 5 compares the standard deviation of the seismic response for the buildings with 3 stories at different performance levels in terms of the median maximum interstory drift. As it was expected, the values of the standard deviation are larger for the RC3 model in

comparison with the RC3-BRB building. Finally, Figure 6 shows the seismic performance in terms of damage configuration of the BRBs for the model RC-BRB6 under record number one. It is observed that the structural damage is concentrated in the BRBs of the lower stories, as it is illustrated in the hysteretic curves of the braced for two intensity levels in terms of $S_a(T_1)$. It is important to say that for the selected scaling levels of the ground motion records, the BRBs have not reached their maximum capacity.

4.2. Structural Fragility. The structural fragility curves for the RC and RC-BRB buildings are computed in this section via equation (8) in terms of maximum interstory drift. The Mexico City Building Code and Bojórquez et al. [42]

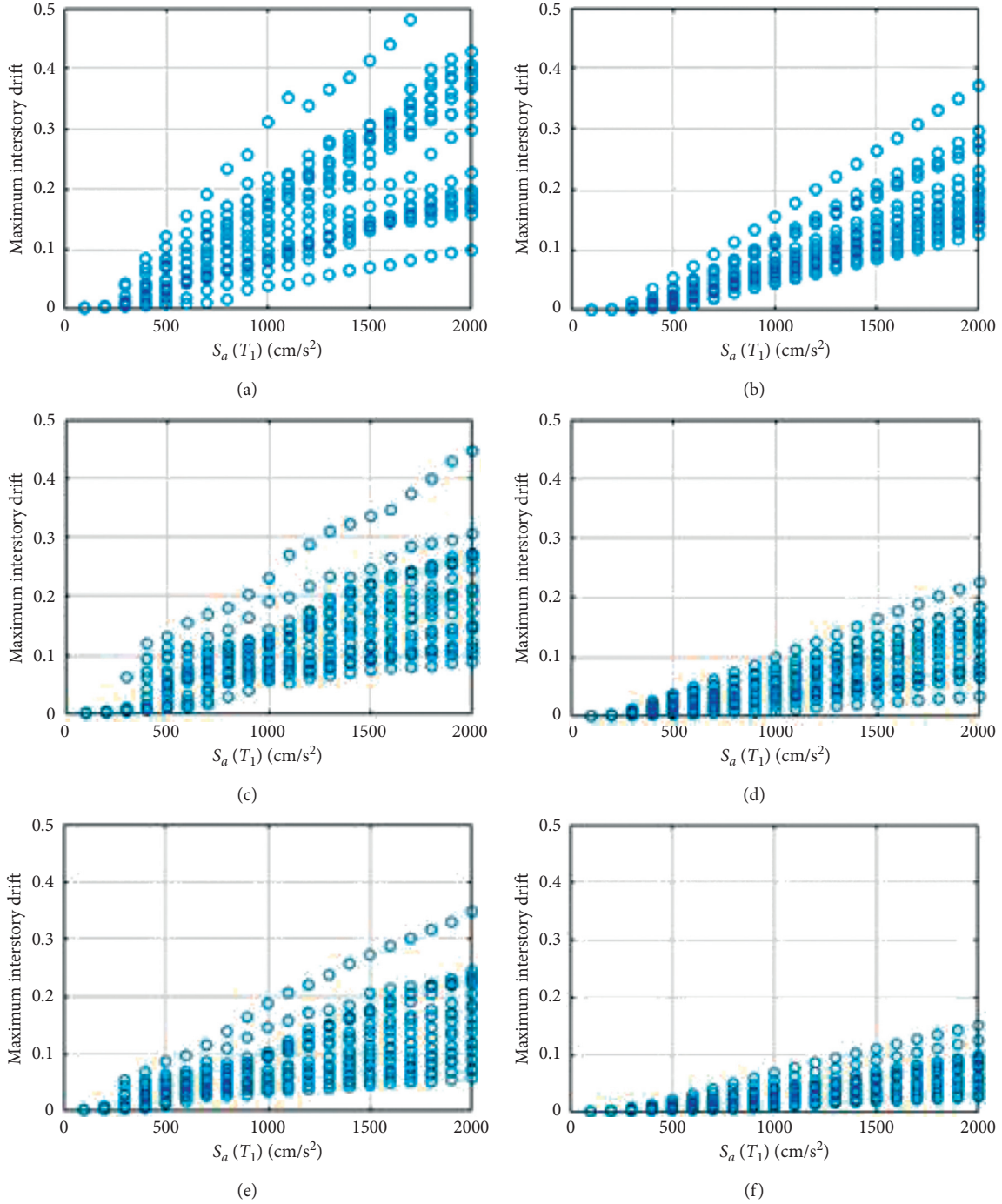


FIGURE 4: Incremental dynamic analysis curves for the buildings: (a) RC3, (b) RC3-BRB, (c) RC6, (d) RC6-BRB, (e) RC9, and (f) RC9-BRB.

indicated that the control of a maximum interstory drift of 0.02 guarantees a good seismic performance. Here, the fragility curves are computed and compared for both selected structural systems using the suggested 0.02 maximum interstory drift value. Figure 7 compares the seismic fragility for the 3, 6, and 9 story levels of RC and RC-BRB buildings. The results suggest that the probability of exceeding the maximum interstory drift is larger for the traditional reinforced concrete frames for all the considered scaling levels in terms of spectral acceleration. For

example, the probability to exceed a peak drift of 0.02 when $S_a(T_1)$ is equal to 1000 cm/s² is 0.8 for the RC3 building, while in the case of the equivalent RC3-BRB structure is about 0.45, indicating that the performance of RC3-BRB is superior in comparison with RC3. The same conclusion is valid for the tallest buildings; in fact, as the level of stories of the buildings increases, the BRBs tend to decrease the probability of exceedance, in such a way that the effectiveness of buckling restrained braces is larger for taller buildings.

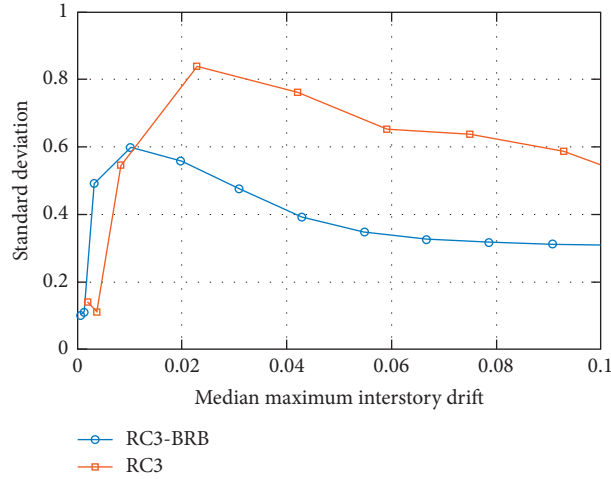


FIGURE 5: Comparison of the standard deviation at different performance levels in terms of the median maximum interstory drift value for the buildings RC3 and RC3-BRB.

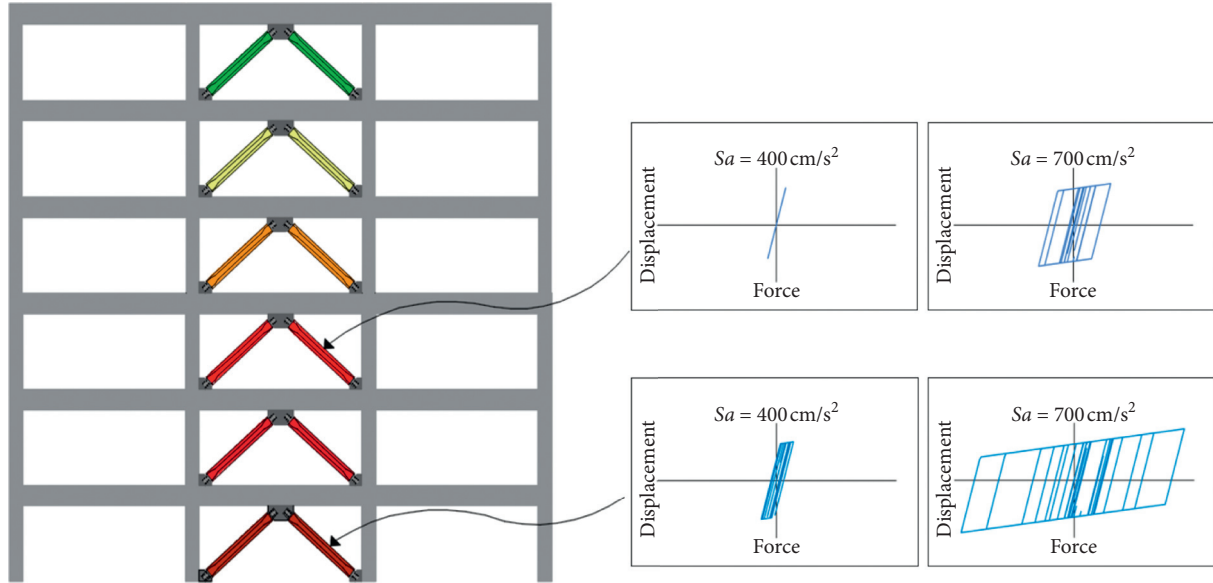


FIGURE 6: Damage configuration of the RC6-BRB and hysteretic curves of the braces for two intensity levels.

4.3. Structural Reliability. The structural reliability is assessed by means of the fragility curves combined with the seismic hazard curves to calculate the mean annual rate of exceedance a maximum interstory drift threshold. For the present study, the spectral acceleration hazard curves corresponding to the first-mode period of vibration of each building and for the *Secretaría de Comunicaciones y Transportes* (SCT) site in Mexico City were developed following the procedure suggested by Alamilla [44]. The seismic hazard curves in terms of peak interstory drift for the RC and the RC-BRB buildings are compared in Figure 8. The figure suggests that the mean annual rate of exceeding a specific value of maximum interstory drift is larger for the traditional reinforced concrete buildings. For this reason, the BRBs on reinforced concrete buildings increase considerably the structural reliability, which is valid for all the

selected buildings. This is especially valid as the number of stories tend to increase as it was indicated in the case of the seismic fragility. The mean annual rate of exceedance a threshold equals 0.02 in terms of MID for the RC and RC-BRB is given in Table 4. Note that it corresponds to target structural reliability levels of buildings designed according to the Mexican Building Code. Thus, the MARE values in terms of peak drift for the BRB buildings are considerably reduced in comparison to those of the RC structures provided by the Mexico City Building Code. In other words, it is observed that the values of the mean annual rates of exceedance for the RC-BRB systems are smaller than those of the traditional RC buildings. Note that there are other structural systems to improve the seismic reliability of buildings such as post-tensioned connections [45]. The results indicate that the use of BRBs in buildings is a good solution in order to reduce

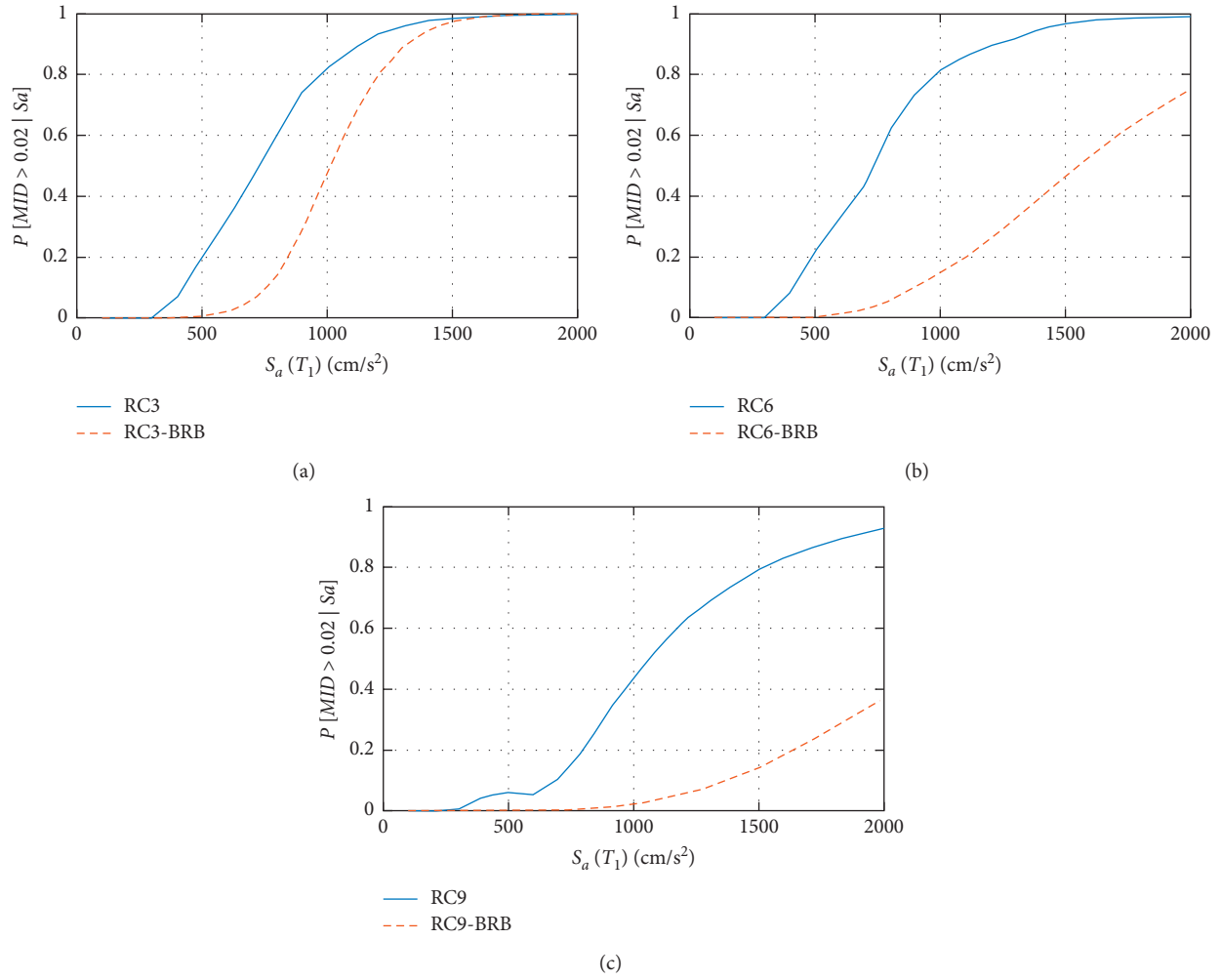


FIGURE 7: Fragility curves for maximum interstory drift and all the studied buildings.

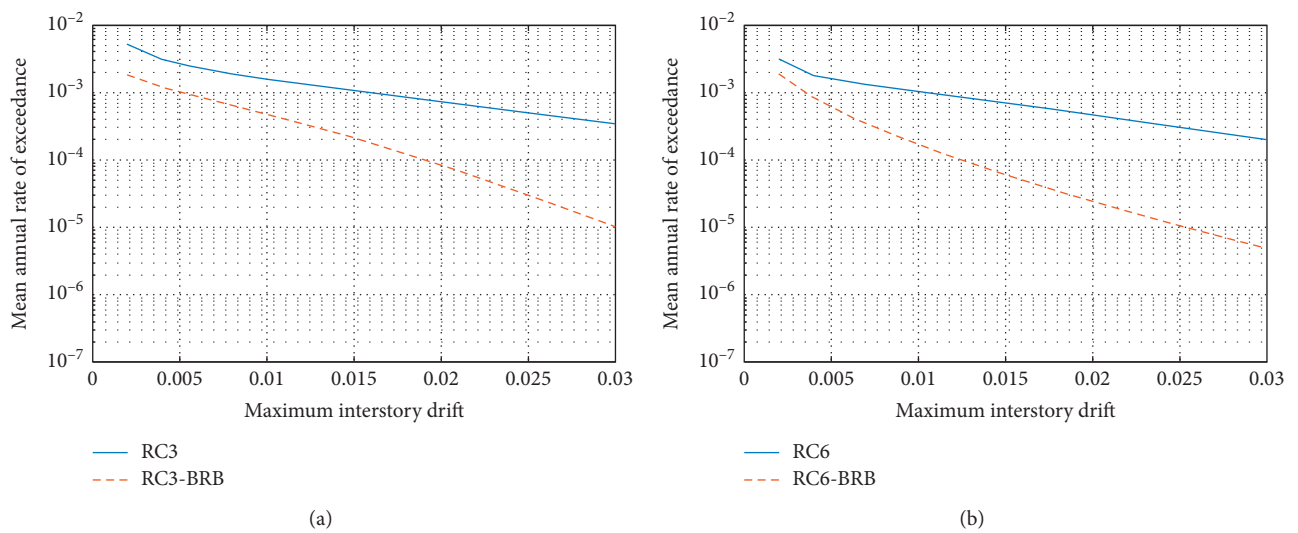


FIGURE 8: Continued.

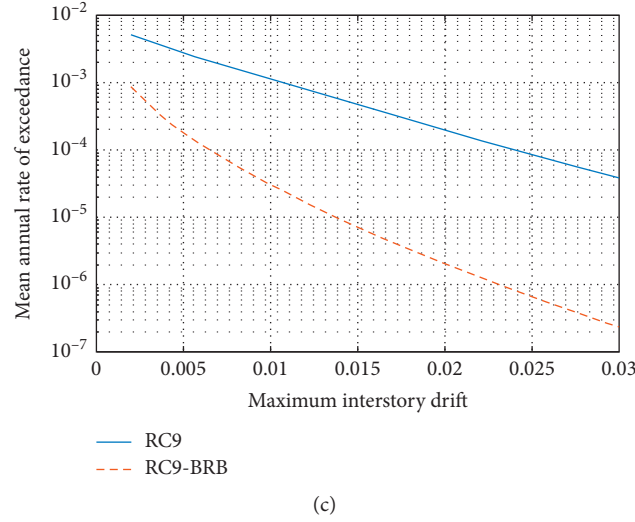


FIGURE 8: Comparison of the *MID hazard* curves for the RC and the RC-BRB buildings with (a) 3 stories, (b) 6 stories, and (c) 9 stories.

TABLE 4: Comparison of the mean annual rate of exceedance (MARE) values for the RC and RC-BRB buildings for a *MID* value equal to 0.02.

RC buildings	MARE for <i>MID</i> = 0.02	RC-BRB buildings	MARE for <i>MID</i> = 0.02
RC3	0.00072	RC3-BRB	0.000084
RC6	0.00046	RC6-BRB	0.000024
RC9	0.00019	RC9-BRB	0.0000024

peak drift demands of traditional structures located in high seismic zones.

5. Conclusions

The seismic performance of three traditional reinforced concrete buildings and equivalent structures with BRBs is assessed through incremental dynamic analysis, seismic fragility, and structural reliability. For this aim, the maximum interstory drift was selected as engineering demand parameter. The buildings were subjected to several narrow-band motions recorded at soft soil of Mexico City. The results indicate that the maximum interstory drift demand is smaller in the case of the RC-BRB buildings in comparison with the reinforced concrete structures. Moreover, the uncertainty in the structural response prediction also tends to decrease when the BRBs are used in the RC buildings. This is reflected in the fragility analysis where the probability of exceeding the maximum interstory drift is larger for the traditional reinforced concrete frames for all the considered scaling levels in terms of $S_a(T_1)$. Finally, the MARE, a specific value of maximum interstory drift, is larger for the traditional reinforced concrete buildings in comparison with the BRB buildings. For this reason, the BRBs on RC buildings increase the structural reliability for all the buildings under consideration. This is particularly valid for the tallest buildings studied. In conclusion, the use of BRBs is a good solution to obtain safer buildings or in order to reduce peak drift demands of traditional structures under strong earthquake ground motions.

Data Availability

The data used to support the findings of this study are available from the corresponding author upon request.

Conflicts of Interest

The authors declare that there are no conflicts of interest regarding the publication of this paper.

Acknowledgments

The financial support given by the Universidad Autónoma de Sinaloa under grant PROFAPI is appreciated. The authors express their gratitude to the *Consejo Nacional de Ciencia y Tecnología* (CONACYT) in Mexico for funding the research reported in this paper under grant Ciencia Básica 287103 and for the scholarships given to the PhD students. The support of the UNAM-DGAPA-PAPIIT under project no. IN100320 is appreciated.

References

- [1] H. Krawinkler and A. Gupta, "Deformation and ductility demands in steel moment frame structures," *Stability and Ductility of Steel Structures*, vol. SDSS'97, pp. 1825–1830, 1998.
- [2] A. Khampanit, S. Leelataviwat, J. Kochanin, and P. Warnitchai, "Energy-based seismic strengthening design of non-ductile reinforced concrete frames using buckling-restrained braces," *Engineering Structures*, vol. 81, pp. 110–122, 2014.

- [3] H. Guerrero, T. Ji, A. Escobar, and A. Terán-Gilmore, "Effects of buckling-restrained braces on reinforced concrete precast models subjected to shaking table excitation," *Engineering Structures*, vol. 163, pp. 294–310, 2018.
- [4] J. Osteraas and H. Krawinkler, "The Mexico earthquake of September 19, 1985—behavior of steel buildings," *Earthquake Spectra*, vol. 5, no. 1, pp. 51–88, 1989.
- [5] H. Kim, *Seismic evaluation and upgrading of braced frame structures for potential local failures*, PhD thesis, p. 290, UMCEE 92-24, Dept. of Civil Engineering and Environmental Engineering, Univ. of Michigan, Ann Arbor, Michigan, 1992.
- [6] R. Tremblay, A. Filiatrault, P. Timler, and M. Bruneau, "Performance of steel structures during the 1994 Northridge earthquake," *Canadian Journal of Civil Engineering*, vol. 22, no. 2, pp. 338–360, 1995.
- [7] Architectural Institute of Japan and Steel Committee of Kinki Branch, *Reconnaissance Report on Damage to Steel Building Structures Observed from the 1995 Hyogoken-Nanbu (Hanshin/Awaji) Earthquake*, p. 167, AIJ, Tokyo, 1995.
- [8] T. Hisatoku, "Reanalysis and repair of a high-rise steel building damaged by the 1995 Hyogoken-Nanbu earthquake," in *Proceedings, 64th Annual Convention, Structural Engineers Association of California*, pp. 21–40, Structural Engineers Association of California, Sacramento, CA, USA, October 1995.
- [9] R. Tremblay, A. Filiatrault, M. Bruneau et al., "Seismic design of steel buildings: lessons from the 1995 Hyogo-ken Nanbu earthquake," *Canadian Journal of Civil Engineering*, vol. 23, no. 3, pp. 727–756, 1996.
- [10] R. Sabelli, S. Mahin, and C. Chang, "Seismic demands on steel braced frame buildings with buckling-restrained braces," *Engineering Structures*, vol. 25, no. 5, pp. 655–666, 2003.
- [11] C. M. Uang and M. Nakashima, "Steel buckling-restrained braced frames," *Earthquake Engineering, Recent advances and applications*, CRC Press, Boca Raton, FL, USA, chapter 16, 2004.
- [12] C. M. Uang and M. Nakashima, *Earthquake Engineering: From Engineering Seismology to Performance Based Engineering*, CRC Press LLC, Boca Raton, FL, USA, 2004.
- [13] Q. Xie, "State of the art of buckling-restrained braces in Asia," *Journal of Constructional Steel Research*, vol. 61, pp. 727–748, 2005.
- [14] G. Della Corte, M. D'Aniello, R. Landolfo, and F. Mazzolani, "Review of steel buckling restrained braces," *Steel Construction*, vol. 4, no. 2, pp. 85–93, 2011.
- [15] S. Kiggins and C. M. Uang, "Reducing residual drift of buckling-restrained braced frames as a dual system," *Engineering Structures*, vol. 28, pp. 1525–1532, 2006.
- [16] M. Bosco, E. Marino, and P. Rossi, "Design of steel frames equipped with BRBs in the framework of Eurocode 8," *Journal of Constructional Steel Research*, vol. 113, pp. 43–57, 2015.
- [17] A. Lago, D. Trabucco, and A. Wood, "Case studies of tall buildings with dynamic modification devices," *Damping Technologies for Tall Buildings*, Elsevier, Amsterdam, Netherlands, chapter 8, 2018.
- [18] G. Palazzo, F. Lopez-Almansa, X. Cahis, and F. Crisafulli, "A low-tech dissipative buckling restrained brace. Design, analysis, production and testing," *Engineering Structures*, vol. 31, pp. 2152–2161, 2009.
- [19] Mexico City Building Code 2017.
- [20] K. Deb, *Multi-objective Optimization Using Evolutionary Algorithms*, John Wiley & Sons, Chichester-New York-Winheim-Brisbane-Singapore-Toronto, 2001.
- [21] K. Deb, A. Pratap, S. Agarwal, and T. Meyarivan, "A fast and elitist multiobjective genetic algorithm: NSGA-II," *IEEE Transactions on Evolutionary Computation*, vol. 6, no. 2, pp. 182–197, 2002.
- [22] J. Avilés and L. Pérez-Rocha, "Damage analysis of structures on elastic foundation," *Journal of Structural Engineering*, vol. 133, no. 10, pp. 1453–1461, 2007.
- [23] S. Abdel, M. Ahmed, and T. Alazrak, "Evaluation of soil-foundation-structure interaction effects on seismic response demands of multi-story MRF buildings on raft foundations," *International Journal of Advanced Structural Engineering*, vol. 7, no. 1, pp. 11–30, 2014.
- [24] A. Wada, E. Saeki, T. Takeuchi, and A. Watanabe, *Development of Unbounded Brace*, Nippon Steel Corporation Building Construction and Urban Development Division, Tokyo, Japan, 1998.
- [25] A. Terán-Gilmore and N. Virto-Cambray, "Preliminary design of low-rise buildings stiffened with buckling restrained braces by a displacement-based approach," *Earthquake Spectra*, vol. 25, no. 1, pp. 185–211, 2009.
- [26] H. Guerrero, T. Ji, and J. Escobar, "Experimental studies of a steel frame model with and without buckling-restrained braces," *Revista de Ingeniería Sísmica*, vol. 95, pp. 33–52, 2016.
- [27] R. Rahnnavard, M. Naghavi, M. Aboudi, and M. Suleiman, "Investigating modeling approaches of buckling-restrained braces under cyclic loads," *Case Studies in Construction Materials*, vol. 8, pp. 476–488, 2018.
- [28] A. Almeida, R. Ferreira, J. Proenca, and A. Gago, "Seismic retrofit of RC building structures with buckling restrained braces," *Engineering Structures*, vol. 130, pp. 14–22, 2017.
- [29] R. Tremblay, P. Bolduc, R. Neville, and R. DeVall, "Seismic testing and performance of buckling restrained bracing systems," *Canadian Journal of Civil Engineering*, vol. 33, pp. 183–198, 2006.
- [30] A. Terán-Gilmore and J. Ruiz-García, "Comparative seismic performance of steel frames retrofitted with buckling buckling-restrained braces through the application of force-based and displacement-based approaches," *Soil Dynamic and Earthquake Engineering*, vol. 31, no. 3, pp. 478–490, 2011.
- [31] J. Holland, *Adaptation in Natural and Artificial Systems. An Introductory Analysis with Applications to Biology, Control and Artificial Intelligence*, University of Michigan Press, Ann Arbor, Mich, 1975.
- [32] M. Barraza, E. Bojórquez, E. Fernández-González, and A. Reyes-Salazar, "Multi-objective optimization of structural steel buildings under earthquake loads using NSGA-II and PSO," *KSCE Journal of Civil Engineering*, vol. 21, pp. 488–500, 2017.
- [33] M.-D. Yang, M.-D. Lin, Y.-H. Lin, and K.-T. Tsai, "Multi-objective optimization design of green building envelope material using a non-dominated sorting genetic algorithm," *Applied Thermal Engineering*, vol. 111, pp. 1255–1264, 2017.
- [34] S. Bakhshinezhad and M. Mohebbi, "Multi-objective optimal design of semi-active fluid viscous dampers for nonlinear structures using NSGA-II," *Structures*, vol. 24, pp. 678–689, 2020.
- [35] H. Leyva, E. Bojórquez, J. Bojórquez et al., "Earthquake design of reinforced concrete buildings using NSGA-II," *Advances in Civil Engineering*, vol. 2018, Article ID 5906279, 11 pages, 2018.
- [36] E. Bojórquez and S. E. Ruiz, "Strength reduction factors for the valley of Mexico taking into account low cycle fatigue effects," in *Proceedings of 13th World Conference on*

- Earthquake Engineering*, Vancouver, BC, Canada paper 516, Vancouver, BC, Canada, August 2004.
- [37] A. Terán-Gilmore and J. O. Jirsa, "Energy demands for seismic design against low cycle fatigue," *Earthquake Engineering and Structural Dynamics*, vol. 36, pp. 383–404, 2007.
 - [38] M. D. Trifunac and A. G. Brady, "A study of the duration of strong earthquake ground motion," *Bulletin of the Seismological Society of America*, vol. 65, no. 3, pp. 581–626, 1975.
 - [39] D. Vamvatsikos and C. A. Cornell, "Incremental dynamic analysis," *Earthquake Engineering and Structural Dynamics*, vol. 31, no. 3, pp. 491–514, 2002.
 - [40] G. G. Deierlein, *Overview of a Comprehensive Framework for Performance Earthquake Assessment*, Report PEER 2004/05, pp. 15–26, Pacific Earthquake Engineering Center, Berkeley, CA, USA, 2004.
 - [41] E. Bojórquez and J. Ruiz-García, "Residual drift demands in moment-resisting steel frames subjected to narrow-band earthquake ground motions," *Earthquake Engineering and Structural Dynamics*, vol. 42, pp. 1583–1598, 2013.
 - [42] E. Bojórquez, A. Terán-Gilmore, S. E. Ruiz, and A. Reyes-Salazar, "Evaluation of structural reliability of steel frames: interstory drift versus plastic hysteretic energy," *Earthquake Spectra*, vol. 27, no. 3, pp. 661–682, 2011.
 - [43] E. Bojórquez and I. Iervolino, "Spectral shape proxies and nonlinear structural response," *Soil Dynamics and Earthquake Engineering*, vol. 31, no. 7, pp. 996–1008, 2011.
 - [44] J. L. Alamilla, *Reliability-based Seismic Design Criteria for Framed Structures*, PhD Thesis, Universidad Nacional Autónoma de México, UNAM, Mexico, 2001.
 - [45] E. Bojórquez, A. López-Barraza, A. Reyes-Salazar et al., "Improving the structural reliability of steel frames using posttensioned connection," *Advances in Civil Engineering*, vol. 2019, Article ID 8912390, 10 pages, 2019.

Research Article

A Structural Configuration with Separate Substructures towards Reducing the Seismic Damage of Spatial Structures with Rectangular Plan

Dabin Yang ^{1,2}, Litai Sun,¹ Hao Wang ¹, Lei Liu,¹ Mingjin Li,¹ and Xiangyi Sun¹

¹School of Civil Engineering, Shandong Jianzhu University, Jinan 250101, China

²Key Laboratory of Building Structural Retrofitting and Underground Space Engineering (Shandong Jianzhu University), Ministry of Education, Beijing, China

Correspondence should be addressed to Hao Wang; wanghao19@sdjzu.edu.cn

Received 8 July 2020; Revised 23 September 2020; Accepted 30 September 2020; Published 13 October 2020

Academic Editor: Sonia E. Ruiz

Copyright © 2020 Dabin Yang et al. This is an open access article distributed under the Creative Commons Attribution License, which permits unrestricted use, distribution, and reproduction in any medium, provided the original work is properly cited.

Seismic damage of spatial structures of rectangular plan with RC substructures was observed in several earthquakes, especially in the RC substructures. In order to reduce the seismic damage potential, a new structural configuration of spatial structure of rectangular plan is proposed, the substructures of which are composed of the steel substructure and the RC substructure. The latter only bears the vertical load of roof by the arrangement of horizontal sliding bearings between the roof and the RC substructure. The pushover analyses are performed on a steel braced frame and an RC frame with similar lateral stiffness, and the results show that the lateral capacity of the steel structure is much larger than those of the RC structures. A spatial structure of rectangular plan with two different substructures is designed according to Chinese structural designing codes. Seismic time history analyses are carried out for the spatial structure under five ground motions. The results show that the damage mainly concentrates on the substructures, and the seismic performance of the structure with steel and RC substructures is much better than that of the structure with RC substructures.

1. Introduction

Spatial structures have been widely used in gymnasias, public halls, auditorium, and stadiums. In most cases, a typical spatial structure consists of two parts: upper roof and substructure, and the roof is usually in the structural form of steel spatial structures including flat spatial truss or latticed shell, while the latter tends to be the reinforced concrete (RC) structures. The seismic performance of roofs will be greatly influenced by substructures [1–3]. Although it has been proven by many earthquakes that the seismic damage of spatial structures is relatively light compared with the multistory structures, the damages are reported in several earthquakes [4–9], especially in the structural part around roof bearings and RC substructures.

In the Hanshin-Awaji Earthquake in 1995 in Japan, the structural damage to spatial structures was mainly observed

in the RC substructures, while damage to steel roof structures was comparatively minor [4]. The damage of an RC column in a school gymnasium with rectangular plan is shown in Figure 1 [4].

In 2011, Tohoku earthquake with the magnitude of 9.0 hit Japan. Even more severe damages to spatial structures than ever before were observed. Other than the roof damage, the roof bearings and RC substructures supporting steel roofs were extensively damaged according to the Joint Editorial Committee for the Report on the Great East Japan Earthquake Disaster [9], some of which are shown in Figure 2. In the earthquake, the spherical latticed domes including their substructures were seldom damaged, and most of the damaged spatial structures were in the form of rectangular plan, regardless of the roof type of cylindrical latticed shells, flat spatial trusses, and chevron moment frames.

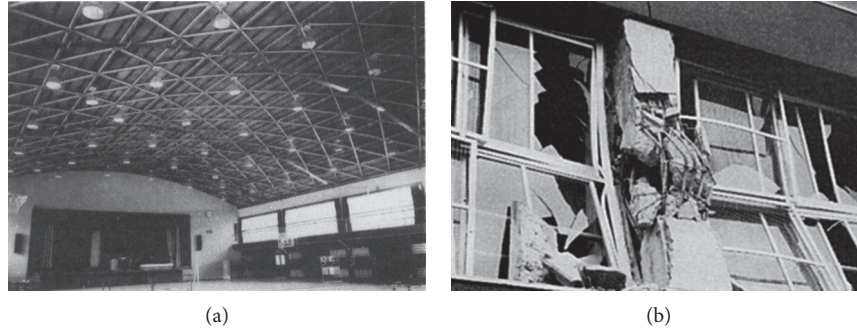


FIGURE 1: Damage of an RC column of a school gymnasium in Hanshin-Awaji earthquake. (a) Interior view of the high school gym. (b) Damage of a column in the gym.

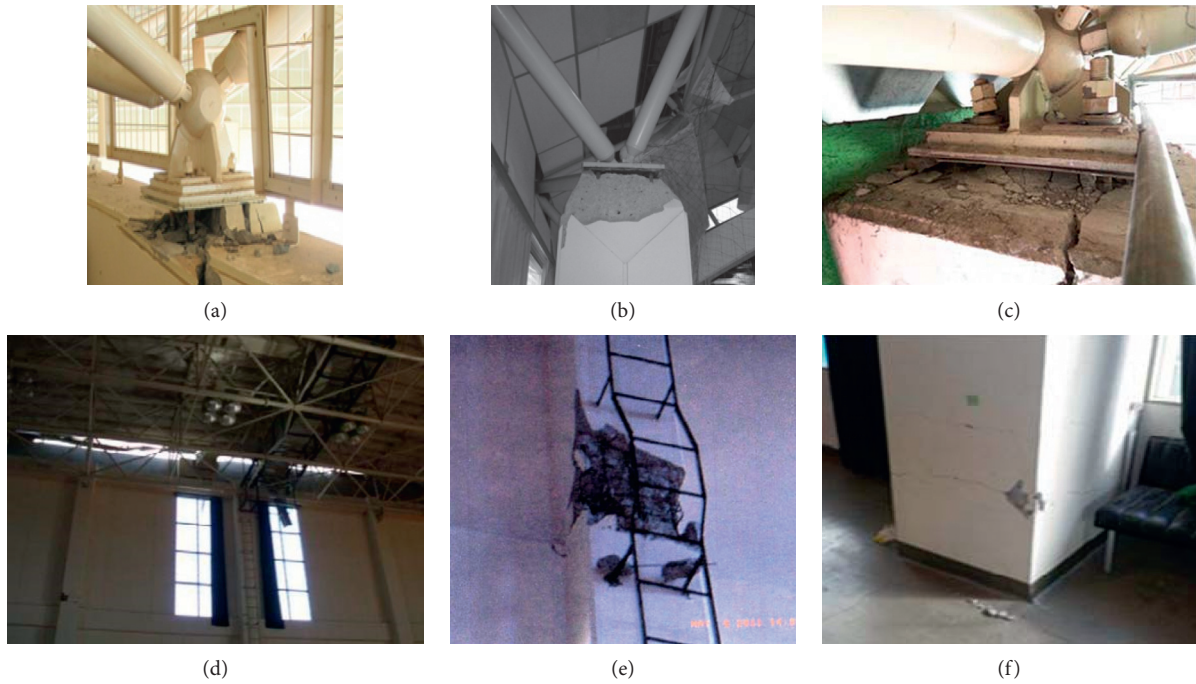


FIGURE 2: Damage of bearings and RC columns of spatial structures in Tohoku earthquake. (a) Bearing-1, (b) bearing-2, (c) bearing-3, (d) column middle-1, (e) column bottom-2, and (f) column bottom-1.

Most of spatial structures tend to be used as shelters for refugees in the event of earthquake, so their seismic performance level should be enhanced compared with ordinary structures, and it is expected to be immediately used without any need of repair after earthquakes. As mentioned above, most of the substructures of spatial structures are RC structures due to the lesser cost of RC compared with steel, but it is well known that the seismic performance of steel structures is much better than that of RC structures. In order to reduce the seismic damage potential, a new structural configuration of spatial structures with rectangular plan is proposed, the substructures of which are composed of two parts: the steel substructure bearing the horizontal and vertical loads of roof and the RC substructure only bearing the vertical load of roof. The seismic performances are studied by static pushover analyses and seismic time history analyses under different ground motions.

2. Structural Configuration and FE Models

2.1. Basic Principle of Structural Configuration. Generally speaking, the RC structure has a relatively high capacity on compression but a low capacity on bending. The basic principle of the structural configuration is to divide the substructures into two separate parts, the steel substructure and the RC substructure, in which the former bears the horizontal and vertical loads of the roof, and the latter only bears the vertical load of the roof by the arrangement of horizontal sliding connections of the RC substructure and the roof. Therefore, the horizontal seismic forces of the roof can only be transferred to the steel substructure rather than the RC substructure by this kind of configuration, so the shear force and the bending moment of the RC substructure can be significantly reduced. However, the steel substructure should be strong enough to retain necessary strength and

stiffness due to the horizontal seismic forces, so high-strength steel cables are used as the diagonal braces. The seismic performance of single-layer latticed domes with separate substructures in accordance with this structural configuration principle is proven to be excellent [10], but the seismic performance of the spatial structure with the rectangular plan has not been studied. Furthermore, it is different and more complicated than the dome-shaped spatial structure in terms of structural configuration.

2.2. FE Models. SAP2000 V19 is used for FE models. A spatial structure with the rectangular plan of $64\text{ m} \times 48\text{ m}$ and the substructure height of 9 m is taken as the structural model. As to the roof, a single-layer latticed shell with the height of 9.6 m is selected as the structural form, and the geometrical modeling procedure in sequence is shown in Figure 3. In the first step shown in Figure 3(a), the plan is meshed into 16×12 squares with the side length of 4 m , and the coordinate origin, point O, is taken as the central point of the plan, and points A ~ D are the middle points of each side, respectively. Lines OA and OD are in the positive directions of x -axis and y -axis, respectively. Then point T is determined by elevating point O by 9.6 m along the positive direction of z -axis, and the circular arcs ATB and CTD are drawn in the second step. Seven arcs in vertical plans passing through the 14 points along the longer side of the plan and the arc AT are depicted, as is shown in Figure 3(c). Vertical lines are drawn from the square points till the intersections with the eight arcs in the former step; thus all the intersections and the corresponding points in the plan sides are connected to form 1/4 part of the latticed shell in the 5th step. Finally, the whole latticed shell is created by mirroring the 1/4 part of the latticed shell, as shown in Figure 3(e).

For the structure with steel and RC substructures, the RC substructures are connected with the roof shell by horizontal sliding bearings, so the horizontal boundary constraint stiffness for the shell will only be provided by steel substructure. In order to maintain the necessary horizontal boundary constraint stiffness of the latticed shell, a boundary beam structure in the plan ABCD shown in Figure 4 is implemented in the structure.

Two kinds of substructures are considered: steel and RC substructures shown in Figure 5 and RC substructures shown in Figure 6, and the bird views and two side views of the whole structure with steel and RC substructures are depicted in Figure 7. All the column intervals are 8 m and both steel and RC beams are in the height of 8 m for both cases. For the case of steel and RC substructures, the same steel substructures distribute in the four corners, comprising steel columns with fixed bottoms, steel beams with flexible connections with the columns, and tension-only concentric braces, and all the steel column tops are pin-connected with the roof members. All the RC column bottoms are fixed on the ground. Equal constraints in SAP2000 shown in Figure 8 are used for modeling the horizontal sliding bearings: the vertical DOFs (degrees of freedom) of column tops are constrained with corresponding roof joints in the same locations, and the other five DOFs of the two joints

remain independent; thus, the horizontal sliding effects can be simulated.

The masses and gravity of members are automatically considered by SAP2000. Super dead load of 0.5 kN/m^2 and live load of 0.5 kN/m^2 for the latticed shell are considered in the design to determine member sections, and the super dead load is converted to nodal masses during the seismic time history analyses. All the member sections are determined according to Chinese structural designing codes [11–14]. The stress-strain relation of the tension-only steel brace of high-strength cable is shown in Figure 9 [15], of which Young's modulus, yield stress, and ultimate stress are $1.9 \times 10^5\text{ MPa}$, 1764 MPa , and 1960 MPa , respectively [16]. All the other steel members are of the steel grade Q345 with Young's modulus of $2.05 \times 10^5\text{ MPa}$ and yield stress of 345 MPa . As shown in Figure 10, all the roof members and boundary beams are of rectangular pipe sections, of which the weaker axes are the roof surface normals. The member sections of the steel substructure are shown in Table 1. The concrete grade for all the RC structures is the widely used C40 in China, with the design value of axial compressive strength being 19.1 MPa . The member sections and reinforcement configurations of the RC substructure are shown in Figure 11, and the reinforcements of RC column and corner column are listed in Table 2, where three levels of reinforcements, R0, R1, and R2, are presented, all of which can meet the designing requirements of Chinese structural designing codes above, and ρ , the ratio of longitudinal reinforcement of R2 level for RC column, is a little larger than the maximum limit, 5%, prescribed in the Chinese code for design of concrete structures [11]. In the structural FE models, the shorter side of each RC column is parallel to the axial line of the RC beam connected.

2.3. Dominant Vibration Modes. SS-SRC and SS-RC are used to label the structure with steel and RC substructures and the structure with RC substructures below.

For both of the two structures with different substructures, as shown in Figure 12, the vibration shapes of the first two modes are the horizontal vibration in y -direction and x -direction, respectively, whose modal participating mass ratios M_x , M_y , and M_z in the three directions are listed in Table 3. It is obvious that the first two vibration modes are the dominant modes for seismic responses, since the modal participating mass ratios are relatively large, especially for the structure with RC substructures. It is worth noting that the RC substructures in the SS-SRC structure remain stationary in the first two vibration modes, as shown in Figures 12(a) and 12(b), which results in less modal participating mass ratios than those of SS-RC structure. The periods of the first two modes are close for the two structures, which suggests that the lateral stiffnesses are almost the same.

2.4. Static Pushover Analyses. To illustrate the comparison of steel substructure and RC substructure, static pushover analyses are performed on two structures shown in Figure 13. The steel structures are composed of steel column

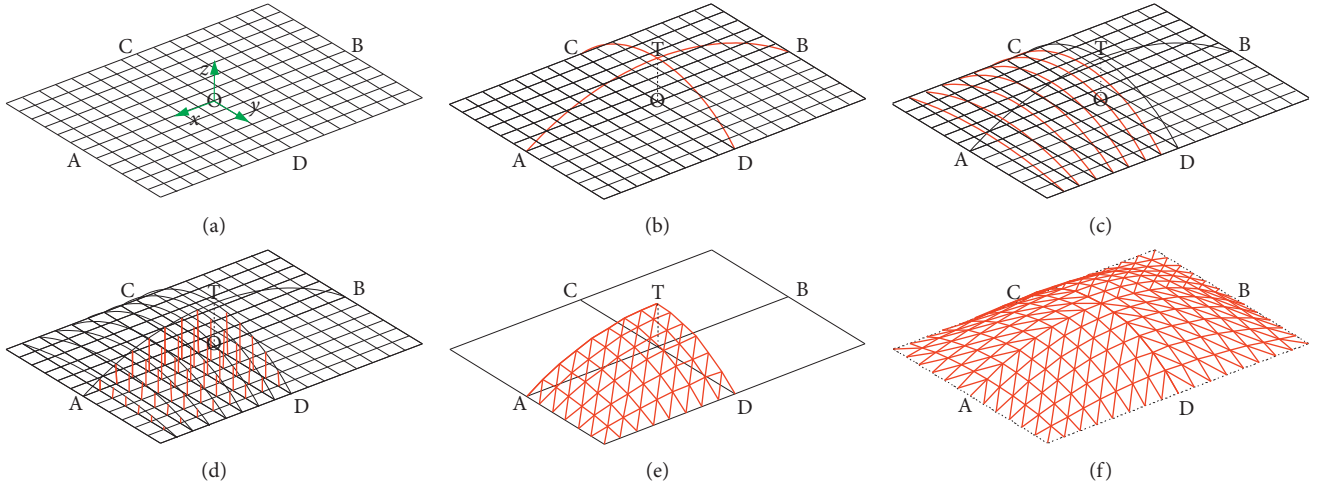


FIGURE 3: Geometrical modeling procedure of roof. (a) 1st step, (b) 2nd step, (c) 3rd step, (d) 4th step, (e) 5th step, and (e) 6th step.

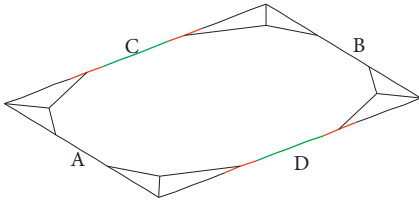


FIGURE 4: Boundary beam structure of the latticed shell.

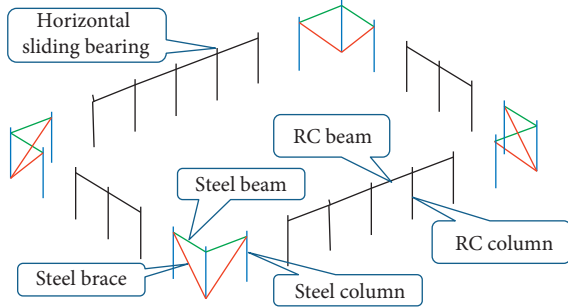


FIGURE 5: Steel and RC substructures.

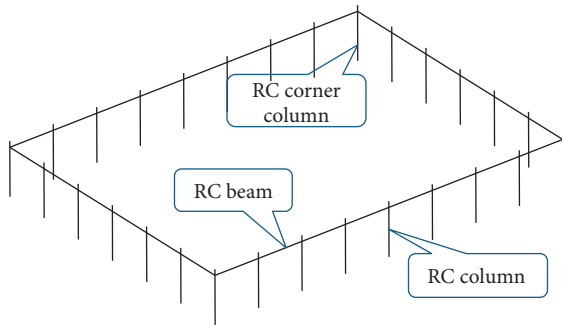


FIGURE 6: RC substructures.

with fixed bottoms, steel beam with flexible connections with the columns, and tension-only concentric brace, and all the sections and materials are the same as shown in Table 1.

Similarly, the RC columns and beams in the pushover models have the same sections and materials presented in Figures 11(a) and 11(c) and Table 2, and the numbers of RC columns and beams are determined according to the lateral stiffness of the steel structure; that is, the lateral stiffnesses of the steel structure and the RC structure are almost same. According to the Chinese code for design of concrete structures [11], the axial compression ratio of RC column, R_{ac} , is defined as

$$R_{ac} = \frac{N}{f_c A_c}, \quad (1)$$

where N and f_c are the compression force and the design value of axial compressive strength of the RC column. Three different compression forces are calculated according to equation (1) when R_{ac} is 0, 0.2, and 0.4, respectively, and then they are applied on the column tops of the two kinds of structures.

The plasticity is usually considered by plastic hinges in SAP2000. As shown in Figure 14, the force-deformation behavior of a plastic hinge is defined by five points labeled A, B, C, D, and E, which denote the origin, yielding, ultimate capacity, residual strength, and total failure. Three additional deformation measures at points IO (immediate occupancy), LS (life safety), and CP (collapse prevention) are also presented in SAP2000 for different automatic hinges. Different performance levels are represented by different colors in postprocess, as shown in Figure 14. All the automatic hinge properties of different sections and load conditions implemented in SAP2000 V19 are described in ASCE 41-13 [17]. In the pushover analyses, the PMM hinge defined in ASCE 41-13 [17] is designated on the two ends of the steel columns and RC columns, and M hinge defined in ASCE 41-13 [17] is designated on the two ends of the RC beam. The hinge of steel braces is also defined according to ASCE 41-13 [17] based on the nonlinear relations in Figure 9.

The relations of lateral forces and lateral displacements on the column tops are depicted in Figure 15. It can be seen that the elastic capacity of the steel structure is much larger than those of the RC structures, irrespective of the

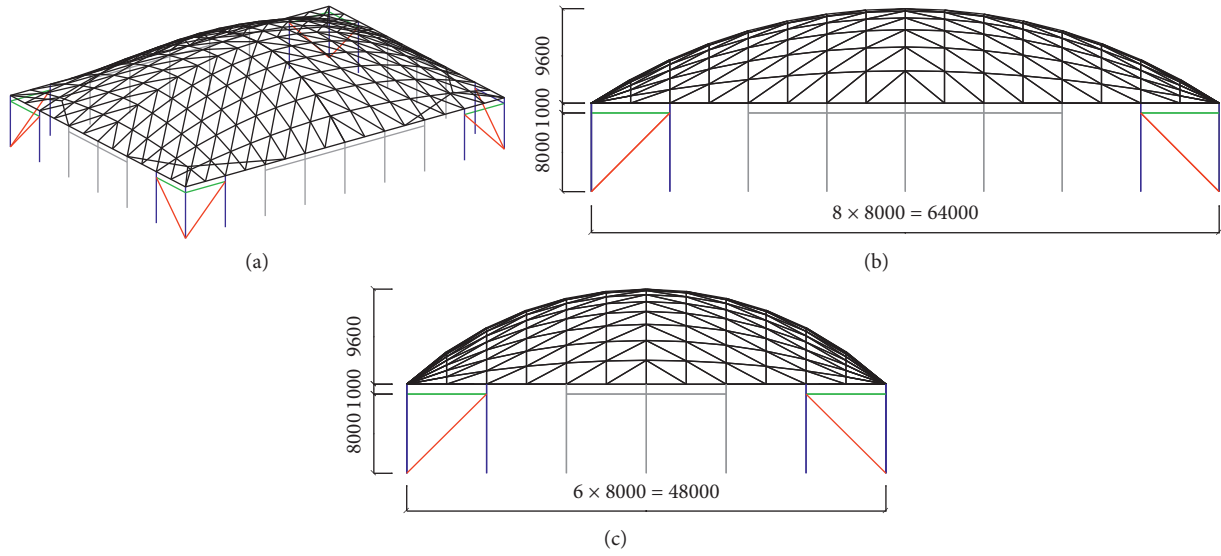


FIGURE 7: Whole structure with steel and RC substructures. (a) Bird view, (b) side view-1, and (c) side view-2.

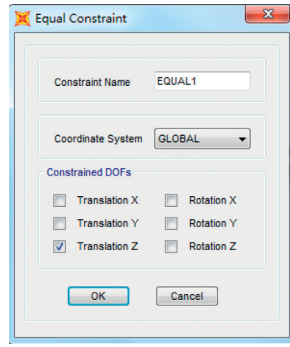


FIGURE 8: Equal constraints for modeling the horizontal sliding bearings.

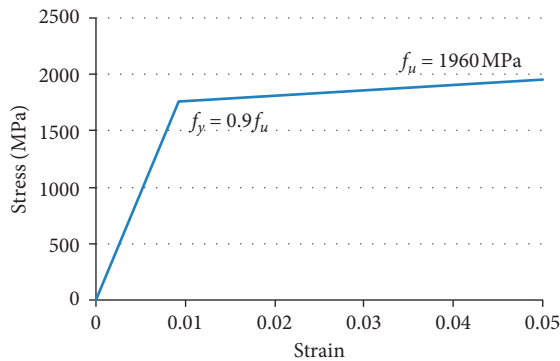


FIGURE 9: Stress-strain relation of steel braces under tension.

reinforcements of the columns. The calculation results show that the transfer points from elastic to plastic in the pushover curves of steel structure correspond to the yielding point of steel braces; that is, the high elastic capacity of steel structure is mainly creditable to the high strength of steel braces. For RC structures, more reinforcements in the columns will increase the lateral force capacity, which basically decreases with the increase of the vertical loads applied.

2.5. Seismic Analyses. Seismic time history analyses under different ground motions are performed to compare the seismic performances of the two kinds of structures. Because the R1 reinforcement is the most commonly used reinforcement level in structural design practice, only the R1 reinforcement is used for the RC columns of both structures in the comparison. Other than the hinges mentioned above, the automatic PMM hinges are designated on the two ends and middle points of the roof including the beam ring members. By assuming damping ratio as 0.035 [14] due to the structure including steel and RC, Rayleigh damping with two coefficients calculated by the periods of the first two vibration modes is used. The Hilber-Hughes-Taylor method with α as zero is used in the analyses, in which P -delta and large displacements effects are considered.

2.6. Ground Motions. As shown in Table 4, five ground motions in three directions are selected as the input seismic accelerations, in which the first one is one of the ground motions in the Tohoku earthquake recorded in Fukushima, the prefecture where many spatial structures with RC substructures were damaged by seismic ground motions in the earthquake according to the Joint Editorial Committee for the Report on the Great East Japan Earthquake Disaster [9]. All the accelerations in the three directions are not scaled, and the maximum horizontal PGA (peak ground acceleration) of the acceleration is 1069 gal, which is inputted in y -direction shown in Figure 3(a). Zhai and Xie [18] recommended the most unfavorable real seismic design ground motions for rock, stiff soil, medium soil, and soft soil site conditions in terms of three typical period ranges of structures, and one of the five ground motions in each group for the middle-period (0.5–1.5 s) structures is selected as the next four ground motions listed in Table 4, which are expected to result in severe damage for the structure with dominant vibration modal periods from 0.5 s to 1.5 s on rock, stiff soil, medium soil, and soft soil site conditions.

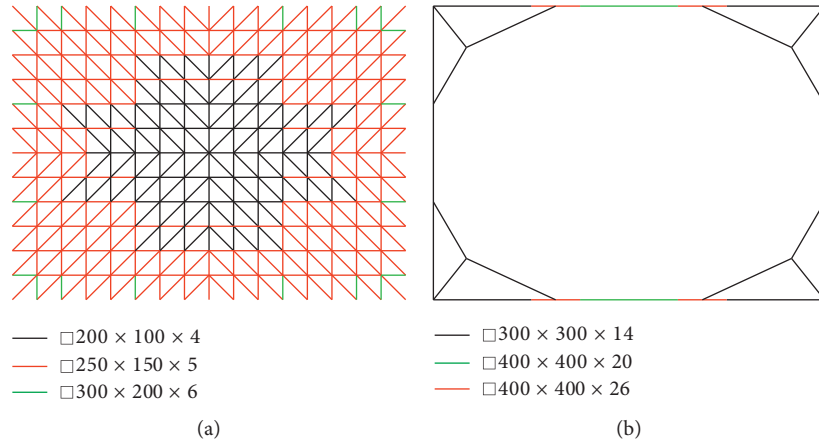


FIGURE 10: Member sections of the latticed shell. (a) Roof members; (b) boundary beam structure.

TABLE 1: Steel member sections and yield stresses.

Member	Section (mm)	Steel grade	Yield stress (MPa)
Steel column	$\square 400 \times 400 \times 16$	Q345	345
Steel beam	H400 \times 200 \times 8 \times 13	Q345	345
Steel brace	$\varnothing 50$	1960	1764

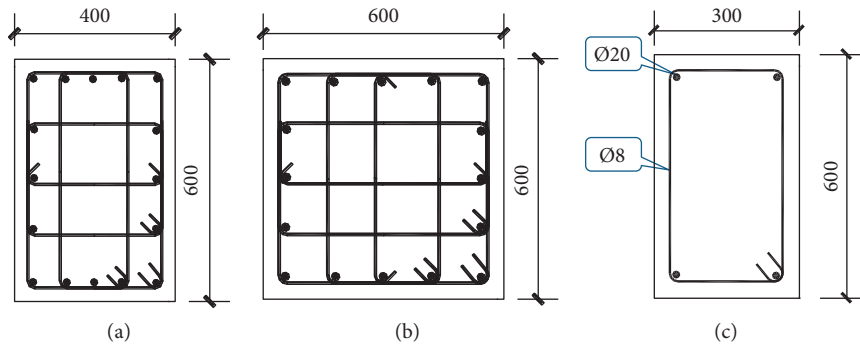


FIGURE 11: RC member sections and reinforcement configurations. (a) RC column, (b) RC corner column, and (c) RC beam.

TABLE 2: Reinforcements of RC column and RC corner column.

Level	Longitudinal reinforcement (mm)	Transverse reinforcement (mm)	ρ of RC column (%)	Steel grade	Yield stress (MPa)
R0	$\varnothing 18$	$\varnothing 8@100$	1.7	HRB400	400
R1	$\varnothing 25$	$\varnothing 12@100$	3.3	HRB400	400
R2	$\varnothing 32$	$\varnothing 14@100$	5.4	HRB400	400

* $\rho = A_s/A_c$, where A_s and A_c are the areas of longitudinal reinforcement and column section, respectively.

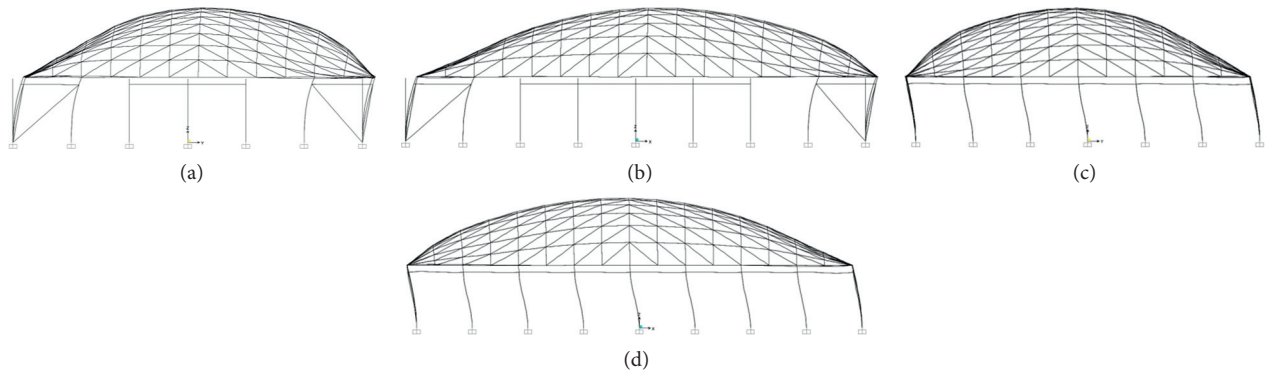


FIGURE 12: The first two vibration modes. (a) 1st mode of SS-SRC; (b) 2nd mode of SS-SRC; (c) 1st mode of SS-RC; (d) 2nd mode of SS-RC.

TABLE 3: The first two modal participating mass ratios.

Structure	Mode	Period (s)	M_x	M_y	M_z
SS-SRC	1	0.591	0	0.75	0
	2	0.572	0.77	0	0
SS-RC	1	0.612	0	0.96	0
	2	0.585	0.98	0	0

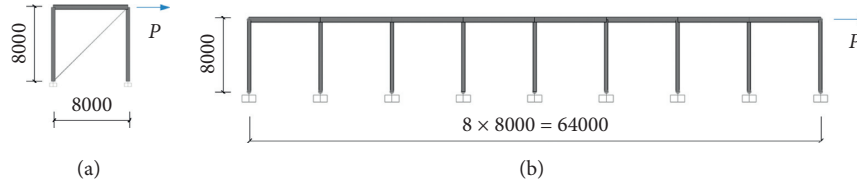


FIGURE 13: Pushover models. (a) Steel structure; (b) RC structure.

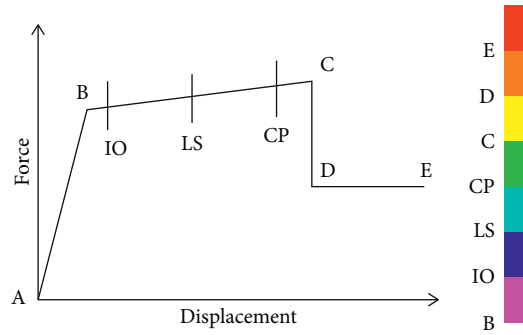


FIGURE 14: Force-deformation behavior of hinge.

Each group of accelerations of three directions is scaled in the same ratio, and the larger PGA of the two horizontal accelerations for each ground motion is scaled to 700 gal and inputted in y -direction. The pseudoacceleration response spectrums of all the scaled accelerations in y -direction are shown in Figure 16. It can be seen that, from 0 s to 0.6 s, the period range of the spatial structures, Kobe's ground motion is the largest, so the structures are expected to be damaged most severely under Kobe's ground motion among all the five ground motions.

3. Results

All the roof members including the boundary beam structure and all the steel braces remain elastic under all the ground motions. The maximum axial stresses of the latticed shell members and the maximum resultant displacements of the latticed shells are illustrated in Figures 17 and 18. It can be seen that both the maximum axial stresses of the latticed shell members in SS-RC and SS-SRC structures are lower than the yielding strength. The maximum resultant displacements of the latticed shells in SS-RC and SS-SRC structures are close, except in the case of Kobe earthquake, where the displacement of SS-RC is much larger than that of SS-SRC, and this large discrepancy will be explained below.

The final plastic hinges of different levels under all the ground motions for substructures are shown in Figure 17. It is clear that the damage of the SS-RC structures is much larger

than that of the SS-SRC structures. For the SS-RC structures, hinges with the state after E occur under all the ground motions except the Mammoth Lakes ground motion, while the hinges remain in state B-IO under all the ground motions except Kobe's ground motion for the SS-SRC structures. Therefore, except Kobe's ground motion, the SS-SRC structures can be used as refugee shelters without any repair, while the SS-RC structures need to be retrofitted on many members because the hinges beyond state IO occur under all the ground motions. As mentioned before, the most severe damage occurs under Kobe's ground motion: other than several hinges with the state after E, all the column bottoms of the SS-RC structure reach the hinge state C-D, that is, beyond the ultimate capacity, while for the SS-SRC structure, all the hinges in the RC columns remain in state B-IO except two IO-LS hinges, and two IO-LS hinges appear in the steel columns.

The maximum resultant lateral displacements of the RC column tops in the two kinds of structures are depicted in Figure 19, from which the lateral displacements of the RC column tops in the RC structures are larger than those of the SRC structures, the comparative relation of which is the same as that of plastic hinge states shown in Figure 20. In the SS-RC structures, all the horizontal seismic forces and displacements due to the roof weight will be transferred to the RC columns, while those forces and displacements will only be transferred to the steel substructures in SS-SRC structures, and the RC substructures only bear the horizontal forces and displacements due to self-weight and parts of the

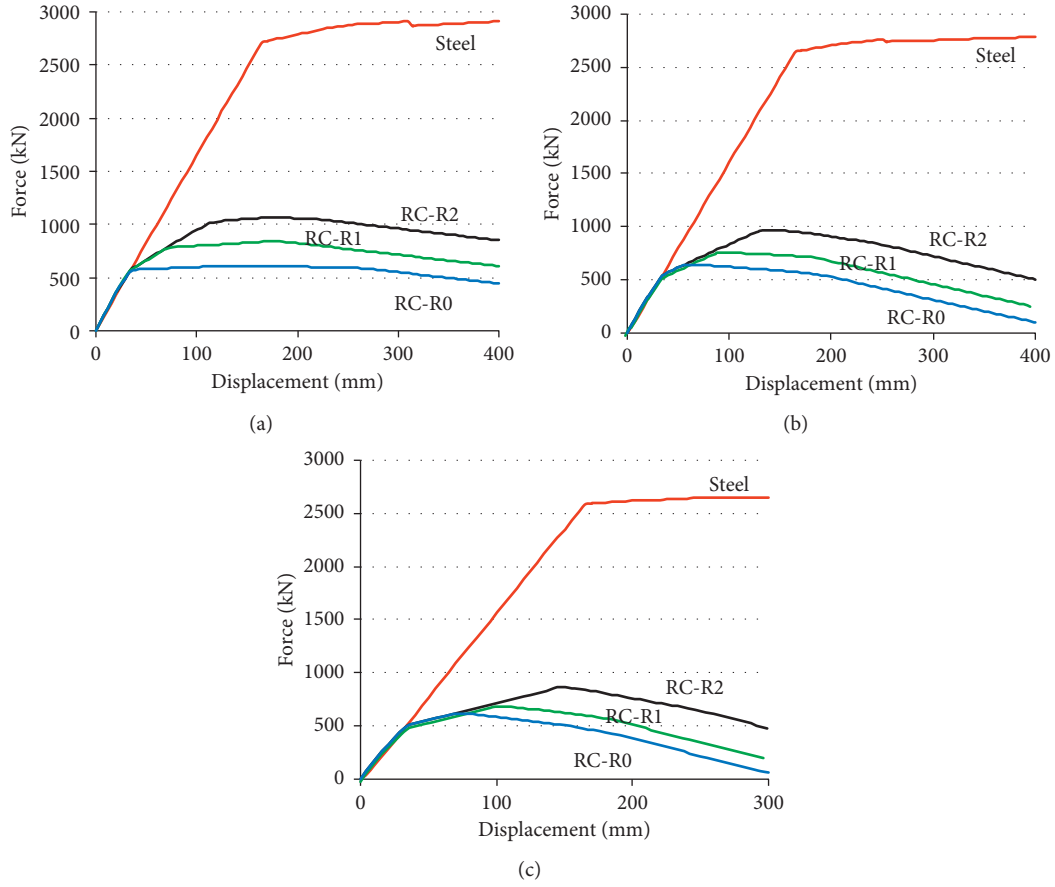


FIGURE 15: Force displacement of pushover analyses under different axial compression ratio of RC column R_{ac} . (a) $R_{ac} = 0$, (b) $R_{ac} = 0.2$, and (c) $R_{ac} = 0.4$.

TABLE 4: Ground motions.

Earthquake	Year	Station	Magnitude	PGA_y (gal)
Tohoku	2011	FKS018	9.0	1069
Mammoth Lakes	1980	CSMIP 54214	6.2	700
Chi-Chi	1999	TCU136	7.6	700
El Centro	1940	USGS 0117	6.9	700
Kobe	1995	CUE	6.9	700

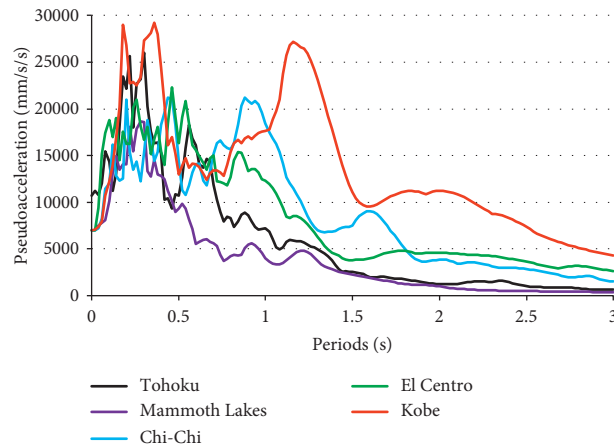


FIGURE 16: Pseudoacceleration response spectra.

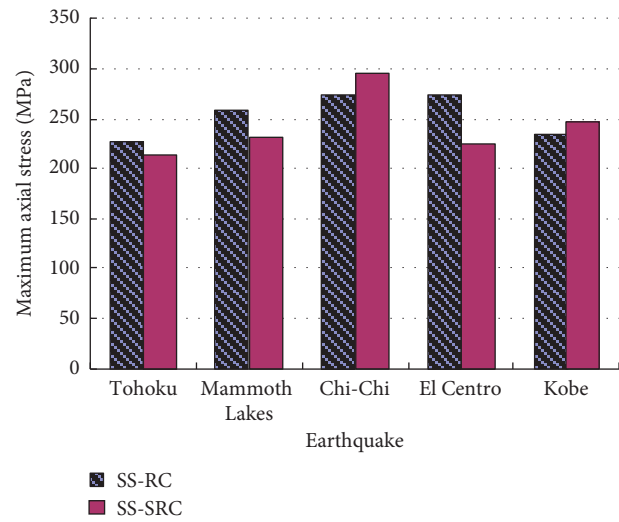


FIGURE 17: Maximum axial stresses of the latted shell members.

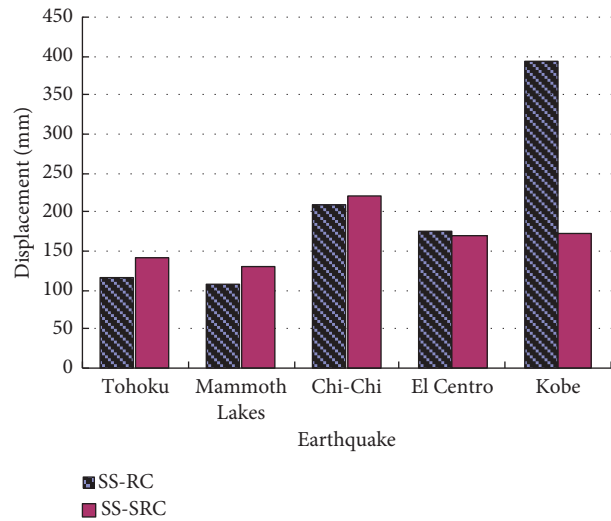


FIGURE 18: Maximum resultant displacements of the latted shells.

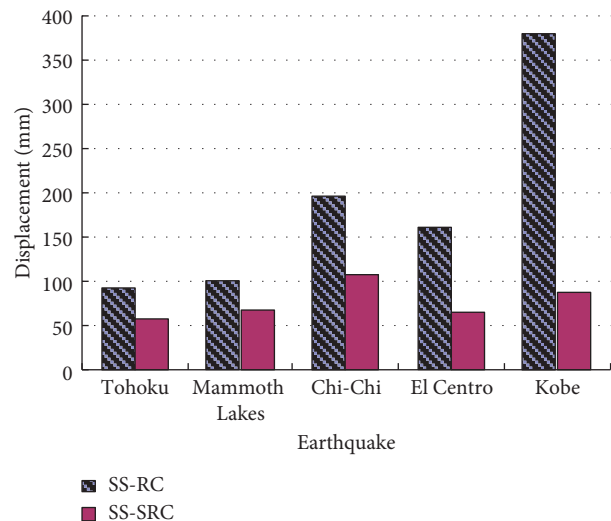


FIGURE 19: Maximum resultant lateral displacements of the RC column tops.

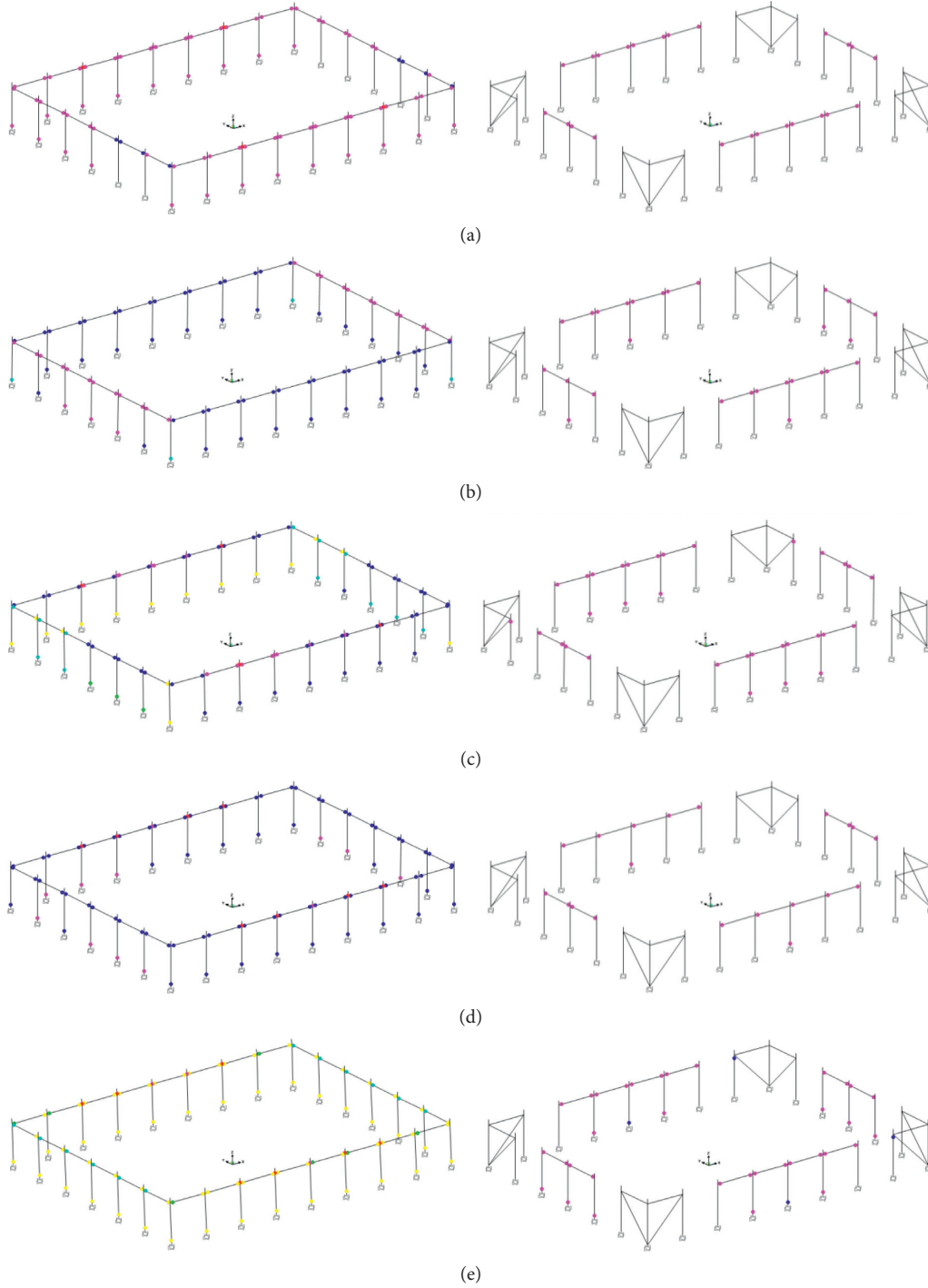


FIGURE 20: Plastic hinges under different earthquakes (left: SS-RC; right: SS-SRC). (a) Tohoku, (b) Mammoth Lakes, (c) Chi-Chi, (d) El Centro, and (e) Kobe.

vertical forces of roof, thus leading to the seismic responses differences including plastic hinges and lateral displacements of RC column tops. The most remarkable discrepancy in lateral displacements of RC column tops is in the case of Kobe's ground motion, because all the column bottoms exceed the ultimate capacities and large plastic rotations occur in the hinges of column bottoms, as is shown in Figure 20(e).

The time histories of maximum moments of RC column bottoms of section 600×400 mm are depicted in Figure 21. It is apparent that the column bottom moments in SS-RC structures are significantly larger than those of SS-SRC structures, which also explains the reason for the discrepancies in plastic hinges shown in Figure 20.

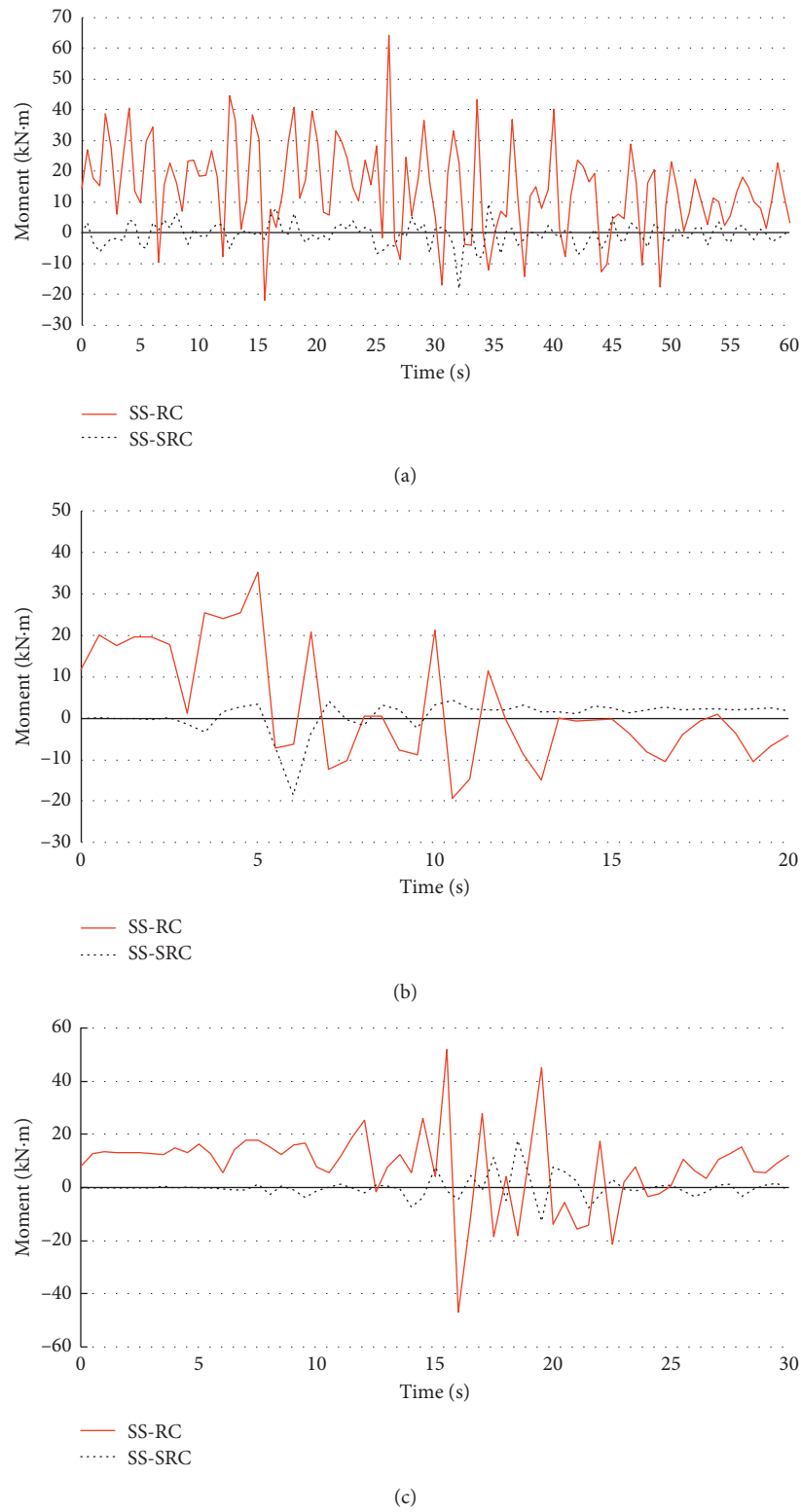


FIGURE 21: Continued.

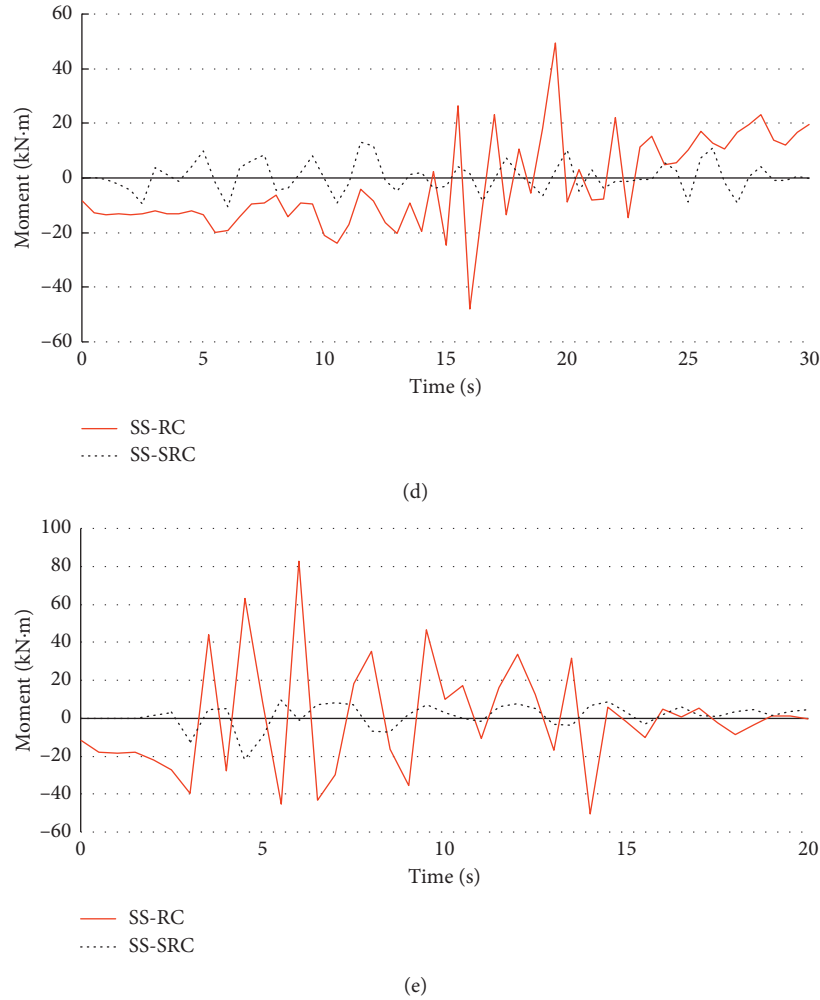


FIGURE 21: Time histories of maximum moments of the RC column bottoms. (a) Tohoku, (b) Mammoth Lakes, (c) Chi-Chi, (d) El Centro, and (e) Kobe.

4. Conclusions

Seismic damage of spatial structures of rectangular plan with RC substructures is observed in several earthquakes, especially in the RC substructures. In order to reduce the seismic damage potential of this kind of structure, a new structural configuration of spatial structures of rectangular plan is proposed, the substructures of which are composed of two parts: the steel substructure and the RC substructure. The former bears the horizontal and vertical forces of roof under earthquake and vertical loads, while the latter only bears the vertical load of roof by the arrangement of horizontal sliding bearings between the roof and the RC substructure. Therefore, the horizontal seismic forces of the roof can only be transferred to the steel substructure rather than the RC substructure by this kind of configuration, so the shear force and the bending moment of the RC substructure can be significantly reduced.

The static pushover analyses are performed on two kinds of simple structures with similar lateral stiffness: one is a steel braced frame with high-strength cable as braces, and the other is RC frame structures. The results show that the

lateral capacity of the steel structure is much larger than those of the RC structures with different reinforcements under several vertical loads.

A spatial structure of rectangular plan with typical dimension is designed according to Chinese structural designing codes. The structure is composed of three parts: the single-layer latticed shell as roof, the boundary beam structure, and the substructures. Two kinds of substructures are considered: one is RC structure, and the other is steel structure and RC structure. Seismic time history analyses are carried out for the spatial structure with two different substructures under five ground motions. The results show that the damage mainly concentrates on the substructures, and the seismic performance of the structure with steel and RC substructures is much better than that of the structure with RC substructures.

Data Availability

The authors declare that all data supporting the findings of this study are available within the article.

Conflicts of Interest

The authors declare that they have no conflicts of interest in connection with the work submitted.

Acknowledgments

This work was supported by the National Natural Science Foundation of China (no. 51308326), Shandong Provincial Natural Science Foundation (no. ZR2019MEE042), and Key Laboratory of Building Structural Retrofitting and Underground Space Engineering (Shandong Jianzhu University), Ministry of Education.

References

- [1] Z.-W. Yu, X.-D. Zhi, F. Fan, and C. Lu, "Effect of substructures upon failure behavior of steel reticulated domes subjected to the severe earthquake," *Thin-Walled Structures*, vol. 49, no. 9, pp. 1160–1170, 2011.
- [2] Y. G. Li, F. Fan, and H. P. Hong, "Effect of support flexibility on seismic responses of a reticulated dome under spatially correlated and coherent excitations," *Thin-Walled Structures*, vol. 82, pp. 343–351, 2014.
- [3] Z. Yu, S. Li, D. Lu, C. Lu, and J. Liu, "Failure mechanism of single-layer steel reticular domes with reinforced concrete substructure subjected to severe earthquakes," *International Journal of Steel Structures*, vol. 16, no. 4, pp. 1083–1094, 2016.
- [4] K. Kawaguchi, "A report on large roof structures damaged by the great Hanshin-Awaji earthquake," *International Journal of Space Structures*, vol. 12, no. 3-4, pp. 137–147, 1997.
- [5] T. Saka and Y. Taniguchi, "Damage to spatial structures by the 1995 hyogoken-nanbu earthquake in Japan," *International Journal of Space Structures*, vol. 12, no. 3-4, pp. 125–133, 1997.
- [6] M. Motosaka and K. Mitsuiji, "Building damage during the 2011 off the pacific coast of Tohoku earthquake," *Soils and Foundations*, vol. 52, no. 5, pp. 929–944, 2012.
- [7] J. Dai, Z. Qu, C. Zhang, and X. Weng, "Preliminary investigation of seismic damage to two steel space structures during the 2013 Lushan earthquake," *Earthquake Engineering and Engineering Vibration*, vol. 12, no. 3, pp. 497–500, 2013.
- [8] G. Nie, C. Zhang, J. Dai, and K. Liu, "Seismic damage investigation and seismic performance study of space double-layered lattice structure," *Journal of Performance of Constructed Facilities*, vol. 32, no. 2, Article ID 04018003, 2018.
- [9] Architectural Institute of Japan, "Joint editorial committee for the report on the great East Japan earthquake disaster, report on the great east japan earthquake disaster," Architectural Institute of Japan, Tokyo, Japan, 2014.
- [10] D. Yang, C. Yun, J. Wu, and Y. Zhang, "Aseismic performance of large span latticed domes with separated substructures," *Journal of Vibration and Shock*, vol. 37, no. 3, pp. 237–242, 2018.
- [11] China Architecture & Building Press, *GB 50010–2010, Code for Design of Concrete Structures*, China Architecture & Building Press, Beijing, China, 2011.
- [12] China Architecture & Building Press, *GB 50011–2010, Code for Seismic Design of Buildings*, China Architecture & Building Press, Beijing, China, 2016.
- [13] X. Liang, *GB 50017–2003, Code for Design of Steel Structures*, China Architecture & Building Press, Beijing, China, 2003.
- [14] China Architecture & Building Press, *Chinese Standard.net, JGJ 7-2010, Technical Specification for Space Frame Structures*, China Architecture & Building Press, Beijing, China, 2010.
- [15] H. X. Shang, "Performance testing research of high strength steel wire products," *Metal Products*, vol. 39, no. 6, pp. 39–43, 2013.
- [16] China Architecture & Building Press, *JGJ 257-2012, Technical Specification for Cable Structures*, China Architecture & Building Press, Beijing, China, 2012.
- [17] ASCE 41-13, *Seismic Evaluation and Retrofit of Existing Buildings*, American Society of Civil Engineers, Reston, VA, USA, 2014.
- [18] C.-H. Zhai and L.-L. Xie, "A new approach of selecting real input ground motions for seismic design: the most unfavourable real seismic design ground motions," *Earthquake Engineering & Structural Dynamics*, vol. 36, no. 8, pp. 1009–1027, 2007.

Research Article

Optimal Location of Multiple Tuned Mass Dampers in Regular and Irregular Tall Steel Buildings Plan

Mohsen Khazaei , Reza Vahdani, and Ali Kheyroddin

Department of Civil Engineering, Semnan University, Semnan, Iran

Correspondence should be addressed to Mohsen Khazaei; m.khazaei@qiet.ac.ir

Received 28 January 2020; Revised 26 June 2020; Accepted 13 July 2020; Published 16 September 2020

Academic Editor: Edén Bojórquez

Copyright © 2020 Mohsen Khazaei et al. This is an open access article distributed under the Creative Commons Attribution License, which permits unrestricted use, distribution, and reproduction in any medium, provided the original work is properly cited.

Tuned mass dampers are one of the most common devices for the passive control of structures subjected to earthquakes. The structure of these dampers consists of three main parameters: mass, damping, and stiffness. Tuned mass dampers reduce the amplitude of the responses affecting on a mode. In most cases, only a single TMD (tuned mass damper) or a few dampers at several points above the building height are installed on the roof of the building, requiring considerable mass and space in some parts of the structure as overhead. It is also more important to predict the elements that will meet the required mass. In this research, the performance of multiple tuned mass dampers (MTMDs) is investigated in L- and U-shaped regular and irregular tall steel buildings with 10 and 20 floors, under the near- and far-field records. Nonlinear time history analysis is also applied to evaluate the multiple tuned mass dampers effects on the seismic responses of the structures. The SAP2000 API and MATLAB genetic algorithm are used to determine the optimal location of the MTMDs in the roof plans of the buildings. The results show the effects of multiple tuned mass dampers in reducing the seismic response of acceleration, displacement, and base shear up to 50, 40, and 40% in average, respectively. The results of determining the optimum location of MTMDs in the models indicate the importance of the symmetry of the dampers relative to the centre of mass of the building.

1. Introduction

During an earthquake event, a significant amount of energy is applied to the structure. If this energy is not absorbed or dissipated, it causes destruction that will result in significant financial and life damage. In conventional methods, the building exhibits resistance by combining stiffness, ductility, and energy dissipation as well as inertia against dynamic forces (e.g., wind, earthquake, vibration of machines, sea waves, etc.). The damping value in these structures is very low and therefore the damped energy is negligible in the elastic behavior range of the structure. These structures experience a great deal of displacement under the influence of strong dynamic forces such as earthquakes crossing the elastic range. Inelastic displacements cause the plastic joints to be positioned locally in some parts of the structure, which in turn increases the ductility, and consequently a large amount of earthquake energy is dissipated by local

degradation in the lateral resisting system. In recent years, many efforts have been made to apply modern control devices to the structures exposed to earthquakes. These devices prevent the degradation of the structural elements during earthquake by absorbing some of the energy input into the structures [1]. Different vibration control methods include passive, semi-active, active, and hybrid, and various factors such as efficiency, weight, device and implementation cost, maintenance, and safety influence the choice of a specific type of vibration control device.

Tuned mass dampers (TMDs) are a type of passive damping systems that attaches to the main structure as a secondary mass and reduces the dynamic response of the structure through damping and stiffness, which is widely used in control engineering systems and other civil engineering structures [2, 3]. The mass dampers have a mass of about 1 to 5% of the total mass of the structure, which is connected by a spring and dampers to the location of the

structure which usually has the most displacement. Mass dampers are usually tuned by the frequency of the main mode of the structure. When this mode is stimulated, the mass damper absorbs and dissipates the energy of the earthquake by anti-phase movement toward structure. Ease of installation and implementation is one of its benefits. Multiple tuned mass dampers (MTMDs) consist of several single mass dampers that can be designed and installed in parallel or series in structures. They can be used in centralized or distributed structures. This research includes the related literature review to the topic, the governing equations of multiple distributed mass dampers, introduction of structural models used in the research, introduction of records used in analysis, model and software verification, the result evaluation of the 10- and 20-story buildings with MTMDs in ninth and tenth stories, and the optimal location of the mass dampers in the model plans using genetic algorithm (GA).

2. Literature Review

In a TMD system, a specific mass is mounted at a specified location of the structure and the vibration amplitude of the structure in the first mode is controlled by a spring and a damper with specified damping and stiffness coefficients. However, when external stimulation is such that the higher modes' contribution in the response of the structure is greater than the first mode, the TMD system may have the opposite effect and increase the amplitude of vibrations. The basic idea of TMD was first proposed by Frahm [4] in 1909 and then studied by Ormondroyd and Den Hartog [5] in 1956. For seismic applications, some researchers like Chen and Clark [6, 7] have shown that the individual TMD system is not effective in reducing seismic responses. There are two reasons for this: first, earthquake loads are a kind of shock and quickly reach maximum values. Secondly, earthquake shocks comprise a wide range of frequency components and often contain distinct vibrations in both the basic mode and the higher modes of tall building structures. The single-mass dampers are tuned for basic frequencies and are not capable of controlling higher vibrational modes. Reports have suggested that single mass dampers can enhance higher modal responses due to the coupling between basic and higher modes. Due to the disadvantages of using single mass dampers, many researchers have proposed the MTMDs system, multiple tuned mass dampers, which tune and direct different modes and are located in the different locations of the structures. McNamara [8] in 1977 investigated the effect of TMD vibration filtration under white noise and the application of this method under vibration induced by wind in building. Work on TMD was extended by Warburton and Ayorinde [9] in 1980 to determine the optimum values of TMD parameters attached to elastic structures, rectangular plates, and cylindrical shells subjected to periodic loads. Warburton calculated the optimal damper properties for a series of stimuli and response parameters. In 1994, Villaverde and Koyama [10] tested three different structures equipped with TMD, including a 2-dimensional 10-story shear frame, a 3-story frame, and a three-dimensional bridge

under 9 different earthquake types. Wirsching and Campbell [11] in 1974 solved the problem of optimizing the TMD parameters and the natural frequency and damping ratio attached to the multi-story structure and analyzed the response of the first main mode of the main structure equipped with a TMD under the Earth lateral vibration of Gaussian white noise. Abé and Igusa [12] and Jangid [13] investigated the effect of multiple tuned mass dampers according to the structural model of Figure 1 on the main structure. Using asymptotic analysis for the apparent resistance of attached devices, they concluded that several dampers with natural frequencies close to each other which cover a wide frequency range can be represented by an equivalent damping proportional to the dampers' mass.

Li [14] in 2002 investigated the impact of the broadband vibrations of the Earth on different types of linear MTMDs designs and utilized dynamic displacement magnification factor as well as dynamic acceleration magnification factor as the optimal design criterion and then they were compared with 5 MTMDs models with different combinations of stiffness, mass, damping coefficient, and damping ratio. In 1995, Kareem and Kline [15] investigated the method of control using MTMDs attached to a real-scale vibrating structure. They validated previous results and studies and showed that the efficiency of MTMDs in the natural frequency range is more dependent on the number of mass dampers than the damping ratio parameter. Abdullah et al. [16] investigated the adjacent structures using STMD or shared tuned mass damper system to reduce the vibration of structures and the effects of pounding. Due to the connection of STMD to both structures, the problem of tuning the stiffness and damping will be solved. Their results show that the STMD system performs better than TMD and is an effective way to reduce the impact of pounding on adjacent buildings and vibrations. Zahrai and Ghannadi [17] investigated the effect of tuned mass dampers on the control of earthquake-prone buildings by studying the effect of TMD vibration control on 5-, 8-, 10-, and 15-story special bending frame buildings in both directions. Tuan and Shang [18] investigated the effects of TMD on the dynamic response of the Taipei 101 tower, explaining that the tower is subjected to wind load and earthquake excitation. The simulated results were compared with the wind tunnel test and the desired records. The results showed the damper effect in reducing the vibration of the wind, although it did not have much effect in reducing the vibration of the earthquake force. Hirde and Aher [19] investigated the seismic response of a concrete building with irregular plan under earthquake force with pushover analysis. Models were analyzed with irregular and L-shaped plan and compared with irregular plan with 5, 10, and 15 floors. Soto and Adeli [20] used eight different sets of equations to tune the parameters of a mass damper attached to a 5-story building with irregular plan and height and exposed a 15-story and 20-story building with irregular planes to earthquake loading. Also, bi-directional mass dampers with pendulum mass dampers with 3 different plan and height irregularities from 5 to 20 stories and period from 0.55 to 4.25 seconds were exposed to Loma Prieta earthquake and their performances were compared. They also

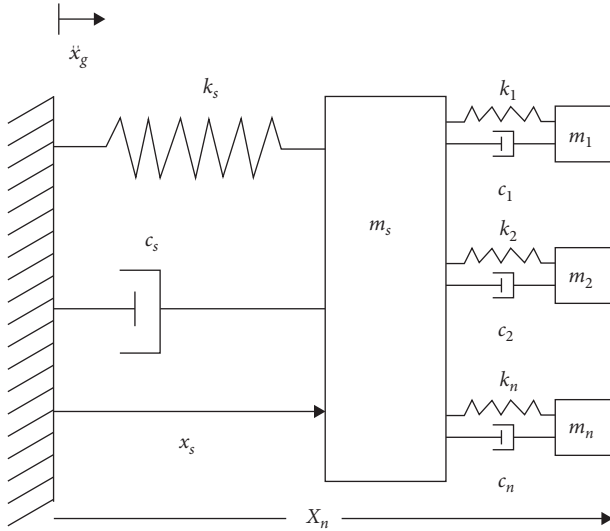


FIGURE 1: Structural model of MTMDs [13].

investigated the vibration control of irregular high-rise buildings using mass dampers and bi-directional mass dampers. Wakchaure et al. [21] examined various irregularities with analytical methods during earthquakes. Valmundson and Nau [22] investigated the range of mass, strength, and stiffness for regular buildings by UBC regulations. Selected structures are two-dimensional with 5, 10, and 20 floors, and irregularity is created by changes in the properties of the floors. Reddy et al. [23] concluded that mass dampers with mass percentages of 5 are more effective and the dimensions of the dampers should be proportional to the frequency of the structure. Bagheri and Rahmani-Dabbagh [24] used a viscous damper with mass damper to control the vibration of structures and concluded that the mass dampers significantly reduced the structural response and suggested an optimum mass damper (combined mass and viscous dampers) without the need for viscous damper with appropriate performance to be used. Wang et al. [25] applied mass dampers to control the bridge deck eddy vibrations and found that the mass dampers perform well in reducing bridge deck oscillation response. Li and Peng [26] proposed a new frequency-hopping-based design method for nonlinear mass damper, based on which the mass damper performs better than the linear design method. Lu et al. [27] investigated 5- and 20-story models as nonlinear benchmark structures for comparing optimum mass dampers and particle dampers. Their results showed that particle dampers offer better control effects than mass dampers in the responses such as maximum rotation of the plastic joints, energy absorption, and relative displacement between the main structure and the dampers. Lin [28] invented a type of mass dampers called TSMD that is formulated using three-degree-of-freedom modal properties of triple vibrational modes in a building with a two-way asymmetric plan whose performance has been validated by the frequency response function and seismic responses of a single-story and 20-storey structure with asymmetric plan. Lu et al. [29] pointed out that in recent years a great deal of

attention has been paid to the particle damper, which is very similar to mass dampers, although they have different damping mechanism. The results showed that vibration control with particle dampers has partially better performance than mass dampers on linear and nonlinear indices such as maximum rotation of plastic joints, energy absorption, and similar items. Kamgar et al. [30] investigated the optimum design of mass dampers considering the effects of soil-structure interaction and high-rise structures. For this purpose, a 40-story shear frame was selected and WOA (Whale Optimization Algorithm) algorithm was applied to optimize TMD parameters. Their results indicate that the soil type and selected function influence the optimal design of the mass damper system. Elias et al. [31] compared the performance of a distributed multiple mass vibration absorber on a nonlinear structure with a single vibration absorber. The results showed that the mass damper distribution would have favorable effects on structures exposed to earthquake excitation. Rahmani and Könke [32] investigated the optimal location and parameters of mass dampers in high-rise buildings using genetic algorithms. They used multiple mass dampers distributed at building height and found that, at higher modes, distributed dampers at building height are more effective than mass dampers, and the optimal position of the dampers is highly dependent on the frequency of earthquake excitation. Yucel et al. [33] developed an ANN (artificial neural network) model to estimate the TMD parameters and the long numerical repetition process used in optimization. The aim of the research is to develop a method for mechanical systems including structures exposed to seismic loads. Keshtegar and Etedali [34] suggested a method based on the dynamic parameters of the structure for the optimal design of mass dampers, which output more accurately than other algorithms. Nigdeli and Bekdaş [35] in their research examined several dampers on the structural floors. They concluded that the application of the damper at several points in the structure has a more favorable effect than the placement of a damper on the roof of a building. Shahi et al. [36] examined the effects of soil/structure interaction on the seismic behavior of structures and their performance. Etedali et al. [37] investigated the performance of TMD and FTMD in seismic control of tall buildings under near-field earthquakes, including soil and structural interactions. In their study, they used a 40-story structure and concluded that the FTMD performed better than the TMD in terms of story placement, drift, and acceleration parameters. Now, considering the research history of researchers on mass dampers and their focus on the use of single dampers on the roof or the distribution of dampers on building floors, this study investigates the optimum location of multiple distributed dampers in the roof plan especially in buildings with plan irregularities, and changes in seismic parameters have been investigated by changing the damper position in the roof plan.

3. Governing Equations of TMD

To determine the MTMDs parameters, Sadek et al.'s [38] (according to equations (1)–(4)) method which is provided

for multi-degree-of-freedom structures is utilized as an initial value and sample:

$$f = \frac{1}{1 + \mu\phi} \left[1 - \beta \sqrt{\frac{\mu\phi}{1 + \mu\phi}} \right], \quad (1)$$

$$\xi = \phi \left[\frac{\beta}{1 + \mu} + \sqrt{\frac{\mu}{1 + \mu}} \right], \quad (2)$$

$$M_n = \frac{(\sum_1^n m_i \phi_{i,n})^2}{\sum_1^n m_i \phi_{i,n}^2}, \quad (3)$$

$$\begin{aligned} m_{\text{TMD}} &= \mu \cdot M_n, \\ K_{\text{TMD}} &= \omega_0^2 f^2 m_{\text{TMD}}, \\ C_{\text{TMD}} &= 2\xi \omega_0 f m_{\text{TMD}}, \end{aligned} \quad (4)$$

where f is optimal frequency, which is the ratio of the damper frequency to the structure frequency, ξ is the optimum damping ratio, μ is the mass ratio which is the ratio of damper mass to the structural mass, β is the damping ratio of the structure, ϕ is the mode shape at the location of the TMD such that the coefficient of the modal contribution is equal to the unit, M_n is the effective mass of the first mode or any mode that the damper is set to control, and m_{TMD} , K_{TMD} , C_{TMD} are the mass, stiffness, and the damping of the TMD, respectively.

4. Structural Models

4.1. Assumptions and Loading. The mechanical properties of ST37 steel are as follows (Table 1).

All the structures have been modelled as 3D models and analyzed with nonlinear dynamic analysis. The sample structures are considered to be steel structures with special ductility. The dead and live loads of the floors are 500 kgf/m² and 200 kgf/m², respectively, floors' height is 3.2 meters, and the structure is made from 5 bays with 6-meter length and regular plan. According to Soto and Adeli [20] researches referred to in the literature review, the mass ratio of 3 percent for the design of dampers and the damping ratio of 2% for structures are considered based on ASCE2010. The region with very high risk and the soil of Type III are assumed for building design. The elements' mass is ignored and the rigid diaphragm is applied to floors. The axial length change of beam elements is also ignored. The rigid-zone factor is assumed to be 0.5. The effective variables in seismic coefficient (e.g., $C = AB I/R_u$) are considered as in Table 2. The effective mass of the structures is comprised of the dead load plus 20% of the live load.

4.2. Structural Element Design. After spectral analysis, the structural elements are designed in SAP2000.v19.2 software. AISC360-10 regulation is used to design members and seismic criteria are applied to design members. The utilized sections are HEB for beams and BOX for columns.

5. Seismic Records Selection

To determine the impact of the control system, 7 records from 7 different near-field earthquakes and 7 far-field earthquakes have been selected. In order to investigate the effects of damper in different models, earthquake records have been applied in one direction to the structure of analytical models. The properties of the selected records are given in Tables 3 and 4. Different seismic records with different PGA and fault distance are selected to consider the impacts of different frequency contents of earthquakes.

5.1. Seismic Records Normalization. According to Code 2800, the accelerometer data used for structural analysis must be normalized. To normalize them, after scaling them to their maximum value (PGA), the accelerometer data response spectrum is provided for a 5% damping. Then, the obtained spectra of the accelerometer data are averaged and compared over the time intervals of 0.2 T and 1.5 T, so that according to the 2800 code the average spectrum should be 1.4 times larger than the standard code 2800 spectrum [39]. After the response spectrum of the earthquake records is obtained, their averages are compared with the 2800 standard spectrum and scaled as follows (Figure 2).

6. Multiple Tuned Mass Damper (MTMD) Properties

In this paper, according to Soto and Adeli [20] research, which is based on thorough investigation of various researcher expressions and design parameters of mass dampers, the optimum mass ratio of the damper is selected to be 3%. The mass damper frequency of the main structure is also considered to be 1.25. Due to the study of the application of dampers and their torsional effects on structural models, the mass of dampers has been applied to the models in two directions. The parameters related to the mass damper are calculated and presented for the regular and irregular 10-story model in Table 5.

7. Geometry and Placement of Dampers

The plan used in the models is a regular and irregular square with 5 bays with 5-meter openings for regular models. Irregular plans according to the definition of geometrical irregularities mentioned in the irregular plans based on the definition of plan geometrical irregularity in 4th edition 2800 code [39] have been developed and defined for analysis in SAP2000 software. The utilized mass dampers in the models are defined as in Figure 3.

In this research, dampers are used in three conditions: at first, at one point on the roof, second, at two points on the roof, and third, at four points on the roof. The placement of the dampers is given in Figures 4–6.

8. Verification

In this study, for the purpose of verification, the effects of multiple mass dampers on the seismic behavior of 3-story

TABLE 1: Mechanical properties of steel.

Expected ultimate (F_{ue}) stress	Expected yield (F_{ye}) stress	Poisson coefficient (ν)	Ultimate (F_u) stress	Yield stress (F_y)
4070 kg/cm ²	2640 kg/cm ²	0.3	3700 kg/cm ²	2400 kg/cm ²

TABLE 2: Seismic parameters of models.

Models	R_u	T	T.	T_s	K	B	C
Regular 10-story	7.5	1.07	0.15	0.7	1.42	1.632	0.076
Regular 20-story	7.5	2.26	0.15	0.7	1.88	1.134	0.053

structure have been investigated experimentally by Chen and Wu [40]. The studied structure in Chen et al.'s research with a 1/4 scale steel bending frame was examined at the seismic table of Rolla University. Structural dimensions are 48 inches long, 24 inches wide, and 100 inches high, and the structures are shown in Figure 7. OPENSEES software has been used to validate the experimental studies of multiple mass dampers in the paper. The reason for using is efficiency, fast analysis and processing, high accuracy, and open source nature of this software.

This structure is designed to test the control of a structure with a hydraulic actuator placed on the first roof. The model is restrained with steel braces in three floors and stimulated with a hydraulic Jack. Structural restraint with steel braces has no role in the structural behavior and is solely applied to evaluate the performance of the mass dampers. Each mass damper consists of a mass block, a set of continuous springs, and a sliding shaft ball bearing. The mass block attaches to the base wall of the damper via extension springs and can only move along the dual shafts. The natural frequency of the damper can be adjusted using different types of springs. Since no damping element has been added to the damper system intentionally, friction between the bearings and the shafts forms the main damping part of the system [40].

8.1. Model Structural Properties. The concentrated masses on the first, second, and roof are 445, 394, and 388 kg, respectively. Forced excitation experiments were performed to identify the structural parameters for all three modes. First, several sine sweep experiments were performed to identify approximately the natural frequencies of the structure. Then, a series of concurrent tests with different excitation frequencies were performed around the natural frequencies of the tested structure. The modal properties of the test are shown in Table 6.

8.2. Dampers Properties. Six different types of continuous springs were used consistently throughout the shake table tests. Three specimens were selected randomly and with determination of resilience constant. The properties of the dampers are given in Table 7.

The damper free vibration pattern for the first mode is shown in Figure 8.

8.3. Verification Results. The following results are obtained and compared with the values of the paper by studying the floor accelerations in the dampers with masses of 60 and

80 kg. It should be noted that this issue has been analyzed simultaneously in the OPENSEES and MATLAB programs. The comparison diagram of the controlled structure acceleration results with damper in software with the experimental model results is shown in Figure 9, which is confirmed by a slight difference. The response of the normalized accelerations (ℓ^2 norm) of the structure controlled by the mass dampers on the roof floor is presented in Figure 9. It can be seen in the figure that multiple mass dampers can reduce the normalized acceleration response of the stories by more than 20%.

9. Nonlinear Time History Analysis Results of the Regular 10-Story Model

Mass dampers reduce the applied force to the structures by structural mass increase approach and the change in the stiffness and mass matrices of the structures, which results in a change in the effective time period of the structure and getting the structure away from the acceleration sensitive boundary. When the dampers are in a position of the structures, the control of seismic response of the structures is not significant and has little effect on the response of the structures with higher predominant modes. Thus, when the damper is located at more than one point, it is possible to control the seismic response of the structures by controlling the impact of higher modes.

9.1. Roof Displacement Results with Dampers in the Tenth Story. To evaluate the effect of tuned mass dampers on the seismic response of regular and irregular structures in different damper position conditions, the maximum lateral displacement of the roof is extracted for near- and far-field records. In this study, dampers are mounted on the roof floor in three conditions: one, two, and four dampers. The records used in this study are 7 near-field and 7 far-field records. In this section, the displacement value for each record with damper and without damper conditions is plotted. Figure 10 shows the maximum roof displacement in the ten-story model.

According to the results of the maximum displacement investigated for the 10-story structure without mass dampers and with different conditions with different mass dampers, it can be seen that utilizing tuned mass dampers in near-field and far-field records significantly reduces the displacement of the 10-story structure. It is observed that the change in the number of dampers leads to a change in the responses. The highest displacement reduction for near-field records in the case of using a damper is 43%. This amount of reduced displacement is investigated toward the case of without damper. The highest amount of displacement reduction for the cases of two and four dampers is 49% and 52%, respectively. The results of the far-field records also show that,

TABLE 3: Near-field earthquake properties.

	Record	Station	Year	Dis (km)	Mag	PGA	PGV (cm/s)	T_s (sec)	Duration (sec)
1	Alaska-Denali	Pump	2002	2.74	7.9	0.32	1689	3.48	86
2	Bam	Bam	2003	1.7	6.6	0.59	417	0.78	37.36
3	Chi-Chi	Thy101	1999	9.94	7.62	0.44	261.38	0.9	26.48
4	Chi-Chi	Tcu 68	1999	0.32	7.62	0.56	312	0.42	12.48
5	Imperial-Valley	El Centro Array	1979	1.35	6.53	0.43	250.12	0.24	8.49
6	Kobe	Takatori	1995	1.47	6.9	0.61	206	1.22	11.34
7	Borujerd	Silakhor	1909	12	7.3	0.44	321	1.52	56.34

TABLE 4: Far-field earthquake properties.

	Record	Station	Year	Dis (km)	Mag	PGA	PGV (cm/s)	T_s (sec)	Duration (sec)
1	Chi- Chi	Chy 065	1999	83	7.62	0.6	130.79	0.62	28.515
2	Chi-Chi	Tap95	1999	109	7.62	0.15	178.062	0.98	15.8
3	Imperial-Valley	Oak-2	1979	18.87	5.01	0.24	148.23	0.32	12.515
4	Imperial-Valley	Outers	1979	24.23	6.53	0.26	38.78	0.16	1.75
5	Kobe	Hik	1995	95	6.9	0.14	110.64	0.6	17.04
6	Loma Prieta	Halls Valley	1989	30.25	6.93	0.23	107.85	0.3	10.78
7	Manjil	Qazvin	1990	49.97	7.37	0.13	83.79	0.16	25.71

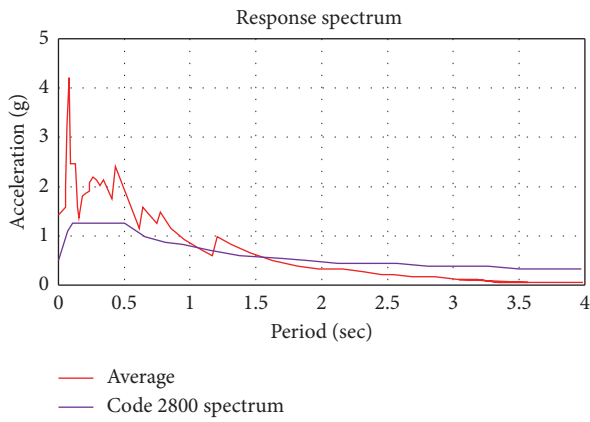


FIGURE 2: Comparison of response spectrum average of earthquake records with 2800 standard spectrum.

TABLE 5: Design parameters of mass damper in regular and irregular 10-story models.

Model	μ	m_d (kg)	k_d (ton/m)	C_c (ton/sec)	C_d (ton/sec)
Regular 10-story	0.03	22779	496.65	212.3	22.07
L-shaped 10-story	0.03	16297	311.93	142.59	14.83
U-shaped 10-story	0.03	17531	227.2	126.22	13.12

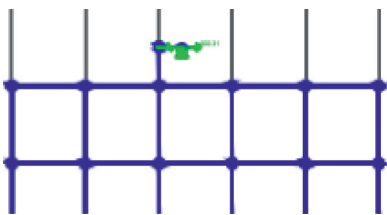


FIGURE 3: Mass application in the TMD model.

in the case of one damper, the reduced mean displacement compared to the cases of without damper, two dampers, and four dampers is 45%, 55%, and 60%, respectively, but on average using four dampers reduces displacement more than using two dampers. In a number of earthquake records, especially in near-field ones, due to the frequency content and earthquake parameters, using two dampers has better results than the four dampers.

9.2. Roof Acceleration Results with Dampers in the Tenth Story.

Tuned mass dampers have the greatest impact on the acceleration value of the structures and control the seismic response of the structures by getting the structures away from the acceleration sensitive region. The maximum acceleration of the roof in the ten-story model is shown in Figure 11.

Since the acceleration of the floors of a structure is influenced by the transmitted acceleration from the ground and the dynamic characteristics of the structure, therefore the mass of the structure increases with the use of mass dampers and the acceleration of the floors reduces with increasing the time period of the structure. This issue is investigated for the 10-story structure in the case of using mass dampers compared to without damper, which yields interesting results. The floor acceleration of the 10-story structure in a fixed mass is affected by the damper number and position. This issue is also investigated for near- and far-field records and the frequency content effects of near- and far-field earthquake records. It is observed that the maximum acceleration reduction for near-field records when using one, two, and four dampers is 28, 46, and 46%, respectively. The results also show 36%, 46%, and 44% reduction for far-field earthquakes, respectively. The results show the effect of the number of dampers on the acceleration reduction of the structure affected by the near- and far-field records. It is also observed that the change in the properties of the record causes a change in the seismic responses such

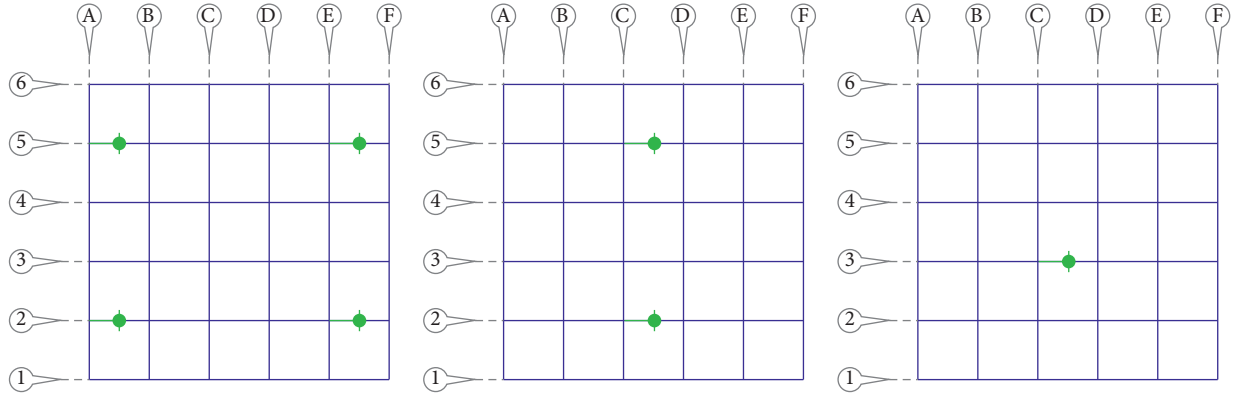


FIGURE 4: Damper at one point (right), dampers at two points (middle), and dampers at four points (left).

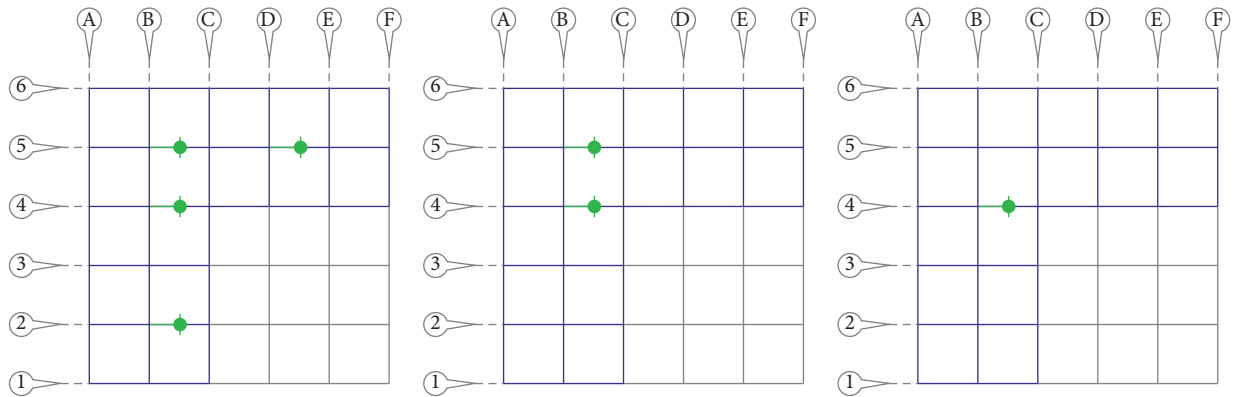


FIGURE 5: Damper at one point (right), dampers at two points (middle), and dampers at four points (left).

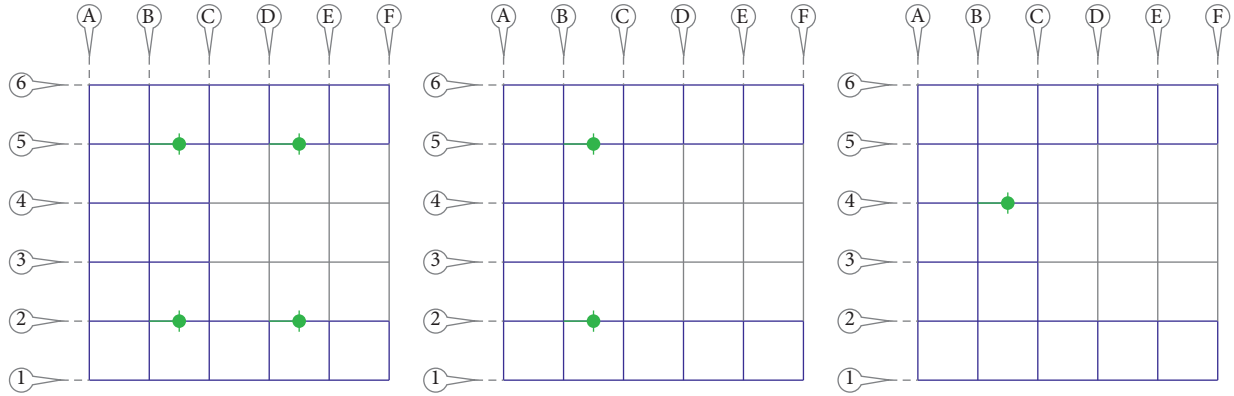


FIGURE 6: Damper at one point (right), dampers at two points (middle), and dampers at four points (left).

that the near-field records increase the acceleration values in the cases of using 1, 2, and 4 dampers over the far-field records due to the pulse in the velocity frequency content.

9.3. Base Shear Results with Dampers in the Tenth Story. The base shear value reduces at a constant mass by changing the applied acceleration to the structure. In this section, the maximum base shear obtained from the time history analysis is presented for the near- and far-field records. The effects of

the tuned mass dampers on the reflection of the earthquake force to the structures are evaluated considering the base shear, and the force dissipation is determined in different conditions considered for the multiple mass dampers. The maximum base shear in the ten-story model is given in Figure 12.

The base shear of the structures is important because any changing in the applied acceleration to the structures changes the amount of base shear. The acceleration value of the 10-story structure is investigated under the near- and far-

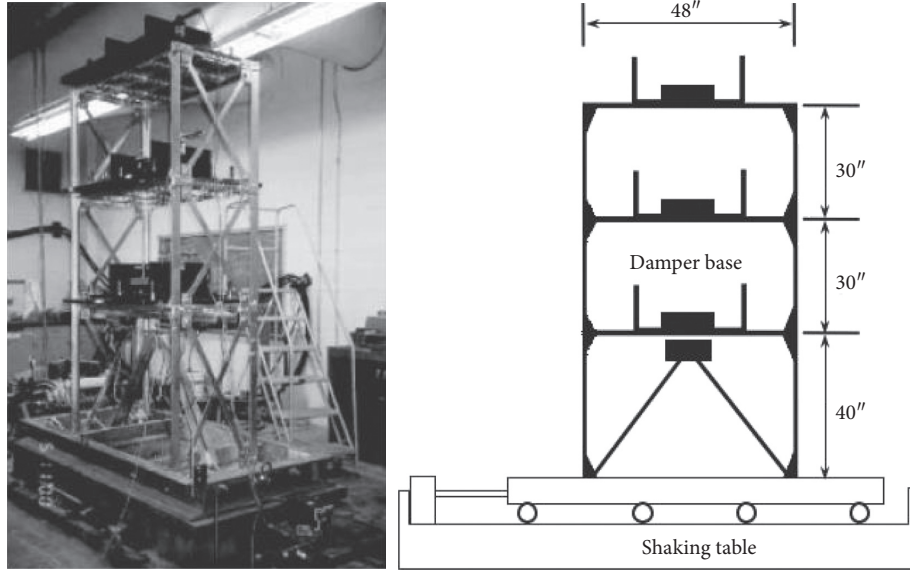


FIGURE 7: Studied structure on the shaking table [40].

TABLE 6: Modal properties of structure [40].

Mode no., i	1	2	3
Frequency, f_i (Hz)	2.743	9.45	18.84
Normalized mode shape, Φ_i	$\begin{Bmatrix} 0.0186 \\ 0.0299 \\ 0.0356 \end{Bmatrix}$	$\begin{Bmatrix} 0.0352 \\ 0.0123 \\ -0.0316 \end{Bmatrix}$	$\begin{Bmatrix} -0.0268 \\ 0.0385 \\ -0.0158 \end{Bmatrix}$
Damping ratio, ε_i (%)	0.48	1.15	1.45
Participation factor, γ_i	33.904	8.293	-2.863
Orthogonality with respect to mass matrix, $\Phi^T M_S \Phi$		$\begin{bmatrix} 1.0 & 0.001 & 0.013 \\ 0.001 & 1.0 & -0.039 \\ 0.013 & -0.039 & 1.0 \end{bmatrix}$	

TABLE 7: Utilized damper properties in the model [40].

Mass, M_s (kg)	Damping, C_s ($\times 10^2$ N · sec/m)	Stiffness, K_s ($\times 10^6$ N/m)
$\begin{bmatrix} 445 & 0 & 0 \\ 0 & 394 & 0 \\ 0 & 0 & 388 \end{bmatrix}$	$\begin{bmatrix} 7.770 & -4.683 & 0.257 \\ -4.683 & 8.594 & -4.224 \\ 0.257 & -4.224 & 4.057 \end{bmatrix}$	$\begin{bmatrix} 2.669 & -2.118 & 0.452 \\ -2.118 & 3.397 & -1.645 \\ 0.452 & -1.645 & 1.260 \end{bmatrix}$

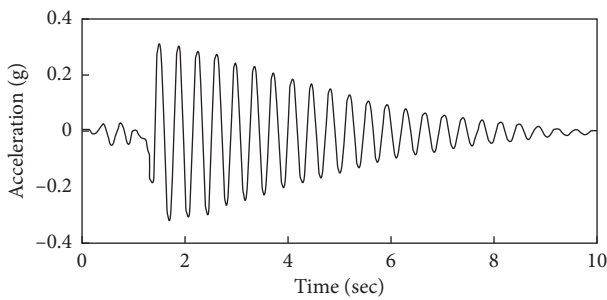


FIGURE 8: First mode stimulation pattern [40].

field records in the cases of with damper and without damper. The results show that, in the case of using tuned mass damper, the reduction value of applied acceleration to the structures is proportional to the reduction value of

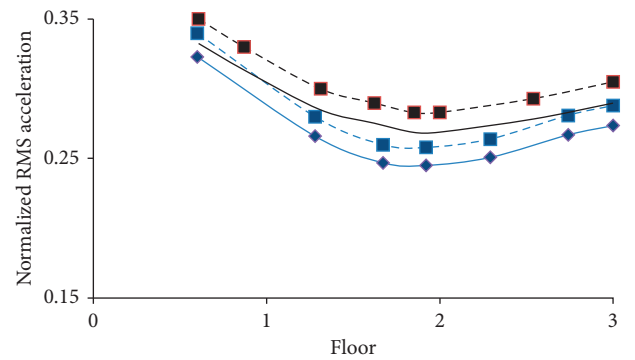


FIGURE 9: Comparison diagram of controlled structure acceleration results with damper in software analysis with obtained results of the experimental model.

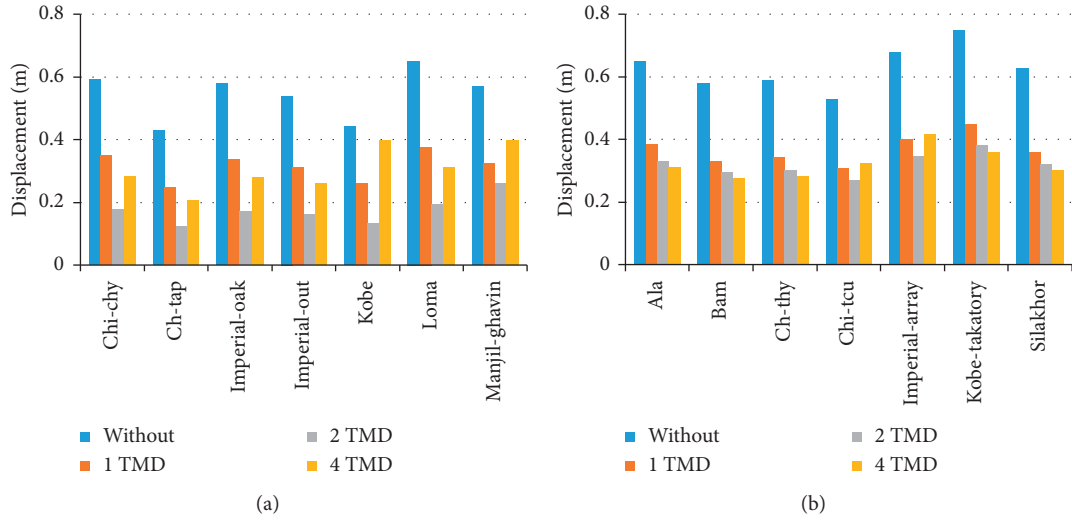


FIGURE 10: Maximum roof displacement under the near-field (right) and far-field (left) earthquakes in the regular 10-story model.

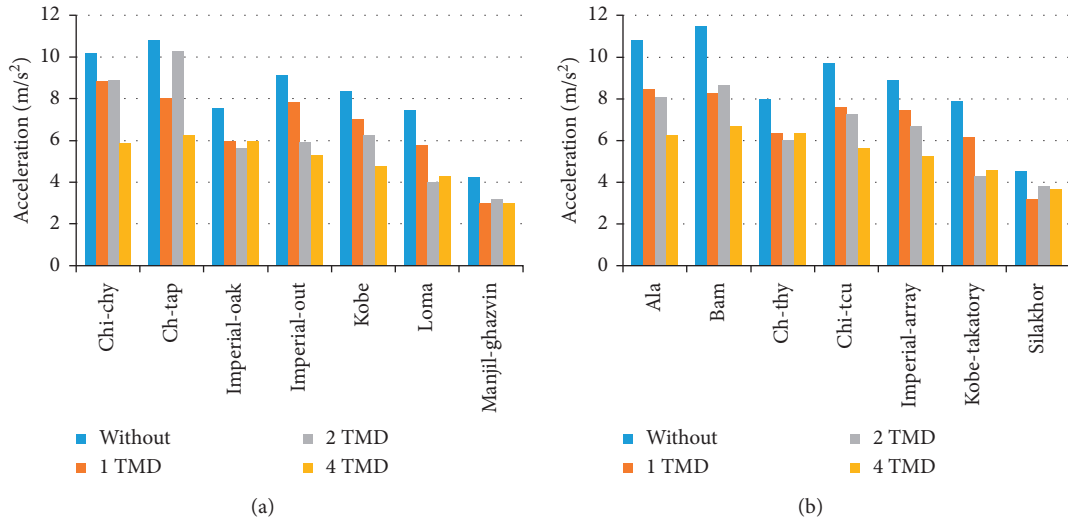


FIGURE 11: Maximum roof acceleration under the near-field (right) and far-field (left) earthquakes in the regular 10-story model.

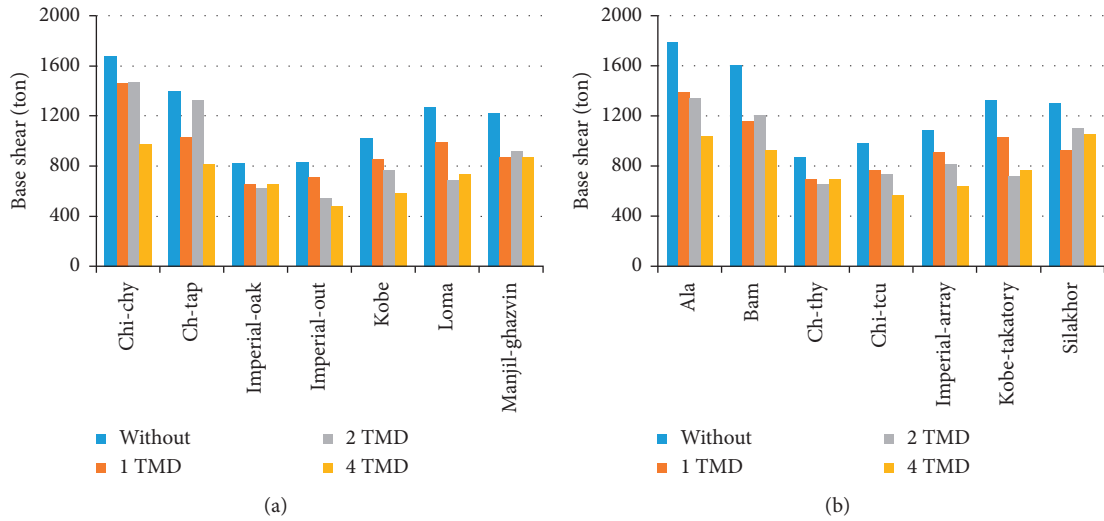


FIGURE 12: Base shear under the near-field (right) and far-field (left) earthquakes in the regular 10-story model.

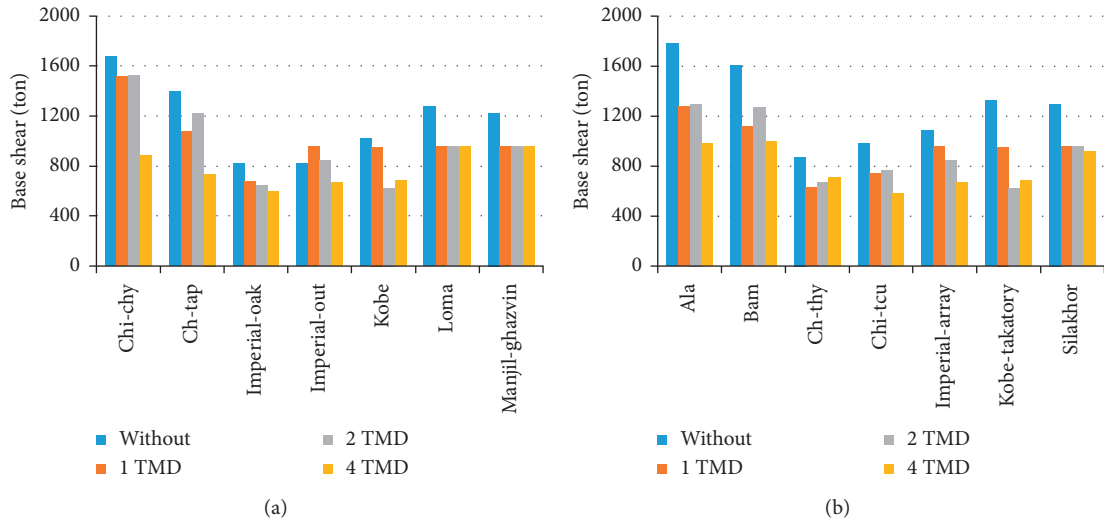


FIGURE 13: Base shear with damper in the ninth story under the near-field (right) and far-field (left) earthquakes in the regular 10-story model.

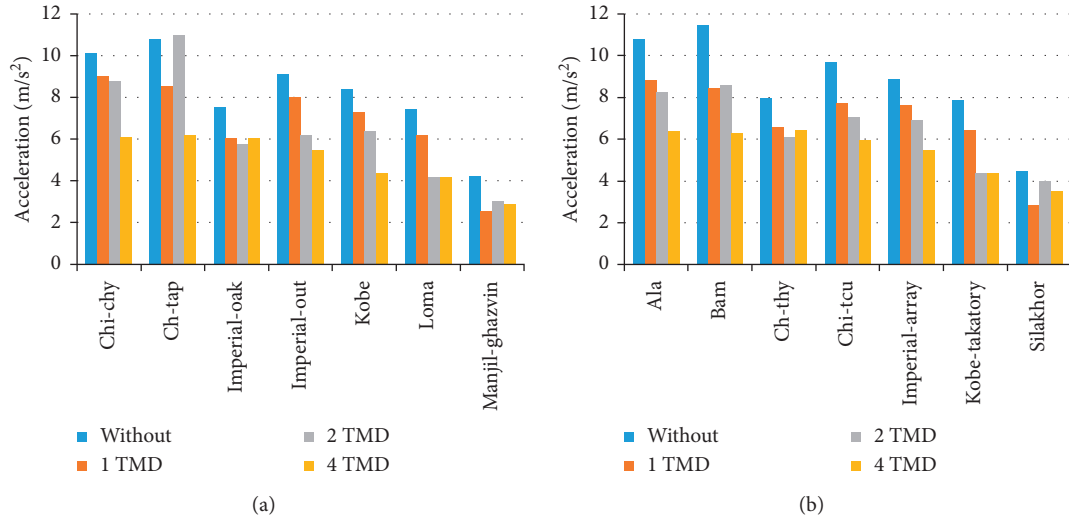


FIGURE 14: Acceleration with damper in the ninth story under the near-field (right) and far-field (left) earthquakes in the regular 10-story model.

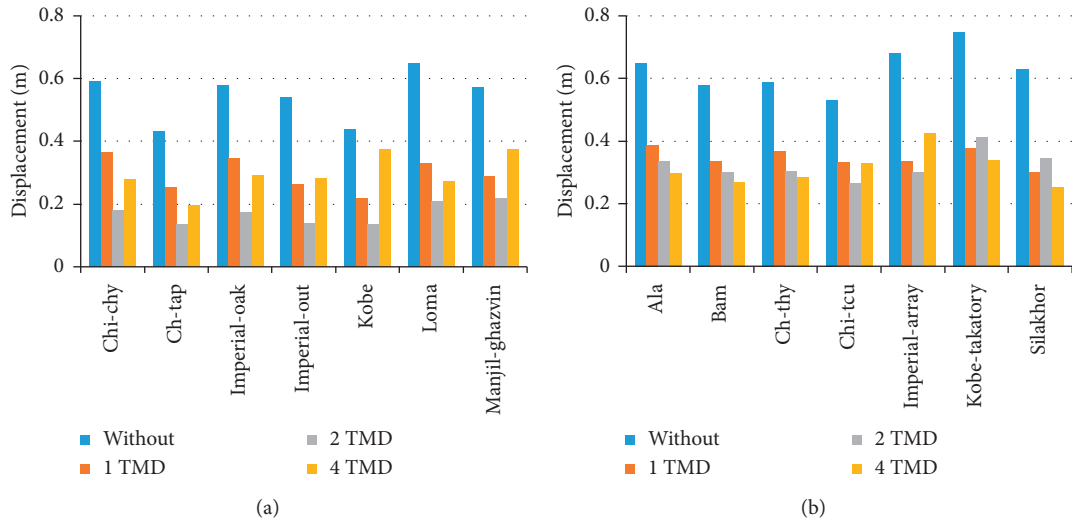


FIGURE 15: Displacement with damper in the ninth story under the near-field (right) and far-field (left) earthquakes in the regular 10-story model.

structural base shear. This reduction is different for different dampers. In the case of using one damper, the maximum reduction for near- and far-field records is 40% and 36%, respectively. The results for using two and four dampers in near- and far-field records are 46%, 42%, 46%, and 44%, respectively.

9.4. Base Shear Results with Dampers in the Ninth Story. In this section, the maximum base shear obtained from the time history analysis for near- and far-field records is presented. The maximum base shear in the ninth floor of the ten-story model is shown in Figure 13.

The numerical results of the seven near- and far-field records for the case that the damper is placed on the ninth floor of the 10-story structure show that using tuned mass dampers on the penultimate floor of the structure also has a significant effect on reducing the base shear value. On the other hand, it can be seen that changing the number of dampers changes the base shear value, and in some cases, having more dampers leads to noticeable reduction in base shear. The numerical analysis of base shear for near-field records shows that, in the cases of using one, two, and four dampers, the maximum reduction is 30, 53, and 48%, respectively. For far-field records, these values are 24, 39, and 33%, respectively.

9.5. Acceleration Results with Dampers in the Ninth Story. In this section, the maximum acceleration obtained from the time history analysis for near- and far-field records is given. The maximum acceleration in the ninth floor of the ten-story model is given in Figure 14.

Studying the maximum acceleration of the roof for the case where the dampers are placed on the ninth floor of the 10-story structure indicates that utilizing tuned mass dampers on the penultimate floor can control the acceleration of the structure. It is observed that the change in damper position has a different effect on the acceleration values of the roof. The change in the number of dampers in the plan also causes a change in the maximum value of roof acceleration. Numerical analysis of the roof acceleration shows that the maximum acceleration reduction of the floor for the cases with one, two, and four dampers under the near-field records is 36, 44, and 45%, respectively. This value for far-field records is 39, 43, and 47%, respectively.

9.6. Roof Displacement Results with Dampers in the Ninth Story. In this section, the displacement obtained from the time history analysis for near- and far-field records is given. The maximum displacement in the ninth floor of the ten-story model is given in Figure 15.

By studying the maximum lateral displacement of the roof in the case the damper is located in the ninth-floor, it can be seen that the change in the number of the dampers in the ninth floor has a different effect on the lateral displacement reduction of the roof. The maximum reduction in the lateral displacement in the case of using TMDs with one, two, and four dampers for near-field records is 52, 55, and

59%, respectively, and these values for far-field records are 51, 74, and 58%, respectively. The placement of the dampers in the ninth floor rather than the tenth floor affects the dynamic properties of the structure and changing the frequency characteristics of the structure including the time period of the structures alters the effects of the dampers in the seismic response of the structure. In general, regarding the location of the mass dampers in the tenth and ninth floors of the regular ten-story model, it can be concluded that using the mass dampers has significant effects on the seismic responses of the structures up to 50% reduction in average in the roof acceleration, displacement, and the base shear. Using 2 or 4 dampers compared to one damper shows a significant reduction up to 25% in the seismic response of the structure. The response reduction variations in near-field records are more noticeable than those in the far-field, due to the frequency content and the details of earthquake parameters. The responses also show better adaptation of the mass dampers to analytical models with near-field records. The placement of the dampers in the tenth floor shows little difference in the seismic response compared to the ninth floor in the present analytical model. It is worth noting that the application of dampers is also investigated in the irregular structures and the maximum percentage reduction in the regular and irregular structures is shown in Tables 8–10.

The results of the tables show the significant impact of the mass dampers on the reduction of seismic parameters and responses. The percentage of reduction in the models with multiple mass dampers is more than single dampers. In the case of base shear response, increasing the number of dampers from one to four increases the percentage reduction in all models and the responses are mostly reduced in near-field records and the desirable capabilities of the dampers are noticeable in controlling the displacement and accelerations of the structures in near-field records. In the case of roof displacement, as the number of dampers increases, an increase in the percentage of response reduction is observed, and the response of roof displacement is further reduced in far-field records such that, in the special cases, using two dampers under far-field earthquake shows a reduction by approximately 80%. Increasing the number of dampers has also remarkable effect in the reduction of acceleration responses.

10. Number and Location Optimization of MTMDs

In the optimization section, the effect of 2 and 4 dampers on the last floor of the 10- and 20-story structures has been investigated. For this purpose, a genetic algorithm has been used to find the optimal position of these dampers, so that the position of the structural nodes in the roof level (with N number of variables equal to the number of dampers) is considered as a variable and the optimal combination of these variables has been obtained. The algorithm cost function is formed using the SAP2000 API software. For each chromosome in the population consisting of the following variables (for example, 5, 9, 12, and 32 for the

TABLE 8: Maximum displacement reduction percentage of roof in the regular and irregular 10-story models.

Roof displacement reduction % Record	1-damper		2-damper		4-damper	
	Near-field	Far-field	Near-field	Far-field	Near-field	Far-field
Regular 10-story	43	45	49	70	52	52
L-shaped 10-story	40.85	51.75	48.02	80.5	50.44	56.16
U-shaped 10-story	49.45	51.75	56.35	80.5	50.44	59.8

TABLE 9: Maximum acceleration reduction percentage in the regular and irregular 10-story models.

Roof acceleration reduction % Record	1-damper		2-damper		4-damper	
	Near-field	Far-field	Near-field	Near-field	Far-field	Near-field
Regular 10-story	28	36	46	46	46	44
L-shaped 10-story	27.72	32.04	40.02	45.54	45.54	43.56
U-shaped 10-story	29.96	38.52	49.22	49.22	49.22	47.08

TABLE 10: Maximum base shear reduction percentage in the regular and irregular 10-story models.

Base shear reduction % Record	1-damper		2-damper		4-damper	
	Near-field	Far-field	Near-field	Far-field	Near-field	Far-field
Regular 10-story	40	36	46	42	46	44
L-shaped 10-story	44.8	38.52	51.52	36.54	51.52	49.28
U-shaped 10-story	41.6	32.04	40.94	43.68	47.84	45.76

TABLE 11: Genetic algorithm parameters.

Mutation rate (%)	Selection rate (%)	Generation	Population	Algorithm type
20	70	15	30	Continuous

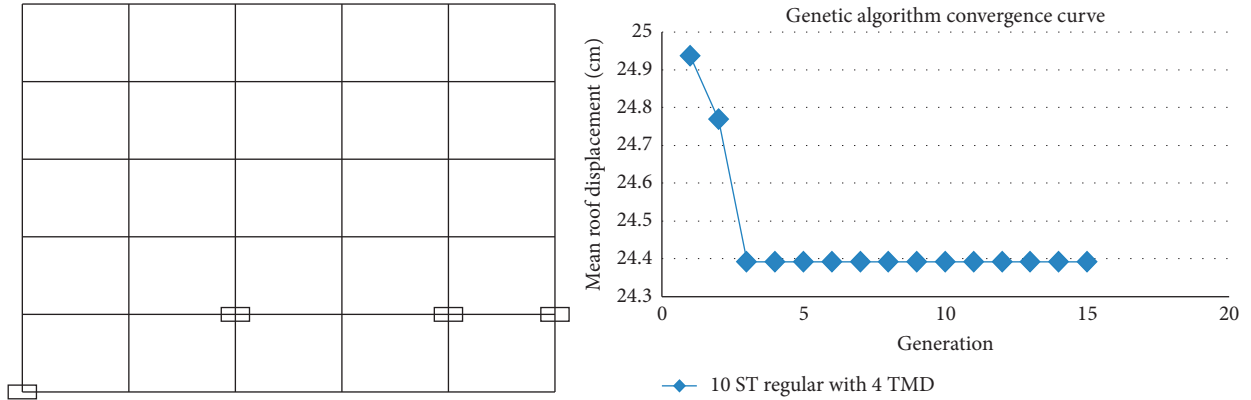


FIGURE 16: Convergence diagram of the ten-story model with 4 dampers in genetic algorithm (right) and damper optimal positions (left).

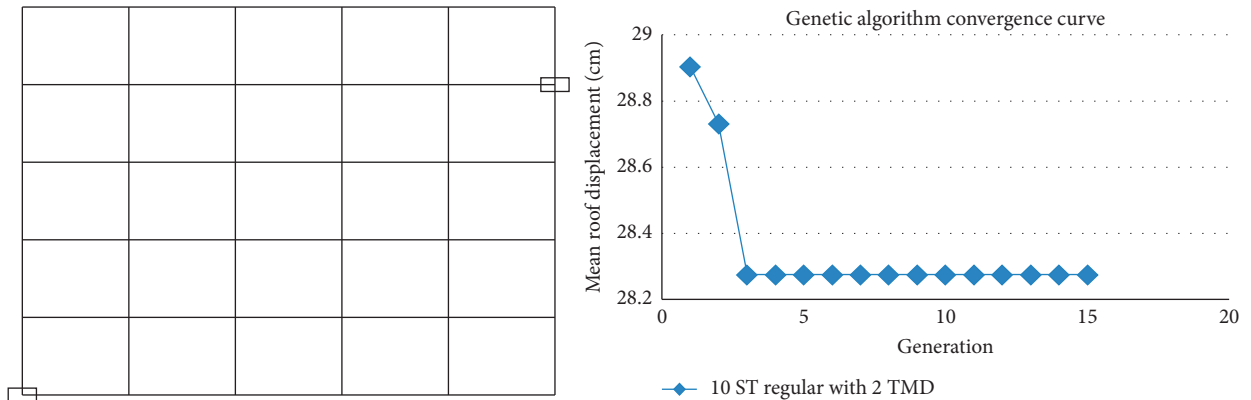


FIGURE 17: Convergence diagram of the ten-story model with 2 dampers in genetic algorithm (right) and damper optimal positions (left).

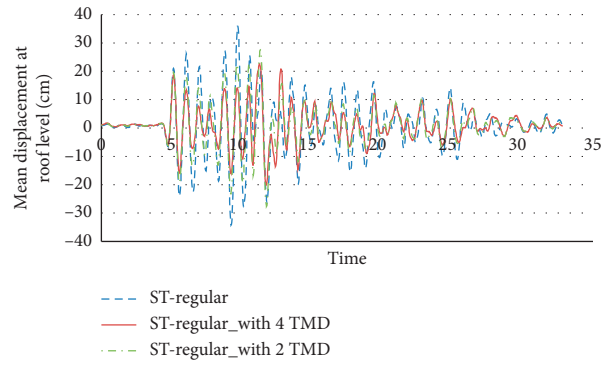


FIGURE 18: Displacement of the ten-story regular model with 2 and 4 dampers.

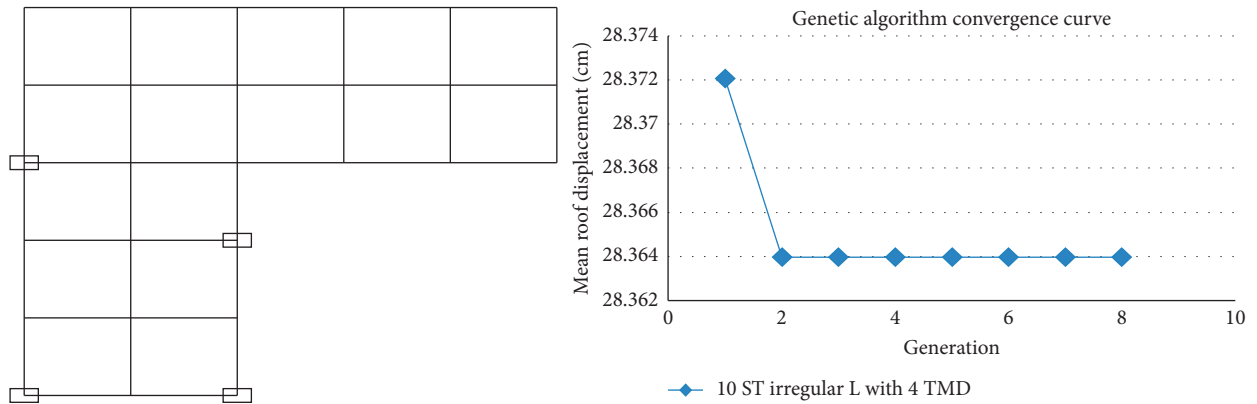


FIGURE 19: Convergence diagram of the ten-story model with 4 dampers in genetic algorithm (right) and damper optimal positions (left).

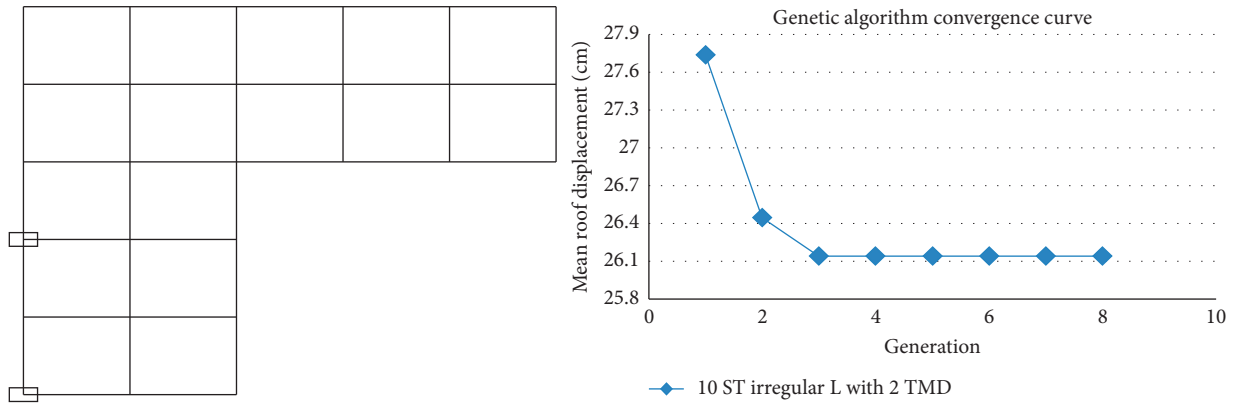


FIGURE 20: Convergence diagram of the ten-story model with 4 dampers in genetic algorithm (right) and damper optimal position (left).

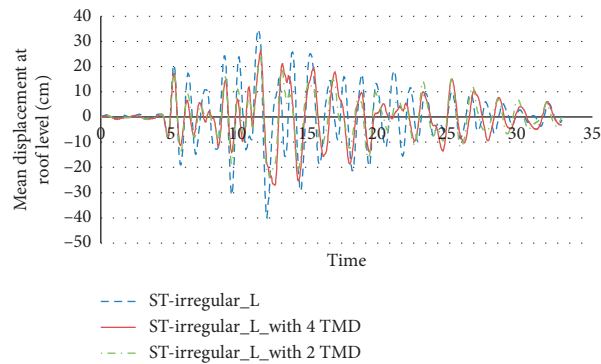


FIGURE 21: Displacement of the ten-story irregular L-shaped model with 2 and 4 dampers.

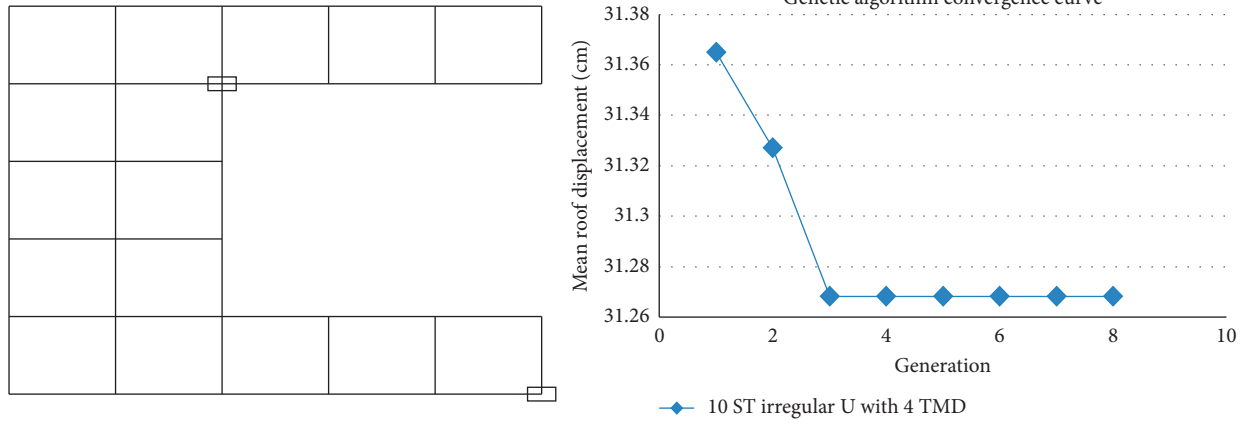


FIGURE 22: Convergence diagram of the ten-story U-shaped model with 4 dampers in genetic algorithm (right) and damper optimal positions (left).

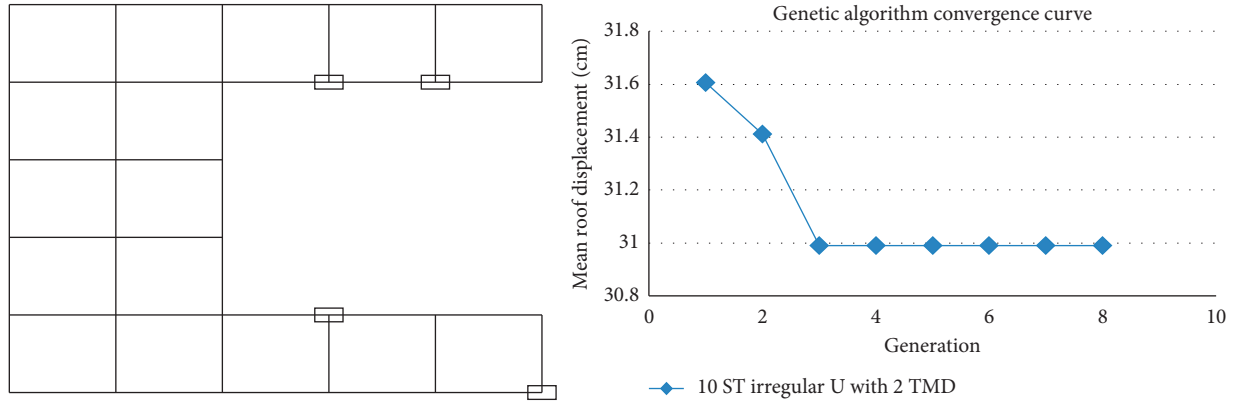


FIGURE 23: Convergence diagram of the ten-story U-shaped model with 2 dampers in genetic algorithm (right) and damper optimal positions (left).

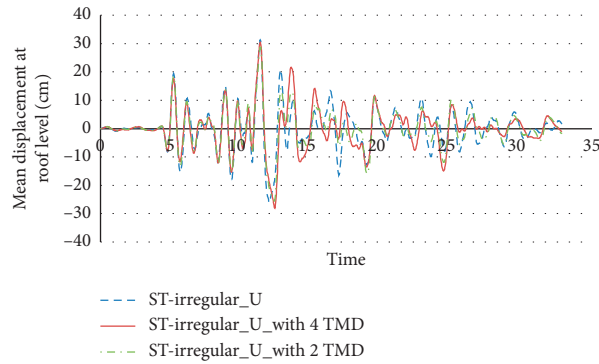


FIGURE 24: Displacement of the ten-story irregular U-shaped model with 2 and 4 dampers.

condition with four dampers, where these numbers are the number of nodes at the roof level), the structure is programmed and analyzed by MATLAB using API functions and the maximum displacement of the roof is considered as the output of the cost function. All steps of creating, analyzing, and capturing the output are performed automatically using the code written in MATLAB in the cost function section, and finally the optimal position of the dampers for 1,

2, and 4 dampers is reported. The continuous version of genetic algorithm is utilized in this paper (because the continuous version converges earlier and requires fewer generations, coding and decoding steps are not required, and the execution time of the program is also short).

Thus, at the beginning of the algorithm, the number of N positions (2, 1, or 4) is randomly selected as input variables and in 30 different conditions (population numbers). These

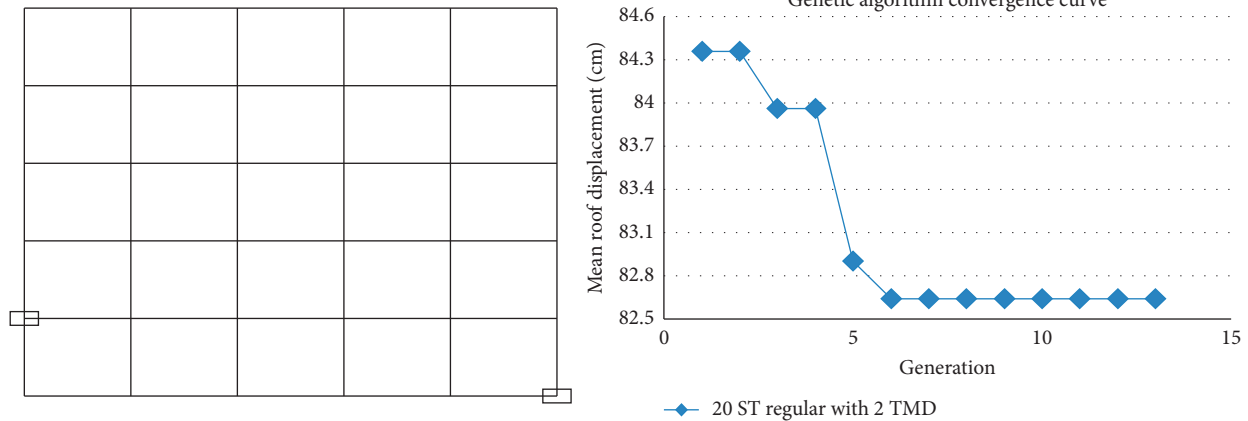


FIGURE 25: Convergence diagram of the twenty-story model with 2 dampers in genetic algorithm (right) and damper optimal positions (left).

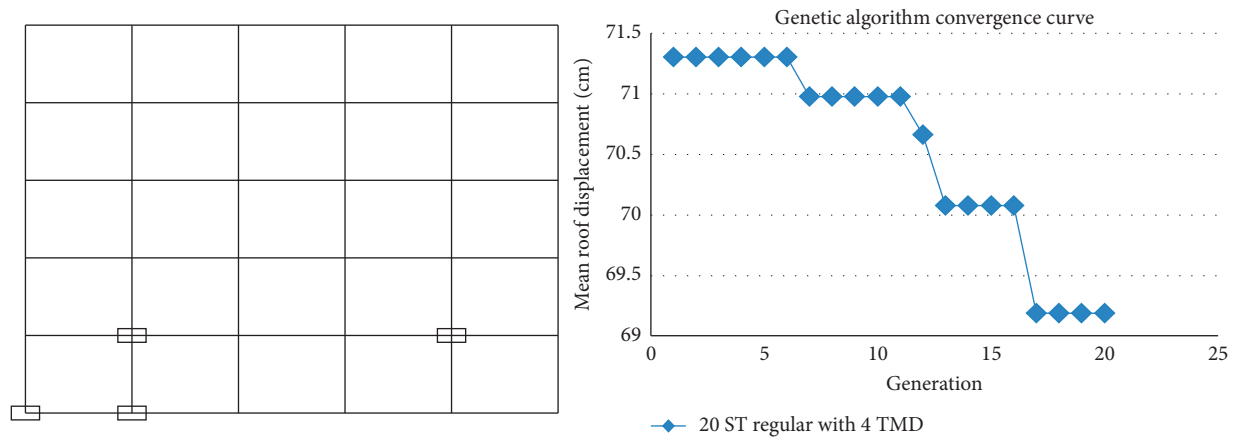


FIGURE 26: Convergence diagram of the twenty-story model with 4 dampers in genetic algorithm (right) and damper optimal positions (left).

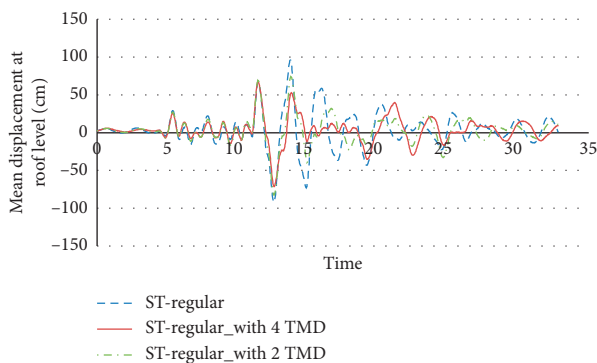


FIGURE 27: Displacement of the twenty-story regular model with 2 and 4 dampers.

variables are the corresponding node number at the roof level of the model created in SAP2000 software, which is defined as a set in MATLAB, and the algorithm uses this set randomly to select variables. For example, to check the optimal position of two dampers in the structure, 30 double families from this collection are selected randomly and entered to the algorithm as the initial population; then, with the initial implementation of the algorithm, 30% of this

population (9 numbers) will be transferred directly to the next generation, and the rest will be included in the transplant and mutation operations and will be the results of the new generation. As mentioned earlier, the cost of each chromosome is calculated in the population generated by the API of the SAP2000 program. In this way, using the API and MATLAB, in each position in each population chromosome, a TMD number with the relevant specifications is placed and the structure is analyzed and the result is extracted as the maximum displacement in the roof level. It should be noted that, in this method, the model without damper in SAP2000 has already been created and the steps of adding damper and analyzing and extracting the results are done by coding. These steps have been repeated for 30 generations. Taking into account the population number and selection rate in each generation of the genetic algorithm, about 700 combinations of different positions of dampers in each model have been investigated. The cost function in the analysis genetic algorithm is considered to be the roof displacement.

In all models, after a maximum of 4 generations, the response to the constant value has been converged, but in order to ensure that the answer to the problem has continued for up to 8 generations, it means for each model about 240 different damper combinations have been examined and

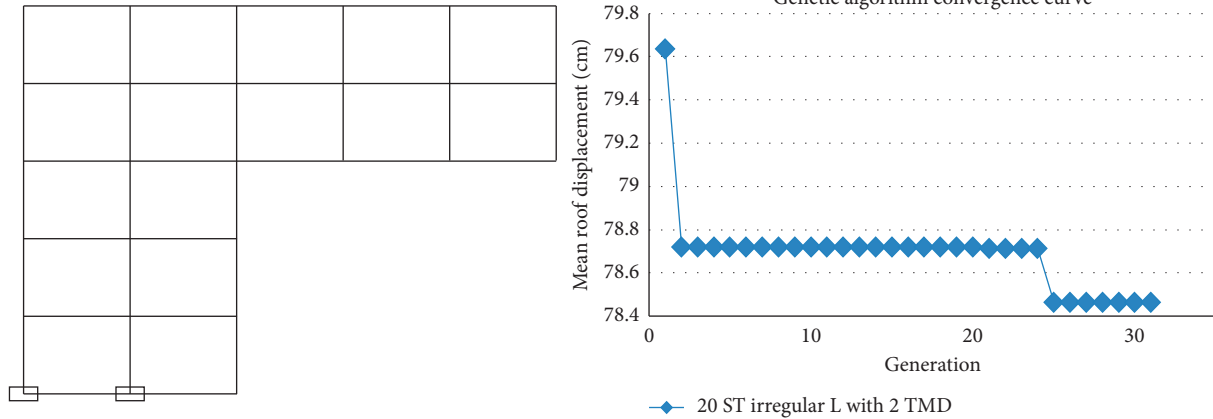


FIGURE 28: Convergence diagram of the twenty-story irregular L-shaped model with 2 dampers in genetic algorithm (right) and damper optimal positions (left).

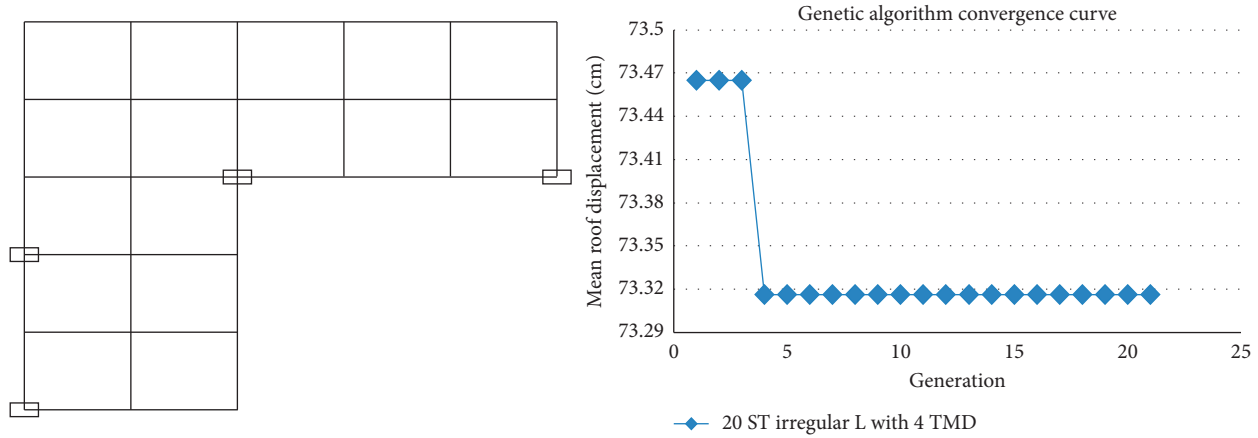


FIGURE 29: Convergence diagram of the twenty-story irregular L-shaped model with 4 dampers in genetic algorithm (right) and damper optimal positions (left).

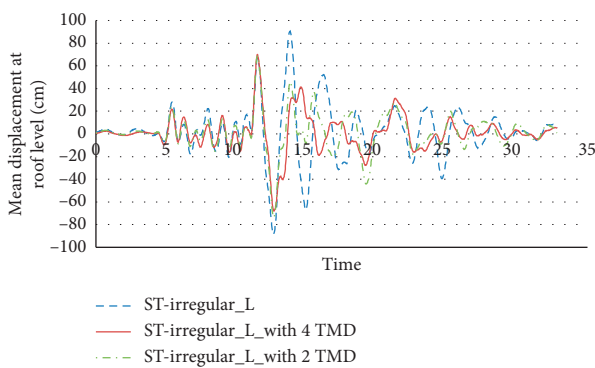


FIGURE 30: Displacement of the twenty-story irregular L-shaped model with 2 and 4 dampers.

in 8 generations all cases have been checked. The stop limitation was not to change the function of the target and the roof movement.

10.1. Modelling and Analysis of Structures. Nonlinear time history analysis under the El Centro earthquake is used to

analyze the structures. The analysis output used to compare and evaluate the number and position of dampers is the maximum displacements of the roof. Modelling, analysis, and comparison of the outputs for different models are performed using the SAP software API.

10.2. API Programming Interface in SAP2000. API programming interface is a valuable tool for CSI software such as SAP and ETABS that allow engineers to exploit them with coding language such as Visual Basic under Excel (VBA), C#, C++, MATLAB, Fortran, and Python. In other words, an engineer using API is capable of coding all ETABS and SAP software commands and tools and accomplishes tasks such as modelling, loading, analyzing, and extracting a variety of results. Engineers can build custom work tools using the API to control CSI software. These tools are able to repeatedly perform time-consuming tasks in a matter of seconds without human error.

10.3. Model Description and Optimization Method for Damper Placement. In this section, the effects of 2 and 4 dampers on the roof level for 10- and 20-story structures are investigated.

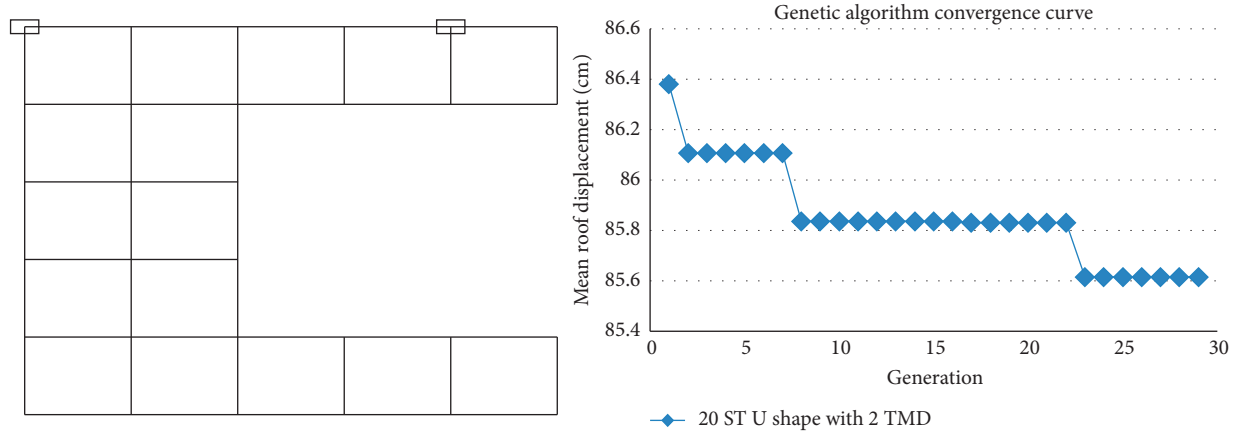


FIGURE 31: Convergence diagram of the twenty-story irregular U-shaped model with 2 dampers in genetic algorithm (right) and damper optimal positions (left).

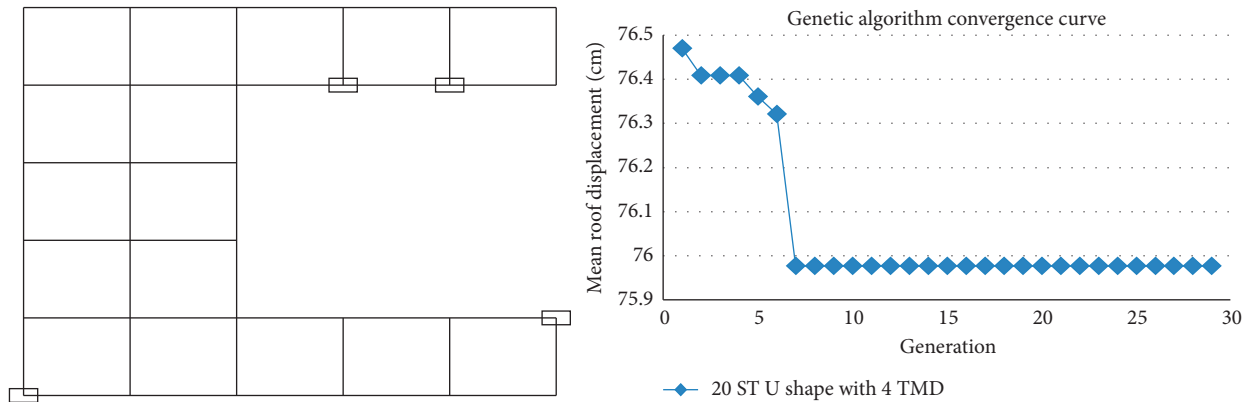


FIGURE 32: Convergence diagram of the twenty-story irregular U-shaped model with 4 dampers in genetic algorithm (right) and damper optimal positions (left).

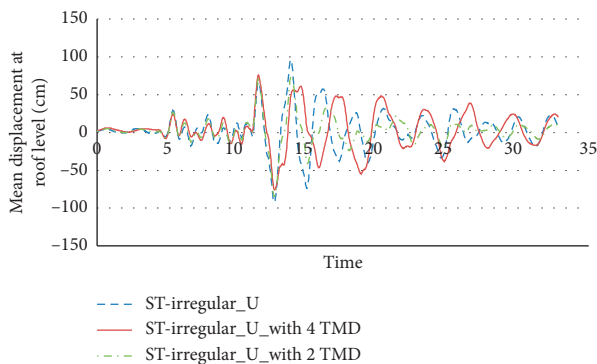


FIGURE 33: Displacement of the twenty-story irregular U-shaped model with 2 and 4 dampers.

For this purpose, the genetic algorithm is used to find the optimal position of these dampers for each number of dampers, so that the position of the structural nodes in the roof level (N variables equal to the number of dampers) is considered as the variable and the optimal combination of these variables is obtained. The cost function of the algorithm is compiled using the SAP software API, for each chromosome in the population consisting of such variables

as 5, 9, 12, and 32 for the case of using 4 dampers, where these numbers are the node numbers in roof level. The structure is created and analyzed using API functions and the maximum roof displacement is considered as the cost function output. All the steps of creating, analyzing, and getting output are done using the code written in MATLAB in the Cost Function section. The algorithm parameters are shown in Table 11.

10.4. Results of Optimal Location of Dampers in 10-Story Regular and Irregular Structures. All models converged to a constant value after a maximum of 4 generations, but it continued for up to 8 generations to ensure the problem is answered (approximately 240 different damper combinations are examined for each model). The locations of the dampers in the cases of using 4 and 2 dampers obtained from genetic algorithm are shown for different structures in Figures 16–24.

The results indicate the significant effects of the mass dampers on the structures. Multiple dampers' symmetrical placement in the plan also plays an important role in the results and responses and the changes in the positions of dampers have insignificant effect in the response of the

structure if their overall positional symmetry does not disagree with the plan axes. In other words, proper and symmetric mass distribution of the mass dampers in the plan plays an important role in reducing the seismic responses of the structures. It can also be noted that the mass dampers with their mass and stiffness change the dynamic characteristics of the structures and affect the seismic responses. Therefore, if the placement of the mass dampers can bring the centre of mass closer to the centre of rigidity, it can reduce the amount of irregularities and its effects and optimize the seismic behavior of the structure. What is considered in determining the optimum position of the mass dampers is their symmetrical positioning which improves the seismic response of the structures. In irregular U-shaped structures, the distribution of dampers is almost symmetric. As it can be seen, the damper optimal positioning approaches the centres of mass and rigidity to each other and reduces the eccentricity and, as a result, improves the responses in irregular L-shaped structures.

10.5. Optimal Position Results of Dampers in Regular and Irregular Twenty-Story Structures. All models converged to a constant value after a maximum of 4 generations, but it continued for up to 8 generations to ensure the problem is answered (approximately 240 different damper combinations are examined for each model). The locations of the dampers in the cases of using 4 and 2 dampers obtained from genetic algorithm are shown for different structures in Figures 25–33.

11. Conclusions

In this research, the effects of optimal number and position of multiple mass dampers on 10 and 20 regular and irregular steel buildings are investigated. The increasing use of high-rise buildings for economic and technical reasons has led to increased research into the control of such structures against earthquake and wind forces and their technical efficiency. Plan irregularity is also one of the important issues that designers and earthquake specialists face. In this research, a wide range of near- and far-field records with different earthquake intensities and parameters are used, and the dampers are designed and installed with respect to the dynamical relationships and the models are analyzed by nonlinear time history analysis. The results show a more desirable effect of using more dampers in models than single mass dampers. Placing dampers at more than one point further reduces the seismic response of the structures and increases the reduction rate of each response such as base shear, displacement, and acceleration of floors. As the dampers are positioned at different points, the mass distribution at the floor level is increased; thereby the applied force by the accelerated mass and the responses are reduced, but when the concentrated mass is positioned at one point of the structure, the applied acceleration to the point is increased and thereby less control is achieved over the seismic response of the structure. The results show that, in most far- and near-field records, when the dampers are

positioned at four symmetrical points in the plan, the internal effort of the resisting members in a story is simultaneously contributed against the increasing applied forces by mass and thereby the responses of the structure are reduced due to the reduction of applied acceleration to the floors and the increase of the time period by controlling the amount of torsion in the irregular structures and the appropriate mass distribution between the lateral elements. It is observed that the effect of mass dampers for different earthquake records has considerable differences, because the characteristics and frequency content of far- and near-field records have differences such as maximum ground acceleration (PGA), magnitude, distance from the fault, the amount of energy released, and the durability, so adding a mass damper changes the dynamic properties and affects the effective frequency of the structure. In the same number of dampers in the far-field records, there is a reduction in the acceleration changes and in the near-field records, the maximum acceleration is observed. In general, multiple dampers in the near-field domain have a better performance in reducing the acceleration of the models, which is also true for floor displacements. The story base shear reduction is observed in the near-field domain and increasing number of dampers. The 45% reduction on average for displacement, base shear, and acceleration of the model floors using multiple mass dampers clearly indicates the appropriate performance of this device in improving the performance of structures. The results show that there is no significant change in the results of the seismic parameters due to changing the dampers position from the tenth floor to the ninth floor. In the ninth floor, the increase in the number of dampers also indicates the distribution of the dampers mass and the contribution of the dampers in controlling the response and the optimal performance of the structure. In irregular L-shaped structures, the position of the dampers in optimal mode brings the mass centre closer to the centre of rigidity and reduces the rate of eccentricity, and the results are significantly improved. Therefore, if the placement of mass dampers can bring the centre of mass closer to the centre of rigidity, it can reduce the irregular value and its effects and optimally improve seismic behavior. What has been considered in determining the optimal position of mass dampers is their symmetrical placement, which has improved seismic response in structures. In irregular U-shaped structures, the distribution of dampers has been almost symmetrical. In the case of optimum positioning using genetic algorithm, the results show that the symmetry of the dampers position in the plan plays an important role in the results and responses, and the positioning of multiple dampers symmetrically in the irregular structures plan plays an important role in the results and responses and the position changes of each damper are neglectable in the seismic response of the structures if their overall position relative to the plan axis is preserved. In other words, the appropriate and symmetric mass distribution of the dampers in the plan has an important role in reducing the seismic response of the structures. In irregular L-shaped structures, the damper optimal position approaches the centre of mass to the

centre of rigidity, reduces the eccentricity, and improves the results significantly.

Data Availability

No data were used to support this study.

Conflicts of Interest

The authors declare that they have no conflicts of interest.

References

- [1] K. Bargi, *Fundamentals of Earthquake Engineering*, University of Tehran, Tehran, Iran, 1st edition, 2007.
- [2] M. Soto, "Investigation of passive control of irregular building structures using bidirectional tuned mass damper," M.Sc. thesis, The Ohio State University, Columbus, OH, USA, 2012.
- [3] M. Abbasi, "Investigating and evaluating the performance of mass-dampers regulated in reducing the non-elastic seismic requirements of tall buildings," M.Sc. thesis, University of Rajaei, Tehran, Iran, 2012.
- [4] H. Frahm, "Device for damping of bodies," US Patent No 989, 1911.
- [5] J. Ormondroyd and J. P. Den Hartog, "The theory of dynamic vibration absorber," *Transactions of the ASME*, vol. APM50-7, pp. 9–22, 1928.
- [6] G. Chen, "Multi-stage tuned mass damper," in *Proceedings of the 11th World Conference on Earthquake Engineering*, Acapulco, Mexico, 1996.
- [7] A. Clark, "Multiple passive tuned mass dampers for reducing earthquake induced building motion," in *Proceedings of the 9th World Conference on Earthquake Engineering*, vol. 5, pp. 779–784, Kyoto, Japan, 1988.
- [8] R. McNamara, "Tuned mass dampers for buildings," *Journal of the Structural Division, ASCE*, vol. 103, no. 9, pp. 1785–1798, 1977.
- [9] G. B. Warburton and E. O. Ayorinde, "Optimum absorber parameters for simple systems," *Earthquake Engineering and Structural Dynamics*, vol. 8, no. 3, pp. 197–217, 1982.
- [10] R. Villaverde and L. A. Koyama, "Damped resonant appendages to increase inherent damping in buildings," *Earthquake Engineering & Structural Dynamics*, vol. 22, no. 6, pp. 491–507, 1993.
- [11] P. Wirsching and G. W. Campbell, "Minimal structural response under random excitation using the vibration absorber," *Earthquake Engineering and Structural Dynamics*, vol. 2, pp. 303–312, 1974.
- [12] M. Abé and T. Igusa, "Tuned mass dampers for structures with closely spaced natural frequencies," *Earthquake Engineering & Structural Dynamics*, vol. 24, no. 2, pp. 247–261, 1995.
- [13] R. S. Jangid, "Dynamic characteristics of structures with multiple tuned mass dampers," *Structural Engineering and Mechanics*, vol. 3, no. 5, pp. 497–509, 1995.
- [14] C. Li, "Performance of multiple tuned mass dampers for attenuating undesirable oscillations of structures under the ground acceleration," *Earthquake Engineering & Structural Dynamics*, vol. 29, no. 9, pp. 1405–1421, 2000.
- [15] A. Kareem and S. Kline, "Performance of multiple mass dampers under random loading," *Journal of Structural Engineering*, vol. 121, no. 2, pp. 348–361, 1995.
- [16] M. M. Abdullah, J. H. Hanif, A. Richardson, and J. Sobanjo, "Use of a shared tuned mass damper (STMD) to reduce vibration and pounding in adjacent structures," *Earthquake Engineering & Structural Dynamics*, vol. 30, no. 8, pp. 1185–1201, 2001.
- [17] S. M. Zahrai and A. Ghannadi, "Seismic performance of TMDs in improving the response of MRF building," *Scientia Iranica*, vol. 15, no. 1, pp. 21–33, 2008.
- [18] A. Tuan and G. Q. Shang, "Vibration control in a 101-storey building using a tuned mass damper," *Journal of Applied Science and Engineering*, vol. 17, no. 2, pp. 141–156, 2014.
- [19] S. Hirde and R. Aher, "Seismic evaluation of irregular structures," *International Journal of Engineering Research*, vol. 5, pp. 750–755, 2016.
- [20] M. G. Soto and H. Adeli, "Optimum tuning parameters of tuned mass dampers for vibration control of irregular highrise building structures," *Journal of Civil Engineering and Management*, vol. 20, no. 5, pp. 609–620, 2014.
- [21] M. R. Wakchaure, A. Shirish, and R. Nikam, "Study of plan irregularity on high-rise structures," *International Journal of Innovative Research & Development*, vol. 1, no. 8, pp. 269–281, 2012.
- [22] E. Valmundson and J. M. Nau, "Seismic response of building frames with vertical structural irregularities," *Journal of Structure Engineering, ASCE*, vol. 123, no. 1, pp. 30–41, 1997.
- [23] B. S. K. Reddy, L. Madhavi, and C. H. Srikanth, "Analysis of irregular high raised RCC buildings by using tuned mass damping system," *International Journal of Advanced Engineering Research and Science (IJAERS)*, vol. 5, no. 3, 2018.
- [24] S. Bagheri and V. Rahmani-Dabbagh, "Seismic response control with inelastic tuned mass dampers," *Engineering Structures*, vol. 172, pp. 712–722, 2018.
- [25] W. Wang, X. Wang, X. Hua, G. Song, Z. Chen, and Z. Chen, "Vibration bridge deck by a single-side pounding tuned mass damper," *Journal of Engineering Structures*, vol. 173, pp. 61–75, 2018.
- [26] L. Li and C. Peng, "Novel approach of a nonlinear tuned mass damper with duffing stiffness," *Journal of Engineering Mechanics*, vol. 143, no. 4, Article ID 04017004, 2017.
- [27] Z. Lu, L. Kun, and Z. Ying, "Comparative studies on structures with a mass damper and particle damper," *Journal of Aerospace Engineering*, vol. 31, no. 6, Article ID 04018090, 2018.
- [28] J.-L. Lin, "Top-story mass dampers for seismic control of the first triplet of vibration modes of two-way asymmetric-plan buildings," *Journal of Vibration and Control*, vol. 23, no. 18, pp. 2962–2976, 2017.
- [29] Z. Lu, K. Li, and Y. Zhou, "Comparative studies on structures with a tuned mass damper and a particle damper," *Journal of Aerospace Engineering (ASCE)*, vol. 31, no. 6, 2018.
- [30] R. Kamgar, M. Khatibinia, and M. Khatibinia, "Optimization criteria for design of tuned mass damper including soil-structure interactive effect," *International Journal of Optimization in Civil Engineering*, vol. 9, no. 2, pp. 213–232, 2019.
- [31] S. Elias and V. Matsagar, "Seismic vulnerability of a nonlinear building with distributed multiple tuned vibration absorbers," *Structure and Infrastructure Engineering*, vol. 15, no. 8, pp. 1103–1118, 2019.
- [32] H. R. Rahmani and C. Könke, "Seismic control of tall buildings using distributed multiple tuned mass dampers," *Advances in Civil Engineering*, vol. 2019, Article ID 6480384, 19 pages, 2019.
- [33] M. Yucel, G. Bekdaş, S. M. Nigdeli, and S. Sevgen, "Estimation of optimum tuned mass damper parameters via machine learning," *Journal of Building Engineering*, vol. 26, Article ID 100847, 2019.
- [34] B. Keshtegar and S. Etedali, "Nonlinear mathematical modeling and optimum design of tuned mass dampers using

- adaptive dynamic harmony search algorithm,” *Structural Control and Health Monitoring*, vol. 25, no. 7, p. e2163, 2018.
- [35] S. M. Nigdeli and G. Bekdaş, “Optimum design of multiple positioned tuned mass dampers for structures constrained with axial force capacity,” *The Structural Design of Tall and Special Buildings*, vol. 28, no. 5, p. e1593, 2019.
 - [36] M. Shahi, M. R. Sohrabi, and S. Etedali, “Seismic control of high-rise buildings equipped with ATMD including soil-structure interaction effects,” *Journal of Earthquake and Tsunami*, vol. 12, no. 3, Article ID 1850010, 2018.
 - [37] S. Etedali, M. Akbari, and M. Seifi, “MOCS-based optimum design of TMD and FTMD for tall buildings under near-field earthquakes including SSI effects,” *Soil Dynamics and Earthquake Engineering*, vol. 119, pp. 36–50, 2019.
 - [38] F. Sadek, B. Mohraz, A. W. Taylor, and R. M. Chung, “A method of estimating the parameters of tuned mass dampers for seismic applications,” *Earthquake Engineering & Structural Dynamics*, vol. 26, no. 6, pp. 617–635, 1997.
 - [39] Building and Housing Research Center, *Iranian Code of Practice for Seismic Resistant Design of Buildings*, Building and Housing Research Center, Tehran, Iran, 2015.
 - [40] G. Chen and N. Wu, “Experimental study multiple tuned mass dampers to reduce seismic responses of a three-storey building structure,” *Earthquake Engineering and Structural Dynamics*, vol. 32, pp. 793–810, 2003.

Research Article

Enhancing the Seismic Performance of Precast RC Frames with Cladding Panels through Setting U-Shaped Dampers and Rocking Walls

Qing Jiang ^{1,2} **Hanqin Wang**¹ **Yulong Feng** ^{1,2} **Xun Chong**^{1,2} **Junqi Huang**^{1,2}
and **Yibo Liu**¹

¹*School of Civil Engineering, Hefei University of Technology, Hefei 230009, Anhui, China*

²*Anhui Civil Engineering Structures and Materials Laboratory, Hefei 230009, Anhui, China*

Correspondence should be addressed to Yulong Feng; feng_yulong@126.com

Received 21 February 2020; Revised 17 May 2020; Accepted 22 May 2020; Published 16 June 2020

Academic Editor: Alfredo Reyes-Salazar

Copyright © 2020 Qing Jiang et al. This is an open access article distributed under the Creative Commons Attribution License, which permits unrestricted use, distribution, and reproduction in any medium, provided the original work is properly cited.

An approach combining U-shaped dampers (USDs) and rocking walls is proposed in this paper to improve the seismic performance of traditional precast reinforced concrete (RC) frames with cladding panels (PRCFCPs): (1) the steel bar and USD connection methods are adopted at the top and bottom of the cladding panels to use the relative deformation between the cladding panels and the main structure and then dissipate the seismic energy and (2) rocking walls are added to the structure to control the structural deformation profiles. The USD numerical model is calibrated using the test data, and a series of nonlinear pushover analyses, dynamic time-history analyses, and incremental dynamic analyses are successively performed to compare the seismic performance and collapse capacity of the PRCFCP, PRCFCP with USDs (PRCFCP-USD), and PRCFCP with USDs and rocking walls (PRCFCP-USD-RW). The results show that the USDs in the PRCFCP-USD-RW undergo more uniform deformation along the structural height and higher energy dissipation efficiency and the PRCFCP-USD-RW exhibits enhanced seismic performance and collapse capacity, which verify the superiority of the proposed combined approach.

1. Introduction

Precast concrete cladding panels (PCCPs), fabricated at manufacturing plants and assembled on a supporting main structure at the project site, have been widely used as an architectural external wall system during the past several decades [1]. Losch et al. [2] described the art of precast/prestressed concrete sandwich wall panels and noted that the use of this kind of PCCP has become more widespread in the United States. According to the current design specification [3, 4], PCCPs are primarily designed as a nonstructural member to bear their self-weight and out-of-plane loads, including seismic and wind loads.

Belleri et al. [5] summarized the vulnerabilities of the cladding panels following major earthquakes in the Italian territory and noted that the interaction between the cladding panels and the main structure was a noticeable vulnerability

of the structure. The connection details between the cladding panels and the supporting structure significantly affect their interaction, which might reduce the performance and safety of both panels and main structure [6, 7]. To mitigate the interaction and reduce the sensitivity of the PCCP to the deformation of the main structure, the Precast Concrete Institute (PCI) recommends that the force transmission path from the cladding panel to the main structure should be statically determinate, each cladding panel should not be more than two gravity-bearing connections, and those connections should be placed in the same horizontal position [3]. Thus, the commonly used connection form is a four-point flexible connection, including two gravity-bearing connection points and two lateral force-bearing connection points. At present, the steel bar and limiting device connection methods are adopted at the top and bottom of the cladding panels in China [4], as shown in Figure 1(a),

where the steel bars are placed at the top of the cladding panel and protrude into the floor cast-in-place layer; limiting devices constructed by angle steel are connected with the cladding panel and main structure by long bolts. The steel bar and limiting device connection can resist out-of-plane displacement of the cladding panel and prompt the cladding panel sliding in-plane. The PCCPs with the aforementioned connection forms will exhibit sliding or rocking deformation under an earthquake. These deformation modes are recommended to coordinate the deformation of the main structure and reduce the interaction between the cladding panels and the main structure to enhance the structural safety [8].

Accordingly, there is a relative deformation between the cladding panels and the main structure, in which various energy dissipaters were arranged by many scholars to improve the seismic performance of the structures with PCCPs. Tyler [9] used polytetrafluoroethylene sliding joints to separate the cladding panels from the main structure of a building and noted that their use enables the damping of earthquake and wind motions. Cohen and Powell [10] classified the energy-consuming connections around the cladding panels and studied the design methods of these connections. Pinelli et al. [11] connected the cladding panel and the main structure by an elliptical soft steel energy dissipater. The test and finite element analyses showed that the performance of this energy-dissipating connection form was stable. Ferrara et al. [12] experimentally evaluated the behaviour of friction dampers to be used along the edges of the cladding panels in precast reinforced concrete (RC) buildings. Baird et al. [13] installed U-shaped flexural plates at the lateral connection point of the four-point connected cladding panel and found that the U-shaped flexural plates can effectively dissipate seismic energy and reduce the deformation of the structure under earthquakes. Negro and Lamperti Tornaghi [14] investigated PCCPs with friction-based devices, and the reliability was confirmed by several tests. Lago et al. [15, 16] proposed a steel w-shaped folded plate dissipative connector and a multiple-slit device for the PCCPs. The test results showed that the proposed devices can be effectively used for precast RC structures with cladding panels. Karadoğan et al. [17] arranged steel cushions that have excellent dissipation capacity between the main structure and PCCPs. The test results showed that the plastic deformations accumulated on the steel cushions, and no damage was observed on the PCCPs; using bolts to connect the steel cushions and PCCPs is a reliable connection technique.

The soft-storey failure of RC frames has been mentioned by some existing studies, and rocking systems have proven to be an effective means to control the structural deformation and damage distribution [18, 19]. In particular, the rocking systems and the energy dissipaters have been frequently combined to obtain enhanced seismic performance structures. Deierlein et al. [20] proposed an earthquake resilient rocking steel frame system with energy-dissipating fuses and confirmed that the system can sustain extreme earthquake ground shaking without structural damage. Wada et al. [21] retrofitted the G3 teaching building at Tokyo Industrial

University with rocking walls and steel dampers. This structure survived the 2011 Miyagi earthquake. Twigden and Henry [22] experimentally investigated a posttensioned rocking wall with energy-dissipating O-connectors attached along the vertical. Zhang et al. [23] combined precast rocking walls and friction dampers or buckling-restrained braces to form an inertial force-limiting floor anchorage system that is a low-damage seismic-resistant system. Feng et al. [24] used rocking walls to mitigate the drift concentration issue of buckling-restrained braced frames. Rahgozar et al. [25] numerically investigated the effects of soil-foundation modelling on the seismic performance of rocking braced frames with butterfly-shaped fuses. These studies indicated that the rocking systems might make the energy dissipaters work more effectively.

In this paper, in order to retrofit the existing structure of the precast RC frame with cladding panels (PRCFCPs), U-shaped dampers (USDs) that were developed in 1972 by Kelly et al. [26] and rocking walls are added into a PRCFCP to form a damping and damage-controlling system. This paper focuses on the effect of the USDs and rocking walls on the seismic performance of the PRCFCP through numerical investigations and comparative analyses. A series of nonlinear pushover analyses, dynamic time-history analyses, and incremental dynamic analyses are performed to compare the seismic performance and the seismic collapse capacity of the PRCFCP, PRCFCP with the USDs (PRCFCP-USD), and PRCFCP with the USDs and rocking walls (PRCFCP-USD-RW).

2. Description of the Structural System

2.1. Connection Details. Figure 1(b) shows a connection detail of the proposed damping cladding panels. A precast concrete sandwich wall panel is used as the cladding panel and connected to the main structure at each storey. The cladding panel is connected to the upper and down floors through a row of steel bars and USDs at the top and bottom of the cladding panel, which are deemed the steel bar and USD connection methods, respectively. The USDs are connected to other members through high-strength bolts [17, 27]. In this steel bar connection method, two layers of steel bars are placed at the top of the cladding panel and protrude into the floor cast-in-place layer, and then a fixed constraint end is formed to resist out-of-plane loads. Thus, the construction quality and earthquake safety are easily guaranteed. For the entire cladding panel that spans a single storey using these connection methods, the deformation mode under a horizontal earthquake is dominated by horizontal sliding deformation at the bottom of the cladding panel. Thus, the USDs that are set in the places where USDs undergo horizontal sliding deformations can dissipate energy through their own plastic deformations, as shown in Figure 1(c).

2.2. Structural Systems. Figure 2 describes the schematic of PRCFCP-USD-RW as a retrofitting structure of PRCFCP, which consists of a precast RC frame with the proposed

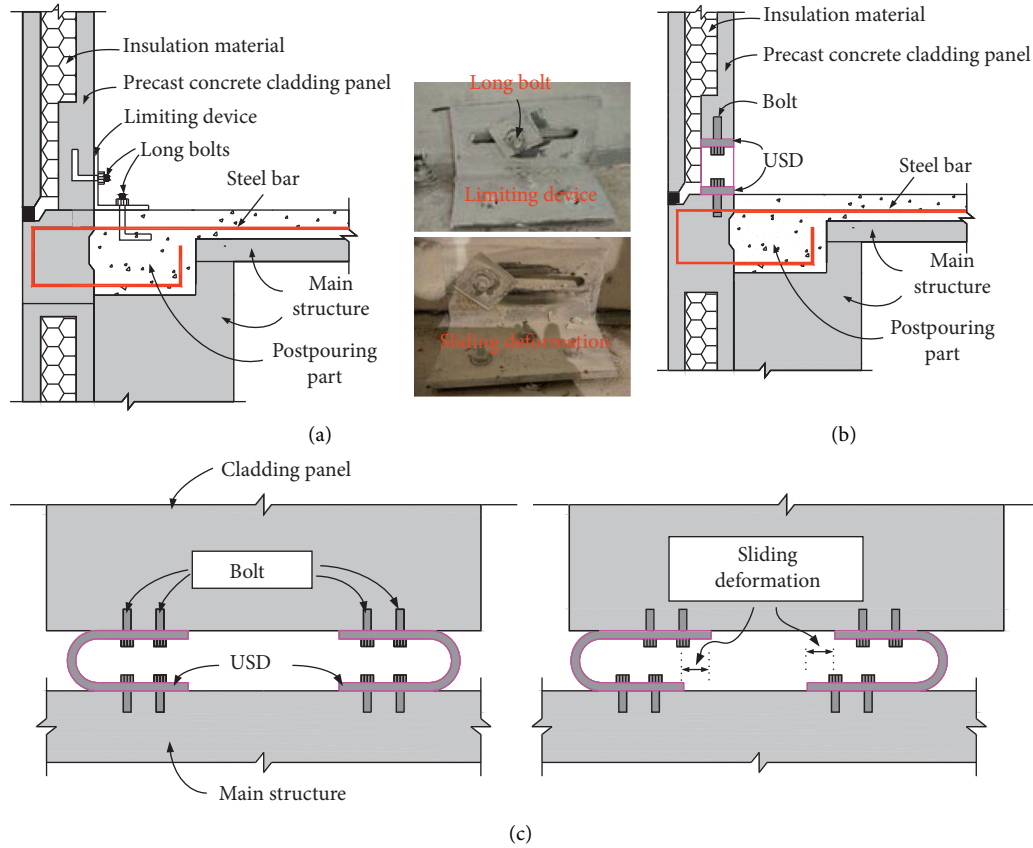


FIGURE 1: Connection details and deformation mode of the proposed damping cladding panel. (a) Typical cladding connection 2 in China. (b) Connection details. (c) Deformation mode of the proposed damping cladding panel.

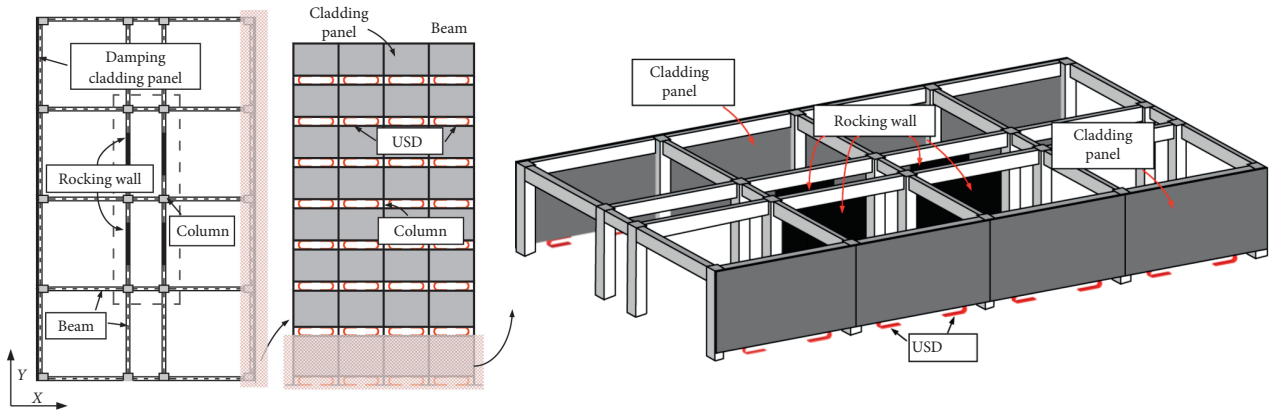


FIGURE 2: Schematic of a PRCFCP-USD-RW system.

cladding panels, as shown in Figure 1, and some rocking walls are attached only to beams at the middle of the structure in the Y direction. The cladding panels in the PRCFCP-USD-RW are no longer a nonstructural element but are a support member of the USDs. Together with the USDs, a shock absorbing unit is formed to transmit the interstorey drift generated by the earthquake to the USDs, and the plastic deformation of the USDs is used to dissipate

the seismic energy to reduce the main structural damage. The rocking walls can render the storey drift of the structure uniform. When the storey drift is uniform, the USDs at each storey can exert an energy dissipation capacity. The collaboration between the USDs and the rocking walls plays a dual role in coordinating the interstorey drift and energy dissipation to achieve a controllable damage degree and distribution.

3. Contrast Models and Finite Element Models

3.1. Calibration of the USD Model. OpenSees [28] numerical simulation software is used for the nonlinear analysis in this paper. The definition of the USD parameters in the model is based on the force-displacement curve obtained from a test performed by the authors. Figure 3(a) shows the USD test model and loading device. The length, width, height, and thickness of the USD are 276 mm, 70 mm, 174 mm, and 12 mm, respectively. The material of the USD is Q235 steel (GB50017-2003) [29]. Figure 3(b) shows the loading protocol in this test. The loading amplitude displacements of each stage are 3 mm, 7 mm, 14 mm, 28 mm, 42 mm, and 60 mm, respectively. The front five stages are cycled three times, and the last stage is cycled approximately 18 times. The USD in OpenSees uses the Steel02 model and the zero-length element for the simulation [30]. The Steel02 model has a yield force $F_y = 11.97$ kN and initial elastic stiffness $E = 3.99$ kN/mm. The parameters controlling the transition from the elastic stage to the plastic stage are as follows: $R_0 = 20$, $CR_1 = 0.925$, and $CR_2 = 0.15$. Additionally, the isotropic hardening parameters are $a_1 = 0.25$, $a_2 = 5$, $a_3 = 0.25$, and $a_4 = 5$. The definition of these parameters can be found in [28]. Figure 3(c) shows the comparison of force-displacement curves between the simulations and the experiments. The simulated results are basically consistent with the experimental results, indicating that the USD model parameters are set properly.

3.2. Contrast Models. Figure 4(a) shows an 8-storey RC frame structure from [31]. The 8-storey RC frame was designed based on existing Chinese code for the design of concrete structures and seismic design of buildings. However, the soft-storey also occurred in this baseline building under horizontal earthquake loads and can be prevented by the addition of rocking walls, which is the reason to use this 8-storey RC frame herein as a benchmark model to construct other contrast models. The structural plane is a rectangle of 24 m by 50.4 m, and the column spacing is 7.5 m or 3.0 m. The earthquake resisting system of the benchmark model comprises five and four moment-resisting frames (MRFs) at the transverse and longitudinal directions of the structure (X and Y directions), respectively. The first and second storeys have heights of 4.5 m and 4.0 m, respectively, and the upper storeys have a height of 3.5 m, resulting in a total height of 29.5 m. The benchmark model is designed for a seismic area with Site Classification II and design ground Group 1, classified as a zone of intensity 8, with a basic design peak ground acceleration (PGA) of 0.2 g. Two concrete strength grades were adopted, C40 for all beams and floors and C45 for all columns (i.e., the cubic compressive strengths of the concrete are 40 MPa and 45 MPa, resp.). HRB 400 reinforcement (i.e., hot rolled ribbed reinforcement with a yield strength of 400 MPa) was adopted for the longitudinal mild steel reinforcement of beams, floors, and columns. The thickness of all floors was 100 mm, and the distribution steel reinforcements bilaterally distributed were all $\phi 10@200$ ($\phi 10$ means that the diameter of distribution steel reinforcements

is 8 mm; @200 means that the spaces of distribution steel reinforcement are 200 mm). All columns and beams used rigid connections. More information regarding this frame structure, such as the beam-column section size and reinforcement, and design dead and live loads, can be found in [31].

To illustrate the performance advantages of the proposed PRCFCP-USD-RW, three different contrast models are developed based on the benchmark model. Only the Y direction seismic action is considered; thus, the comparison model considers only the addition of the rocking walls and the cladding panels in the Y direction, and the earthquake resisting system in the X direction is the same as the benchmark model. The traditional and damping cladding panels are added to the benchmark model in the Y direction, and the PRCFCP and PRCFCP-USD models are created, as shown in Figures 4(b) and 4(c), respectively. The traditional cladding panels at the bottom are connected by two limiting devices that allow the panel to slide freely under design displacement. In the PRCFCP-USD model, four USDs are arranged at the bottom of each cladding panel, and the size and material of each USD are the same as those shown in Figure 3(a). Furthermore, four rocking walls are added to the PRCFCP-USD model in the Y direction, and the PRCFCP-USD-RW model is formed, as shown in Figure 4(d). The sectional dimension of the rocking walls is the same as that in [31], which is 3600 mm \times 150 mm. The paper focuses on the seismic responses of three comparison models, i.e., PRCFCP, PRCFCP-USD, and PRCFCP-USD-RW.

3.3. Finite Element Models. Figure 5 schematically shows the finite element model of the PRCFCP-USD-RW. The benchmark, PRCFCP, and PRCFCP-USD finite element models are modelled using the same techniques. In this paper, the RC beams, columns, and rocking walls are modelled via displacement-based beam-column (displacement-based beam-column) fibre elements, in which their concrete and steel reinforcement materials use Concrete01 (because the tensile strength is less than the compressive strength, Concrete01 is used to build model) and Steel02 (the elastic tangent of reinforcement is 200 GPa, and strain-hardening ratio is 0.01), respectively. Some approaches have been proposed to model the panels (or walls) such as the multilayer element [32] or rigid beam element [33] with the bottom linked by a nonlinear zero-length element. The cladding panels and floors are simulated by shell elements, and the material adopts an elastic model. Notably, the shell elements for cladding panels are not connected to the adjacent columns, and the master nodes of rigid diaphragm at each storey were set in the structural centroid. The limiting devices in the PRCFCP and the USDs in the PRCFCP-USD and PRCFCP-USD-RW are simulated by zero-length elements, which replaces the translational constraint in the loading direction by a Steel02 material defining the force-displacement relationship shown in Section 3.1. The finite element models for the PRCFCP-USD and PRCFCP-USD-

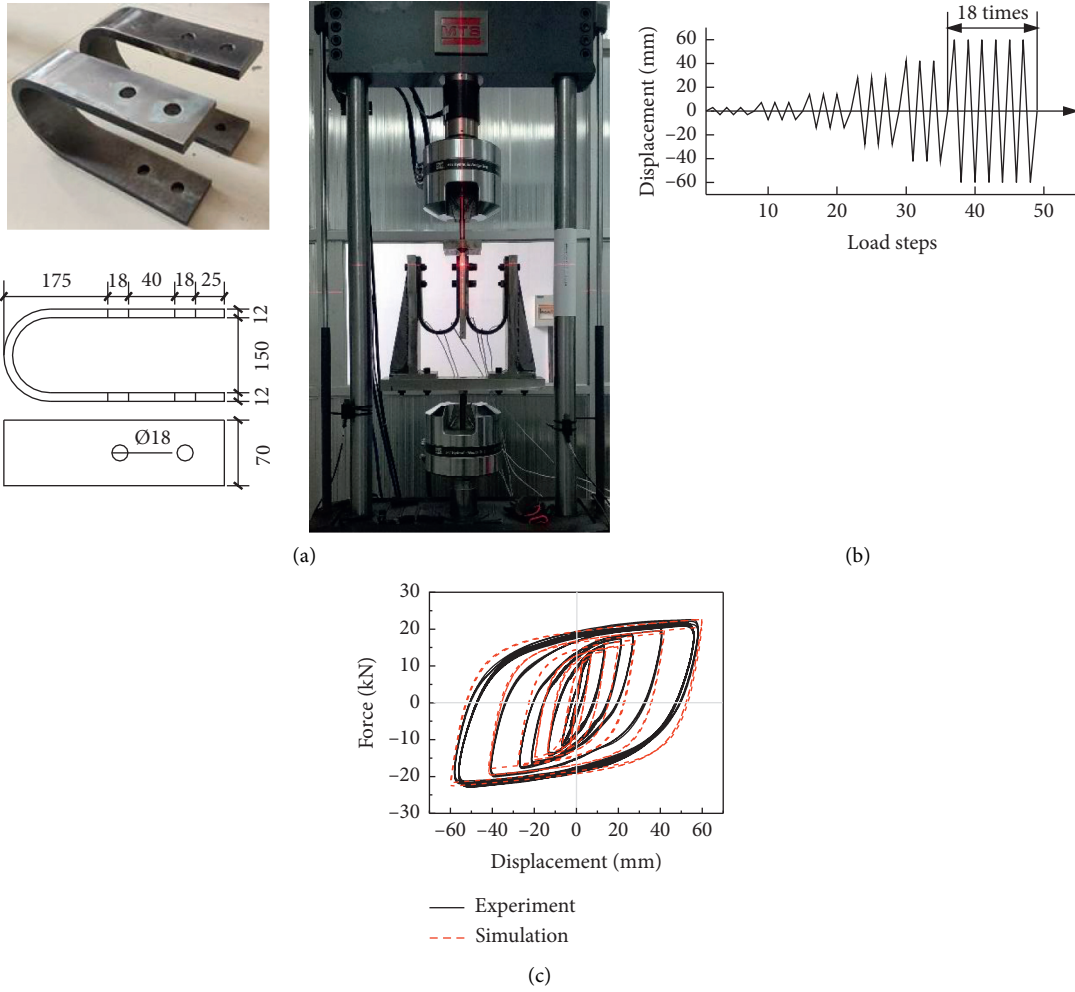


FIGURE 3: Calibration of the USD finite element model. (a) Loading device and the design of the USD (unit: mm). (b) Loading protocol in the test. (c) Comparison of the simulations and experiments.

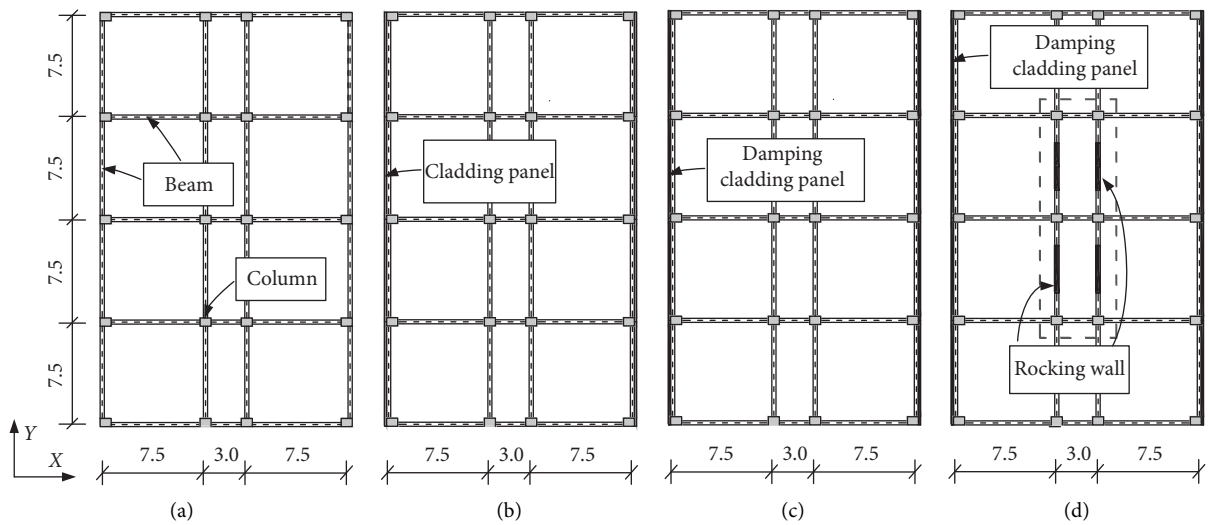


FIGURE 4: Benchmark model and three kinds of contrast models (unit: m). (a) Benchmark model. (b) PRCFCP. (c) PRCFCP-USD. (d) PRCFCP-USD-RW.

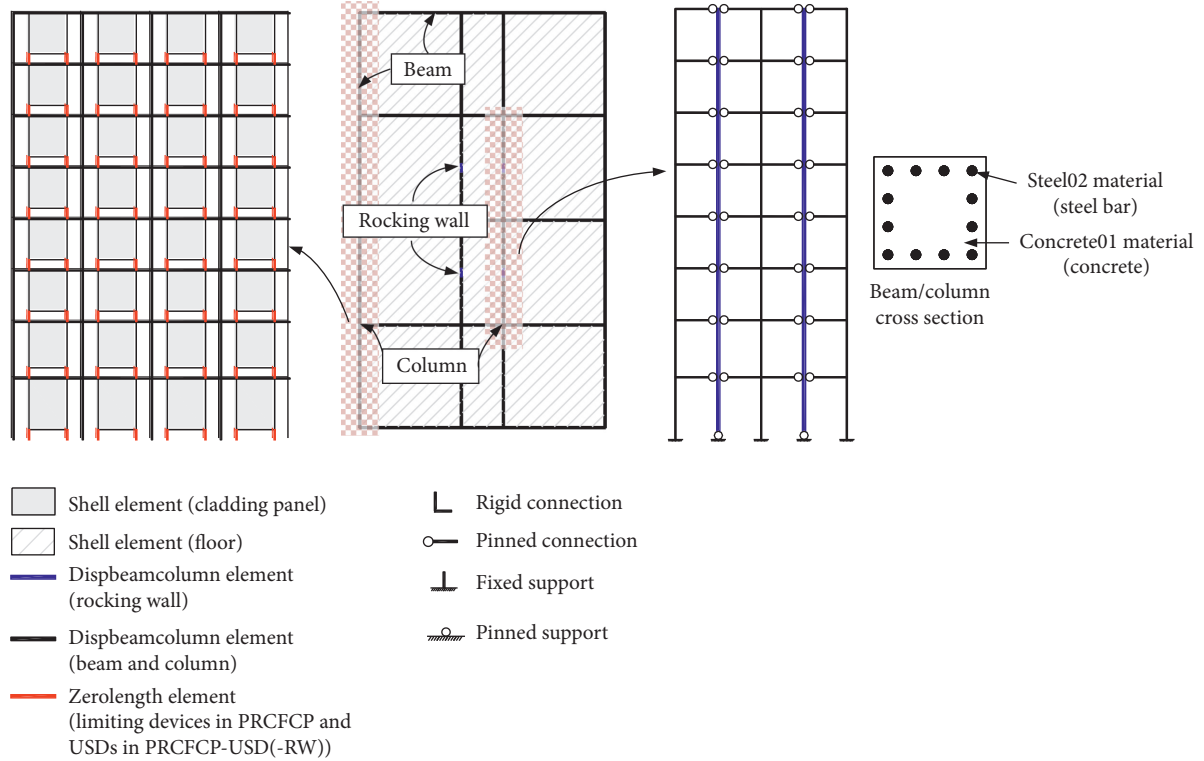


FIGURE 5: Numerical models used in this paper.

RW use one zero-length element to simulate two USDs; therefore, the stiffness and yield force are twice the one USD shown in Figure 3(c). The initial elastic stiffness in the PRCFCP is deliberately set to infinity for the purpose of simulating the free sliding of the cladding panels. The beam/column and beam/rocking walls joints use rigid connections and pinned connections, respectively.

The model mass is added to each storey node in the form of a concentrated mass. The lateral load is an inverted triangle mode in nonlinear pushover analyses, and the Rayleigh damping with natural damping ratio is 0.05 in the nonlinear dynamic time-history analyses. The seismic lateral loads act on the structural Y direction. All nonlinear analyses consider the P-delta effect of gravity. The fundamental periods (T_1) of the benchmark model and three contrast models are shown in Table 1.

3.4. Ground Motions Selection. The dynamic time-history analyses use 22 ground motions recommended in [26], as reported in Table 2. Figure 6 shows the acceleration response spectra for 22 ground motions-adjusted acceleration peaks to 4 m/s^2 and the acceleration design spectrum corresponding to the major earthquake specified by the Chinese code (GB 50011–2010) [34]. The average and design spectrum accelerations (S_a) are similar. This paper focuses on the average value of the structural responses under 22 ground motions. Since the three contrast models have a large response under the 9th ground motion (GM9), this paper also focuses on the performance differences of the comparison

models under the 9th ground motion, and its acceleration time-history curves are shown in Figure 7.

4. Nonlinear Pushover Analyses

Figure 8 shows curves of the base shear force and the roof displacement for the contrast models under inverted triangle lateral load. The curve slope of the PRCFCP-USD is slightly larger than that of the PRCFCP before the structures yield. Therefore, the PRCFCP-USD exhibits a slightly larger lateral stiffness than the PRCFCP, indicating that the addition of the USD can improve the structural stiffness to a certain extent. The lateral load-carrying capacity of the PRCFCP-USD is also slightly larger than that of the PRCFCP, and their base shear forces show a significant downward trend after they reach the peak lateral load-carrying capacity. Figure 8 also shows that the curve slopes of the PRCFCP-USD and PRCFCP-USD-RW structures basically remain consistent before the structures yield, which is mainly because the addition of rocking walls cannot change the lateral stiffness of the structures. Notably, the lateral load-carrying capacity of the PRCFCP-USD-RW is unchanged and is significantly larger than that of the PRCFCP-USD as the loading continues. This result indicates that the lateral load-carrying capacity and ductility of the PRCFCP-USD are enhanced by the participation of the rocking walls.

Figures 9(a)–9(c) show curves of the storey shear force and the storey drift ratio of the frames in the contrast models under the structural pushover. Notably, the interstorey shear force is the sum of the shear forces of all frame columns.

TABLE 1: Periods of all models (the values in brackets are the modal mass participating ratios).

Models	Reference [31]	Benchmark model	PRCFCP	PRCFCP -USD	PRCFCP -USD-RW
T_1 (s)	1.169	1.118 (0.825)	1.051 (0.840)	0.915 (0.861)	0.910 (0.951)

TABLE 2: 22 ground motions recommended in [26].

Number	Earthquake	Year	Component	Magnitude (M)	PGA (m/s^2)
1	Friuli, Italy-01	1976	A-TMZ270	6.50	2.93
2	Imperial Val.-06	1979	H-DLT352	6.53	3.44
3	Imperial Val.-06	1979	H-PTS315	6.53	2.00
4	Superst. Hills-02	1987	B-IVW360	6.54	1.82
5	Loma Prieta	1989	G03090	6.93	3.60
6	Loma Prieta	1989	HDA165	6.93	2.07
7	Loma Prieta	1989	HSP000	6.93	3.63
8	Landers	1992	CLW - TR	7.28	3.04
9	Landers	1992	JOS090	7.28	2.78
10	Landers	1992	YER270	7.28	1.65
11	Northridge-01	1994	LOS270	6.69	4.72
12	Northridge-01	1994	ORR090	6.69	5.57
13	Northridge-01	1994	STM090	6.69	7.38
14	Kobe, Japan	1995	KAK090	6.90	3.38
15	Kobe, Japan	1995	SHI000	6.90	2.38
16	Duzce, Turkey	1999	BOL090	7.14	8.06
17	Chichi, Taiwan-05	1999	TCU029-N	7.62	1.97
18	Chichi, Taiwan-05	1999	TCU070-E	7.62	2.50
19	Chichi, Taiwan-05	1999	TCU095-E	7.62	3.35
20	Wenchuan	2008	UA0097	8.00	4.59
21	Wenchuan	2008	UA0103	8.00	2.79
22	Wenchuan	2008	UA0196	8.00	3.23

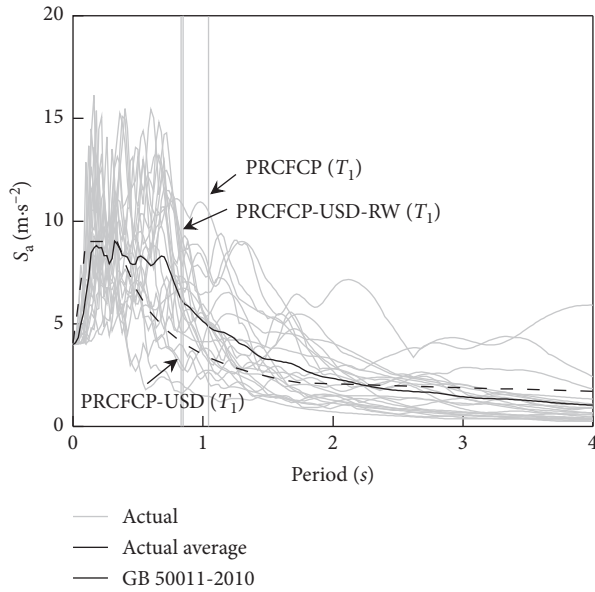


FIGURE 6: Comparison between the design spectrum and the spectra of actual ground motions.

Figure 9(d) shows curves of interstorey drift ratio when the structures arrived at the peak lateral load-carrying capacity.

A drift concentration factor (DCF) was defined by [35] as (1) for the purpose of evaluating the structural lateral deformation mode and damage concentration degree. The parameter θ_{\max} is the maximum interstorey drift ratio, u_{roof}

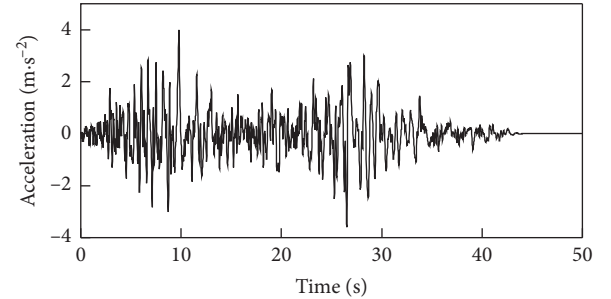


FIGURE 7: Acceleration time-history curve for GM9.

is the structural roof displacement, and H is the structural total height. If $DCF=1$, the structural interstorey drift at each storey is identical. When structures arrive at the peak lateral load-carrying capacity, the DCF values of three contrast models are also listed in Figure 9(d), where DCF_1 - DCF_3 represent the DCF values of the PRCFCP, PRCFCP-USD, and PRCFCP-USD-RW, respectively:

$$DCF = \frac{\theta_{\max}}{u_{\text{roof}}/H}. \quad (1)$$

It can be observed in Figures 9(a) and 9(b) that when structures arrive at the peak lateral load-carrying capacity, the interstorey drift ratios of 1F and 2F are higher than those of 3F-8F in the PRCFCP and PRCFCP-USD, and the interstorey shear forces of 3F-8F do not reach their interstorey lateral load-carrying capacities,

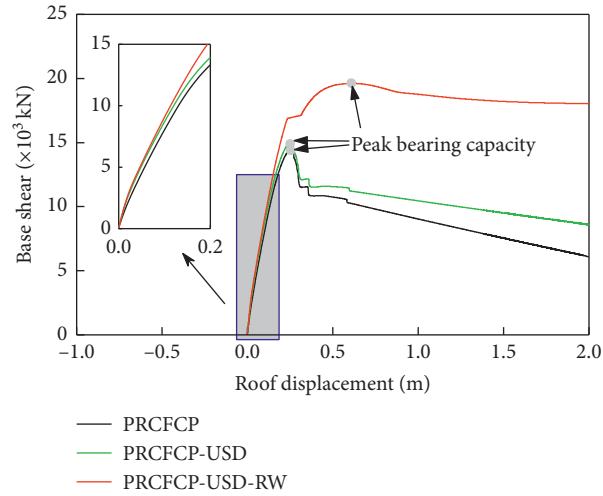


FIGURE 8: Curves of the base shear force and roof displacement.

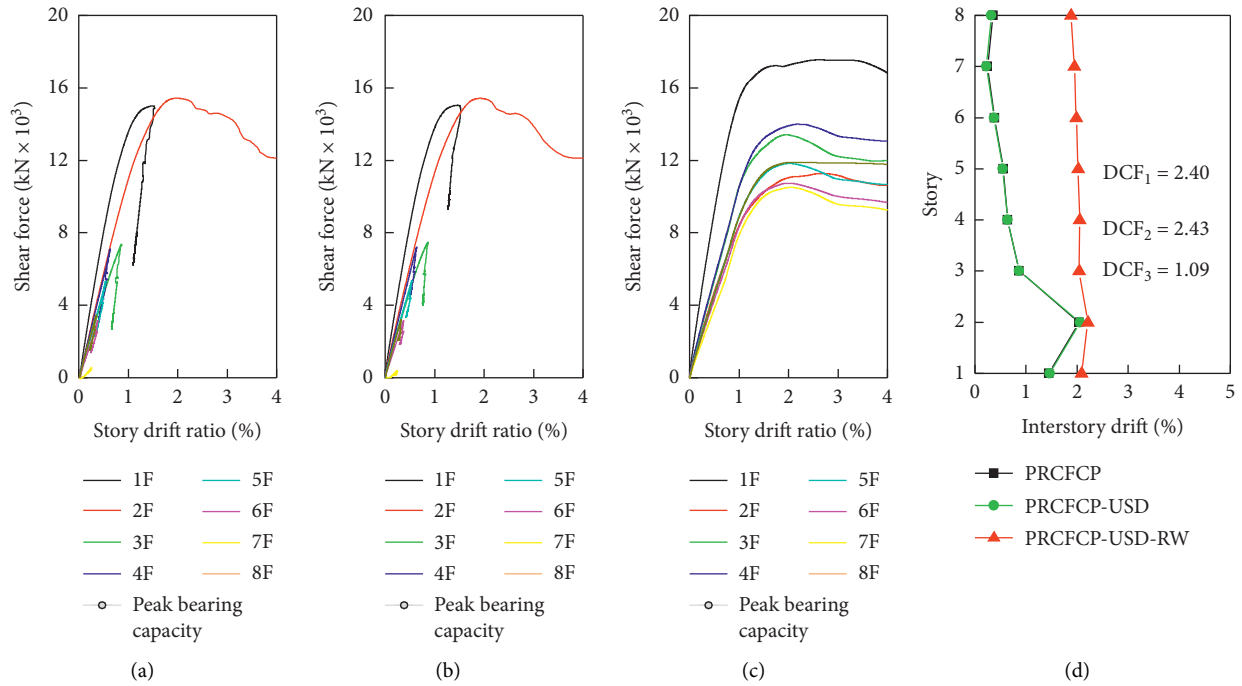


FIGURE 9: Interstorey shear force and interstorey drift curves of the frame. (a) PRCFCP. (b) PRCFCP -USD. (c) PRCFCP -USD-RW. (d) Inter-storey drift.

implying that these storeys basically maintain the elastic status. The DCF values of the PRCFCP and PRCFCP-USD are 2.40 and 2.43, respectively, which means that the damage concentration exists. After the structures arrive at the peak lateral load-carrying capacity, the interstorey drift ratios of 2F in the PRCFCP and PRCFCP-USD are continuously increased as the loading continues; however, the interstorey drift ratios and shear forces of other storeys are slightly and considerably decreased, respectively. These results indicate that the damage of the PRCFCP and PRCFCP-USD is concentrated on the second storey and that the capacities of other storeys cannot be fully used.

Figure 9(c) shows that the interstorey drift ratios at each storey of the PRCFCP-USD-RW are basically the same, and the DCF value is only 1.09 when it arrives at the lateral load-carrying capacity. The trends of the interstorey shear force and the drift ratio curves are similar among the different storeys during the whole loading process, and all storeys can enter the plastic phase at the same time. The results indicate that the capacities of all storeys can be fully used due to the addition of rocking walls.

In conclusion, it is difficult to change the structural deformation mode by the use of USDs; however, the addition of rocking wall is an effective way to control the distribution of the interstorey shear force and drift.

5. Nonlinear Dynamic Time-History Analyses

5.1. Peak Interstorey Drift Responses. Figure 10 compares the distributions of the peak interstorey drift ratios for the contrast models under major earthquakes. The peak interstorey drift ratios of the PRCFCP and PRCFCP-USD exhibit an obvious increase at the second storey, indicating that the structures show an interstorey damage concentration. The average interstorey drift ratio of the PRCFCP is close to the allowable limit (2%) [27]. A comparison of Figures 10(a) and 10(b) shows that the peak interstorey drift ratios of the PRCFCP-USD are less than those of the PRCFCP, which illustrates that USDs arranged in the structure can play a role in energy dissipation to reduce the peak interstorey drift response. Figure 10(c) shows that the peak interstorey drift ratios of the PRCFCP-USD-RW are uniformly distributed and do not exhibit obvious increase or reduction, and the average value is far less than 2%. These results indicate that the USDs and rocking walls of the PRCFCP-USD-RW can work together to render peak interstorey drifts small and uniform.

Figure 11 presents the corresponding *DCF* results of the contrast models under major earthquakes. The *DCF* average values for the PRCFCP, PRCFCP-USD, and PRCFCP-USD-RW under various ground motions are 2.53, 2.50, and 1.19, and their standard deviations are 0.89, 0.49, and 0.09, respectively. These results indicate that the rocking walls can control structural deformation and reduce the randomness of the damage concentration. Compared with the PRCFCP, the *DCF* values of the PRCFCP-USD are larger under some ground motions. In other words, the *DCF* value may be increased, and the unevenness of the interstorey drift distribution may be deepened when the USDs are arranged. This conclusion that the USD cannot control the structural deformation mode is consistent with Figures 9 and 10.

5.2. Hysteresis Responses of the USDs. For the PRCFCP-USD and PRCFCP-USD-RW structures, the USDs at the same position of each storey are selected to check the hysteresis response. Figure 12 shows the USDs' hysteretic curves of the PRCFCP-USD and PRCFCP-USD-RW at each storey under the 9th ground motion. As shown in Figure 12(a), the hysteretic curves of the USDs arranged at 1 F and 2 F are full, and the energy dissipations are overused, in which the USDs may reach their energy limit and be destroyed. The USDs at 3 F–6 F cannot fully use the performance, and the USDs arranged at 7 F and 8 F are in the elastic phase and basically do not dissipate any seismic energy. These results indicate that, compared to the PRCFCP-USD-RW, the PRCFCP-USD is prone to the serious damage concentration in that the USDs yield only at less storeys.

As shown in Figure 12(b), the USDs in the PRCFCP-USD-RW show uniform energy dissipation along the structural height. A comparison of Figures 12(a) and 12(b) shows that the energy dissipation of the USDs at 1 F and 2 F in PRCFCP-USD-RW is less than that of PRCFCP-USD, and this situation is reversed at other storeys. In particular, the USDs placed at 7 F and 8 F in PRCFCP-USD-RW are still

able to dissipate energy, indicating that the addition of rocking walls can enable all USDs at each storey to enter the energy dissipation stage by coordinating each storey drift to avoid the waste of the USD performance. The distributions of the USDs' displacement responses at each storey observed from Figures 12(a) and 12(b) are consistent with Figures 10(b) and 10(c), respectively, because the deformation of the USDs is mainly determined by the interstorey drift of the frame. Thus, the distribution of the USDs' energy dissipation at each storey is also consistent with the structural interstorey drifts.

5.3. Dispersion Coefficients. A dispersion coefficient α_i is defined herein as (2) for the purpose of evaluating the level of uneven energy dissipation of the USDs at each storey. The parameter μ_i is the ductility coefficient of the USD at the i th storey, and μ_{ave} is the average value of μ_i , which can be calculated using (3). When α_i is closer to 1, the difference in the USDs' energy dissipation at each storey is less:

$$\alpha_i = \mu_i / \mu_{ave} \quad (i = 1 \sim 8), \quad (2)$$

$$\mu_{ave} = (\mu_1 + \mu_2 + \dots + \mu_8) / 8. \quad (3)$$

Figure 13 shows the distribution of α_i for the PRCFCP-USD and PRCFCP-USD-RW under the 22 ground motions. The α_i of the PRCFCP-USD and PRCFCP-USD-RW falls in the range of 0.5–2.5 and 0.8–1.3, respectively. In other words, the difference in the energy dissipation of the USDs at various storeys in the PRCFCP-USD-RW is less than that of the PRCFCP-USD. Therefore, the addition of rocking walls can control the USDs at various storeys to uniformly dissipate the seismic energy.

5.4. Energy Dissipation. Figure 14 shows a comparison of the total energy dissipation for contrast models under each ground motion. Table 3 gives the average energy dissipation of the frame and USDs in three models under 22 ground motions. The total energy dissipation of the PRCFCP-USD and the PRCFCP-USD-RW is similar. From the foregoing analyses, although the dissipated energy of the USDs at 1 F and 2 F in the PRCFCP-USD-RW is less than that of the PRCFCP-USD, the USDs at other storeys of the PRCFCP-USD-RW can fully dissipate the energy, which further causes the total energy dissipation of the USDs in the PRCFCP-USD-RW to be greater than that of the PRCFCP-USD. The seismic energy dissipation by the frame in the PRCFCP is higher than that in the others, which means that the damage to the frame in the PRCFCP is more serious than that in the PRCFCP-USD and PRCFCP-USD-RW. In addition, the seismic energy dissipation by the frame in the PRCFCP-USD-RW is only 63% of that in the PRCFCP-USD. The result indicates that the combination of USDs and rocking walls can effectively reduce the damage to the main structure.

Figure 15 shows the energy dissipation at each storey of the three contrast models under the 9th ground motion. The seismic energy in the PRCFCP and PRCFCP-USD is mainly

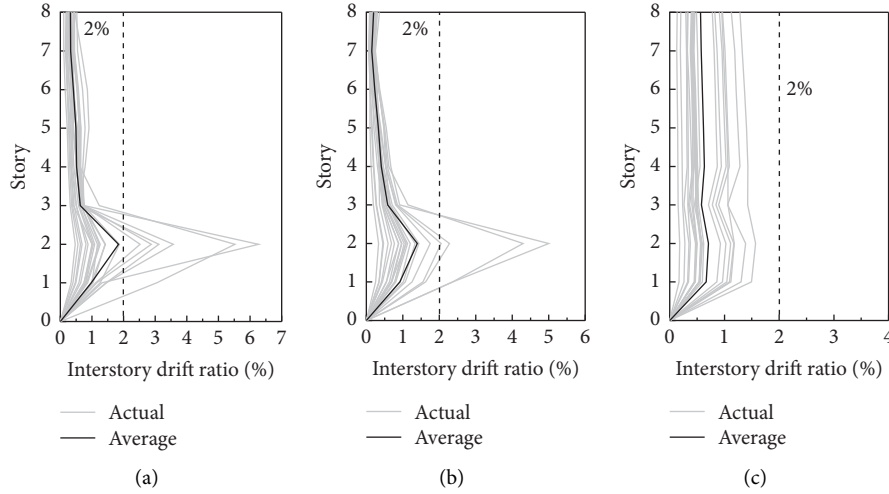


FIGURE 10: Comparison of the peak interstorey drift distributions under major earthquakes. (a) PRCFCP. (b) PRCFCP -USD. (c) PRCFCP -USD-RW.

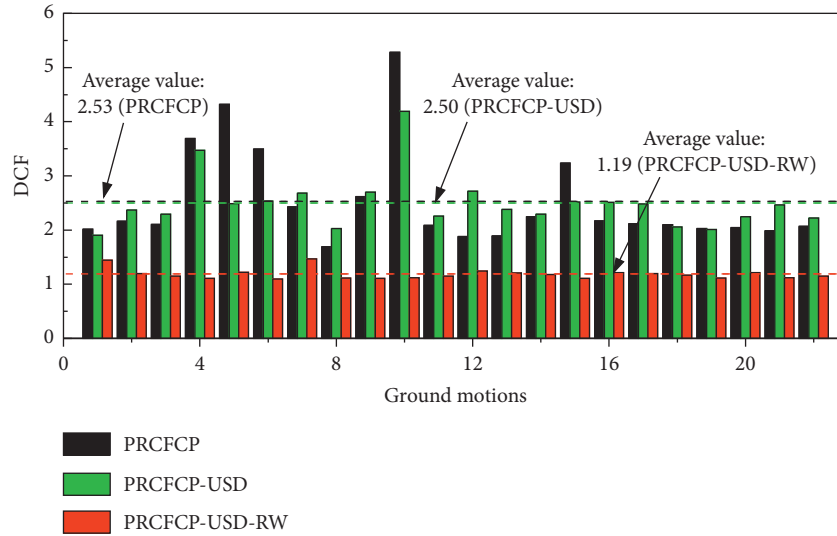


FIGURE 11: Comparison of the *DCF*s under major earthquakes.

dissipated by the members at the 1–2 storeys, which is a significantly uneven energy dissipation. The frame at storeys 1–2 in the PRCFCP and PRCFCP-USD exhibits severe plastic deformation, while the frame at storeys 6–8 basically maintains flexibility, which means that the PRCFCP-USD exhibits damage concentration. In contrast, the frame and USDs in the PRCFCP-USD-RW roughly consume the same energy at each storey. The damage of the PRCFCP-USD-RW is concentrated in the USDs, and each storey of the frame evenly produces a slight plastic deformation. Compared with the PRCFCP-USD, the PRCFCP-USD-RW exhibits enhanced seismic performance, and the proposed approach of combining the USDs and the rocking walls can protect the main frame to avoid severe destruction and damage concentration.

5.5. Residual Displacement. Figure 16 shows the distributions of the residual interstorey drift ratios of the contrast models under major earthquakes. The largest residual interstorey drift ratio of the PRCFCP occurs at 2F, and the average value is 0.29%, while the values of the PRCFCP-USD and PRCFCP-USD-RW are only 0.075% and 0.031%, respectively. Compared with the PRCFCP, the peak residual interstorey drift ratios of the PRCFCP-USD and PRCFCP-USD-RW are reduced by 74.1% and 89.3%, respectively. These results mean that the residual displacement can be reduced by the participation of USDs, and the rocking walls can enhance the USDs' capacity of reducing the residual displacement. The residual displacement of the PRCFCP-USD-RW is also uniformly distributed at various storeys similar to the peak deformation.

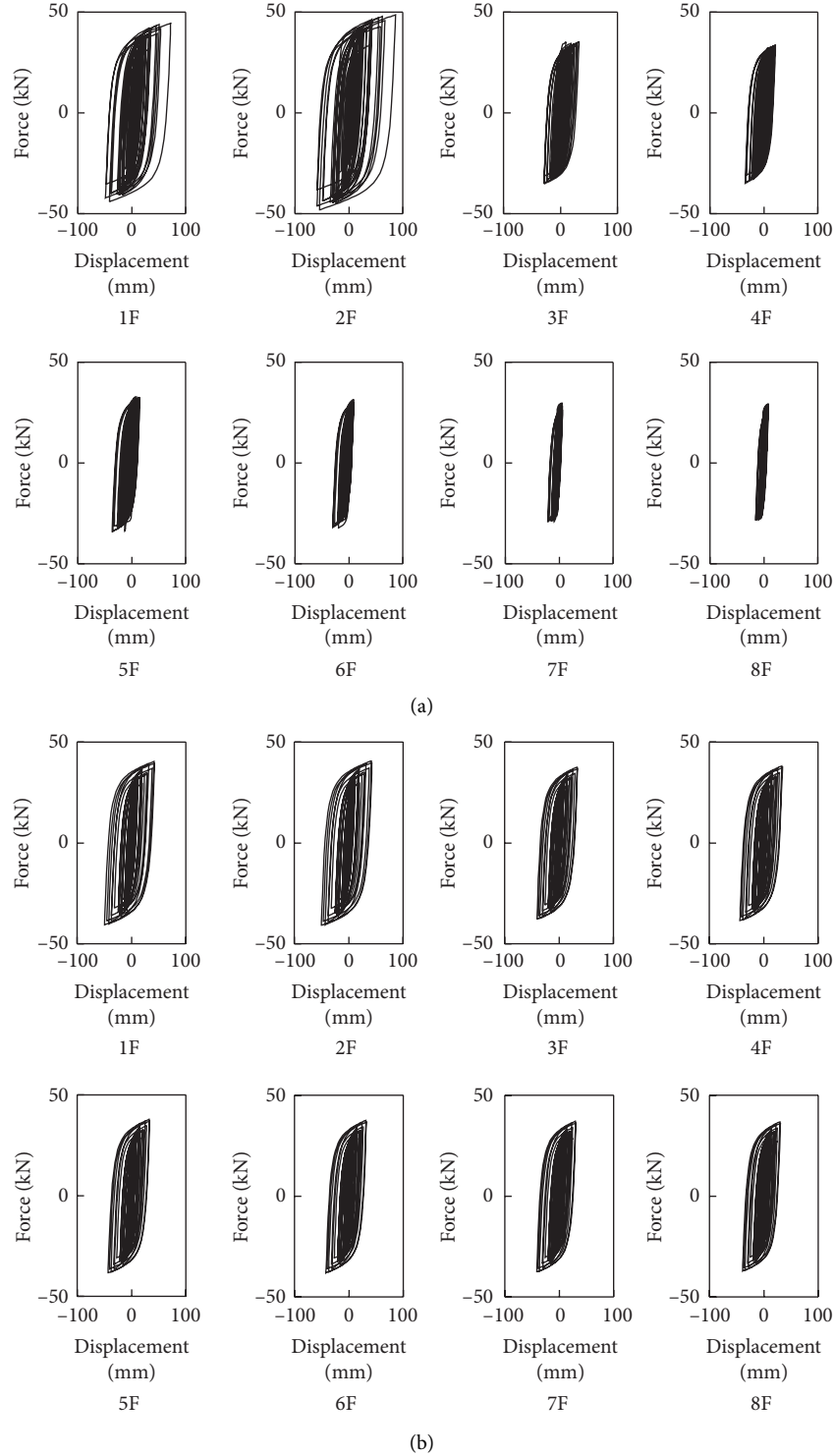


FIGURE 12: Hysteresis responses of the USDs at different storeys of PRCFCP-USD and PRCFCP-USD-RW under GM9. (a) PRCFCP-USD. (b) PRCFCP-USD-RW.

6. Incremental Dynamic Analyses (IDAs)

6.1. IDA Curves. The seismic collapse capacities of the three contrast models are analysed via the incremental dynamic analysis (IDA) method [36] under the 22 ground motions shown in Section 3.4. The limit interstorey drift ratio of 2.0%

specified by ASCE7-10 [37, 38] is used as the sign of the collapse. The approach used to scale the 22 GMs was the hunt&fill algorithm mentioned in [39]. The amplitude modulation and the increment of the step are 0.2g and 0.05g, respectively, and the $S_a(T_1, 5\%)$ (means the spectral acceleration of the ground motions at the fundamental

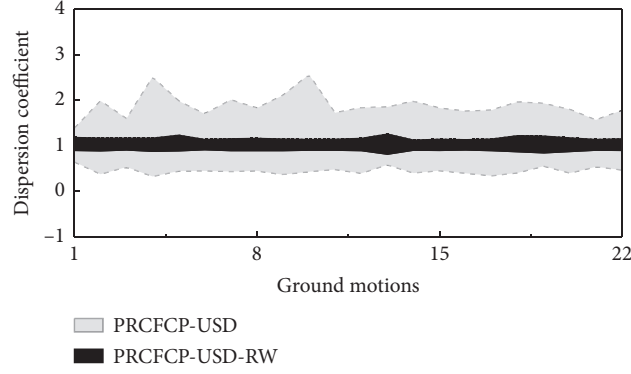


FIGURE 13: Dispersion coefficients of the USDs energy dissipation under 22 ground motions.

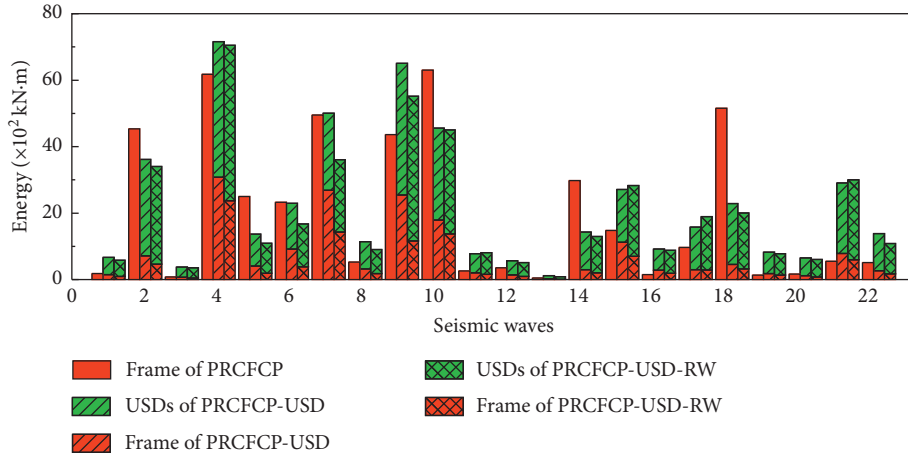


FIGURE 14: Comparison of the total energy dissipation under 22 ground motions.

TABLE 3: Average energy dissipation of the frame and USDs under 22 ground motions (unit: kN·m).

	PRCFCP-USD	PRCFCP -USD-RW	PRCFCP -USD-RW/PRCFCP -USD (%)
Frame	766.85	483.92	63
USDs	1454.87	1538.09	106
Total	2221.72	2022.01	91

period of the structure corresponding to 5% damping ratio) of the first analysis step is 0.005 g. The amplitude modulation coefficient (λ_i) and the inputting acceleration of 22 ground motions used in the analyses (S_a') can be calculated using (4) and (5), respectively:

$$\lambda_i = S_a(T1, 5\%)/S_{GT}, \quad (4)$$

$$S_a' = \lambda_i \cdot S_a, \quad (5)$$

where S_{GT} is the spectral acceleration for 22 ground motions-adjusted acceleration peaks to 4 m/s² corresponding to the major earthquake specified by the Chinese code (GB

50011–2010) and S_a is the actual acceleration of the 22 ground motions (the peak S_a was modulated to 1 m/s² in this paper).

Figure 17 shows the IDA curves of the three contrast models corresponding to 16%, 50%, and 84% quantile levels. The IDA curves of the PRCFCP corresponding to three quantile levels are lower than those of the PRCFCP-USD and PRCFCP-USD-RW, indicating that the addition of USDs can improve the seismic collapse capacity. The IDA curve of the PRCFCP-USD-RW is significantly higher than that of the PRCFCP-USD, which reveals that the rocking walls can further improve the structural seismic collapse capacity.

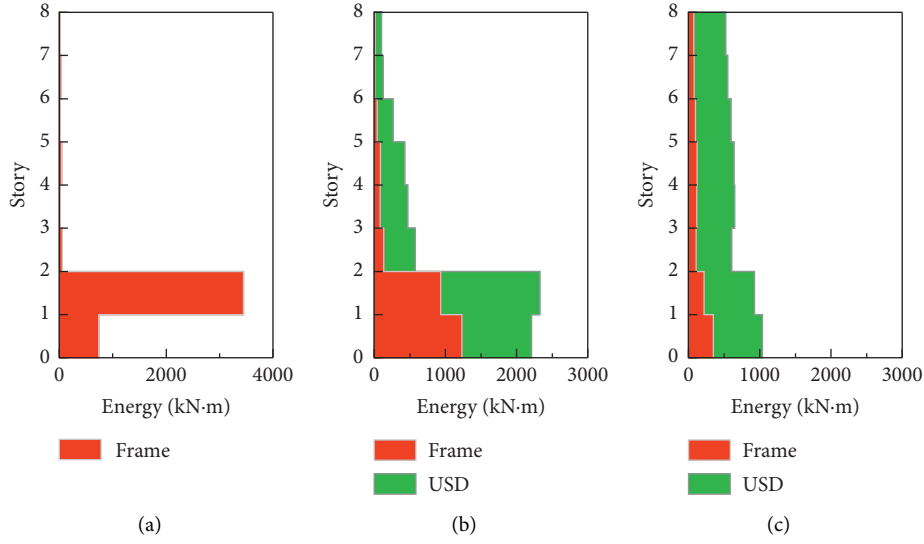


FIGURE 15: Energy dissipation at different storeys under GM9.

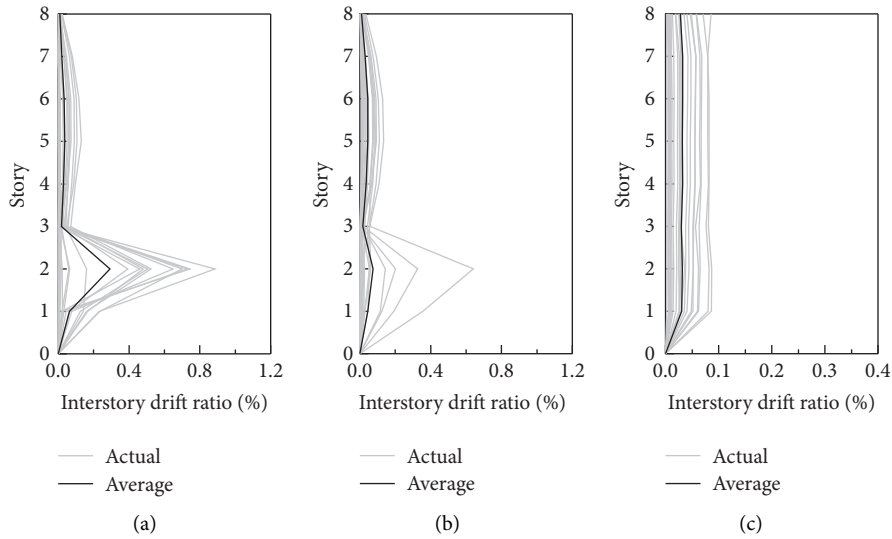


FIGURE 16: Comparison of the residual interstorey drifts under major earthquakes. (a) PRCFCP. (b) PRCFCP -USD. (c) PRCFCP -USD-RW.

6.2. Evaluation of the Seismic Collapse Capacity. The collapse margin ratio (*CMR*), an important index for measuring the structural seismic collapse capacity [40], can be calculated by (6), where \hat{S}_{CT} is the spectral acceleration corresponding to the median value of the estimated spectral accelerations at collapse and S_{MT} is the spectral acceleration at the fundamental period of the structure shown in Figure 6:

$$CMR = \hat{S}_{CT}/S_{MT}. \quad (6)$$

Figure 18 shows the comparison of the collapse probability curves for the contrast models. The collapse

probability of the PRCFCP-USD and PRCFCP-USD-RW is significantly smaller than that of the PRCFCP under the same intensity earthquake. Table 4 shows the *CMR* values of the contrast models. The *CMR* value of the PRCFCP-USD is increased by 31.3% compared to the PRCFCP, which means that the seismic collapse capacity can be improved via the addition of USDs. The *CMR* of the PRCFCP-USD-RW is increased by 152.8%, which is approximately five times that of 31.3%, which means that the participation of rocking walls further improves the seismic collapse capacity of the PRCFCP-USD.

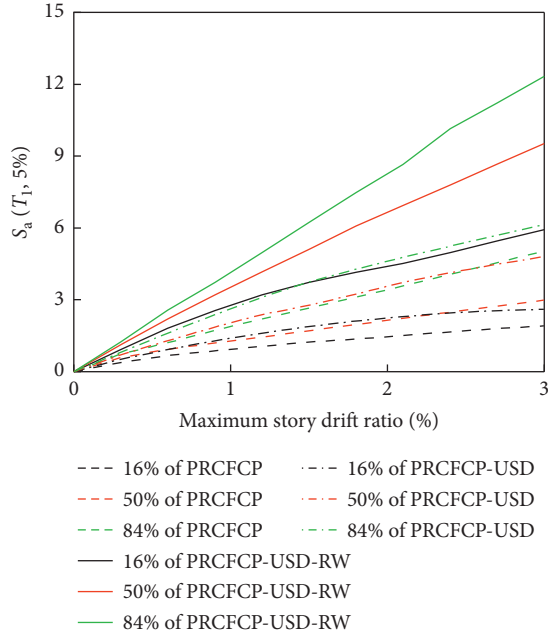


FIGURE 17: Comparison of the three models' IDA curves.

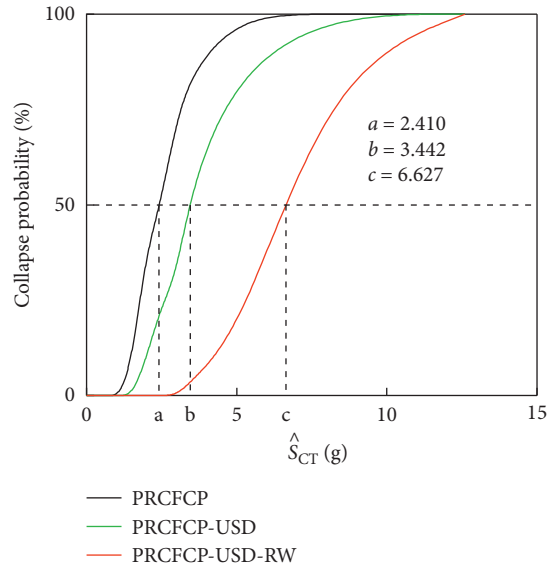


FIGURE 18: Comparison of the collapse fragility curves among the contrast models.

TABLE 4: CMR of all models.

Models	\hat{S}_{CT}	S_{MT} (g)	CMR	Increase
PRCFCP	2.410 g	0.356	6.77	—
PRCFCP-USD	3.442 g	0.387	8.89	31.3%
PRCFCP-USD-RW	6.627 g	0.387	17.12	152.8%

7. Conclusions

The energy dissipation capacity of the USDs placed between the cladding panels and the main structure and the controlling deformation capacity of rocking walls are combined

to improve the seismic performance of the traditional PRCFCP. The following conclusions are obtained through the comparative analyses of the structures with/without the USDs or the rocking walls.

- (1) The participation of the USDs can slightly enhance the lateral load-carrying capacity of the structure and slightly reduce the velocity of the carrying reduction after structural yield under a pushover compared with the PRCFCP. However, the combination of rocking walls and USDs can significantly enhance the lateral load-carrying capacity and ductility of the structure.
- (2) In PRCFCP-USD, the USDs can dissipate energy and effectively reduce the deformation of the structure under an earthquake, indicating that the cladding panel with USDs can achieve the target of shock absorption.
- (3) The USDs at each storey of the PRCFCP-USD exhibit a large difference in energy dissipation. In the position where the interstorey drift is sufficient, the USDs dissipate energy in excess. In places with smaller drifts, the USDs' capacity cannot entirely perform. Rocking walls can compel the USDs at each storey to evenly dissipate energy.
- (4) Compared with the PRCFCP, the *DCF* values of the PRCFCP-USD are larger under some ground motions because the USDs at each storey unevenly dissipate energy. In the PRCFCP-USD-RW, the peak interstorey drift and residual displacement are small and uniform, and the *DCF* average value is only 1.19. According to conclusions (2)–(4), the use of USDs can reduce the structural displacement response but not control the structural deformation profile; however, the two design goals can be simultaneously achieved through the combination of rocking walls and USDs.
- (5) The seismic collapse capacity of the PRCFCP-USD and PRCFCP-USD-RW is larger than that of the PRCFCP. The *CMR* value of the PRCFCP-USD-RW is approximately five times that of the PRCFCP-USD, showing that the seismic collapse capacity can be improved by the proposed cladding panels with USDs and that the combination of rocking walls and USDs further improves the seismic collapse capacity.

Data Availability

The authors declare that all data supporting the findings of this study are available within the article.

Conflicts of Interest

The authors declare no conflicts of interest.

Acknowledgments

This research was financially supported by the National Natural Science Foundation of China (nos. 51708166,

51778201, and 51878233), the Fundamental Research Funds for Central Universities of China (no. JZ2019HGTB0086), and the China Postdoctoral Science Foundation (no. 2018M630706). Their support is gratefully acknowledged.

References

- [1] H. Maneetes, "Development of a seismic dissipating mechanism for precast concrete cladding panels," Ph.D. Dissertation, Pennsylvania State, University, State College, PA, USA, 2007.
- [2] E. D. Losch, P. W. Hynes, R. Andrews Jr. et al., "State of the art of precast/prestressed concrete sandwich wall panels," *PCI Journal*, vol. 56, no. 2, pp. 131–176, 2011.
- [3] Precast/Prestressed Concrete Institute, *PCI Design Handbook*, Precast/Prestressed Concrete Institute, Chicago, IL 60606, USA, 7th edition, 2010.
- [4] JGJ/T458-2018, *Technical standard for application of precast concrete facade panel*, China Building Industry Press, Beijing, USA, 2018, in Chinese.
- [5] A. Belleri, E. Brunesi, R. Nascimbene et al., "Seismic performance of precast industrial facilities following major earthquakes in the Italian territory," *Journal of Performance of Constructed Facilities*, vol. 29, no. 5, Article ID 04014135, 2014.
- [6] G. Toniolo and A. Colombo, "Precast concrete structures: the lessons learned from the L'Aquila earthquake," *Structural Concrete*, vol. 13, no. 2, pp. 73–83, 2012.
- [7] D. A. Bournas, P. Negro, and F. F. Taucer, "Performance of industrial buildings during the Emilia earthquakes in Northern Italy and recommendations for their strengthening," *Bulletin of Earthquake Engineering*, vol. 12, no. 5, pp. 2383–2404, 2014.
- [8] GCR Nist 96-681, *Literature Review on Seismic Performance of Building Cladding Systems*, National Institute of Standards and Technology, United States Department of Commerce, Gaithersburg, MD, USA, 1995.
- [9] R. Tyler, "Damping in building structures by means of PTFE sliding joints," *Bulletin of New Zealand National Society for Earthquake Engineering*, vol. 10, no. 3, pp. 139–142, 1977.
- [10] J. M. Cohen and G. H. Powell, "A design study of an energy-dissipating cladding system," *Earthquake Engineering & Structural Dynamics*, vol. 22, no. 7, pp. 617–632, 1993.
- [11] J.-P. Pinelli, C. Moor, J. I. Craig, and B. J. Goodno, "Testing of energy dissipating cladding connections," *Earthquake Engineering & Structural Dynamics*, vol. 25, no. 2, pp. 129–147, 1996.
- [12] L. Ferrara, R. Felicetti, G. Toniolo, and C. Zenti, "Friction dissipative devices for cladding panels in precast buildings," *European Journal of Environmental and Civil Engineering*, vol. 15, no. 9, pp. 1319–1338, 2011.
- [13] A. Baird, A. Palermo, and S. Pampanin, "Controlling seismic response using passive energy dissipating cladding connections," in *Proceedings of the New Zealand Society for Earthquake Engineering Conference*, Wellington, New Zealand, April 2013.
- [14] P. Negro and M. Lamperti Tornaghi, "Seismic response of precast structures with vertical cladding panels: the safe-cladding experimental campaign," *Engineering Structures*, vol. 132, pp. 205–228, 2017.
- [15] B. Dal Lago, F. Biondini, and G. Toniolo, "Experimental investigation on steel W-shaped folded plate dissipative connectors for horizontal precast concrete cladding panels," *Journal of Earthquake Engineering*, vol. 22, no. 5, pp. 778–800, 2018.
- [16] B. Dal Lago, F. Biondini, and G. Toniolo, "Experimental tests on multiple-slit devices for precast concrete panels," *Engineering Structures*, vol. 167, pp. 420–430, 2018.
- [17] F. Karadoğan, E. Yüksel, A. Khajehdehi et al., "Cyclic behavior of reinforced concrete cladding panels connected with energy dissipative steel cushions," *Engineering Structures*, vol. 189, pp. 423–439, 2019.
- [18] B. Alavi and H. Krawinkler, "Strengthening of moment-resisting frame structures against near-fault ground motion effects," *Earthquake Engineering & Structural Dynamics*, vol. 33, no. 6, pp. 707–722, 2004.
- [19] Z. Qu, A. Wada, S. Motoyui, H. Sakata, and S. Kishiki, "Pin-supported walls for enhancing the seismic performance of building structures," *Earthquake Engineering & Structural Dynamics*, vol. 41, no. 14, pp. 2075–2091, 2012.
- [20] G. Deierlein, H. Krawinkler, X. Ma et al., "Earthquake resilient steel braced frames with controlled rocking and energy dissipating fuses," *Steel Construction*, vol. 4, no. 3, pp. 171–175, 2011.
- [21] A. Wada, Z. Qu, S. Motoyui, and H. Sakata, "Seismic retrofit of existing SRC frames using rocking walls and steel dampers," *Frontiers of Architecture and Civil Engineering in China*, vol. 5, no. 3, pp. 259–266, 2011.
- [22] K. M. Twigden and R. S. Henry, "Experimental response and design of O-connectors for rocking wall systems," *Structures*, vol. 3, pp. 261–271, 2015.
- [23] Z. Zhang, R. B. Fleischman, J. I. Restrepo et al., "Shake-table test performance of an inertial force-limiting floor anchorage system," *Earthquake Engineering & Structural Dynamics*, vol. 47, no. 10, pp. 1987–2011, 2018.
- [24] Y. Feng, Z. Zhang, X. Chong, J. Wu, and S. Meng, "Elastic displacement spectrum-based design of damage-controlling BRBFs with rocking walls," *Journal of Constructional Steel Research*, vol. 148, pp. 691–706, 2018.
- [25] N. Rahgozar, N. Rahgozar, and A. S. Moghadam, "Controlled-rocking braced frame bearing on a shallow foundation," *Structures*, vol. 16, pp. 63–72, 2018.
- [26] J. M. Kelly, R. I. Skinner, and A. J. Heine, "Mechanisms of energy absorption in special devices for use in earthquake resistant structures," *Bulletin of NZ Society for Earthquake Engineering*, vol. 5, no. 3, pp. 63–88, 1972.
- [27] S. Bagheri, M. Barghian, F. Saieri, and A. Farzinfar, "U-shaped metallic-yielding damper in building structures: seismic behavior and comparison with a friction damper," *Structures*, vol. 3, pp. 163–171, 2015.
- [28] S. Mazzoni, F. McKenna et al., *OpenSees Command Language Manual*, PEER, University of California, Berkeley, CA, USA, 2006.
- [29] GB 50017-2003, *Code for Design of Steel Structures*, China Planning Press, Beijing, China, 2003, in Chinese.
- [30] A. I. Dimopoulos, T. L. Karavasilis, G. Vasdravellis, and B. Uy, "Seismic design, modelling and assessment of self-centering steel frames using post-tensioned connections with web hourglass shape pins," *Bulletin of Earthquake Engineering*, vol. 11, no. 5, pp. 1797–1816, 2013.
- [31] Z. Qu, *Study on Seismic Damage Mechanism Control and Design of Rocking Wall-Frame structures*, Tsinghua University, Beijing, China, Ph.D. Dissertation in Chinese, 2010.
- [32] M. Palermo and T. Trombetti, "Experimentally-validated modelling of thin RC sandwich walls subjected to seismic loads," *Engineering Structures*, vol. 119, pp. 95–109, 2016.

- [33] E. Brunesi, R. Nascimbene, and A. Pavese, "Mechanical model for seismic response assessment of lightly reinforced concrete walls," *Earthquakes and Structures*, vol. 11, no. 3, pp. 461–481, 2016.
- [34] GB 50011-2010, *Code for Seismic Design of Buildings*, China Architecture & Building Press, Beijing, China, 2010, in Chinese.
- [35] G. A. MacRae, Y. Kimura, and C. Roeder, "Effect of column stiffness on braced frame seismic behavior," *Journal of Structural Engineering*, vol. 130, no. 3, pp. 381–391, 2004.
- [36] D. Vamvatsikos and C. A. Cornell, "Incremental dynamic analysis," *Earthquake Engineering & Structural Dynamics*, vol. 31, no. 3, pp. 491–514, 2002.
- [37] ASCE, *Minimum Design Loads for Buildings and Other Structures (ASCE/SEI 7-10)*, American Society of Civil Engineers, Reston, VA, USA, 2010.
- [38] S. Zaruma and L. A. Fahnestock, "Assessment of design parameters influencing seismic collapse performance of buckling-restrained braced frames," *Soil Dynamics and Earthquake Engineering*, vol. 113, pp. 35–46, 2018.
- [39] D. Vamvatsikos and C. A. Cornell, "Tracing and post-processing of IDA curves: theory and software implementation," p.44, Report No. RMS, Stanford University and Stanford, USA, 2001.
- [40] Federal Emergency Management Agency (FEMA), *Quantification of building seismic performance factors*, FEMA, Washington, D.C., USA, 2009.